Discrete Element Modelling of Rock Cutting Processes Interaction with Evaluation of Tool Wear

J. Rojek
E. Oñate
F. Zárate
C.A. Recarey

Monograph CIMNE Nº-87, October 2003

Discrete Element Modelling of Rock Cutting Processes Interaction with Evaluation of Tool Wear

J. Rojek[1], E. Oñate[2], F. Zárate[2] and C.A. Recarey[2]

[1] Institute of Fundamental Technological Research (IPPT)
Polish Academy of Sciences
Swietokrzyska 21, 00-049 Warszawa, Poland

[2] International Center for Numerical Methods in Engineering (CIMNE)
Universidad Politécnica de Cataluña
Campus Norte UPC, 08034 Barcelona, Spain

Monograph CIMNE Nº-87, October 2003

INTERNATIONAL CENTER FOR NUMERICAL METHODS IN ENGINEERING
Gran Capitán s/n, 08034 Barcelona, Spain

INTERNACIONAL CENTER FOR NUMERICAL METHODS IN ENGINEERING
Edificio C1, Campus Norte UPC
Gran Capitán s/n
08034 Barcelona, Spain
www.cimne.upc.es

First edition: October 2003

DISCRETE ELEMENT MODELLING OF ROCK CUTTING PROCESSES INTERACTION WITH EVALUATION OF TOOL WEAR
Monograph CIMNE M87
© The authors

ISBN: 84-95999-44-7

Depósito legal: B-47351-2003

Contents

Abstract

The document presents a numerical model of rocks and soils using spherical Discrete Elements, also called Distinct Elements. The motion of spherical elements is described by means of equations of rigid body dynamics. Explicit integration in time yields high computational efficiency. Spherical elements interact among one another with contact forces, both in normal and tangential directions. Efficient contact search scheme based on the octree structures has been implemented. Special constitutive model of contact interface taking into account cohesion forces allows us to model fracture and decohesion of materials.

Numerical simulation predicts wear of rock cutting tools. The developed numerical algorithm of wear evaluation allows us us to predict evolution of the shape of the tool caused by wear.

Results of numerical simulation are validated by comparison with experimental data.

Chapter 1

Introduction

This report presents numerical modelling of rock cutting processes with tool wear evaluation. The numerical model is based on the discrete element method in the version using spherical particles.

This method is widely recognized as a suitable tool to model problems characterized with strong discontinuities. The discrete element model assumes that material can be represented by an assembly of rigid particles interacting among themselves. The overall behaviour of the system is determined by the cohesive/frictional contact laws.

Granular and particulate materials are characterized with inherent discrete nature. Discontinuity in rocks can occur due to progressive damage during cutting.

Discrete element formulation using spherical or cylindrical particles was first proposed by Cundall and Strack [1]. Similar formulation has been developed by Rojek et al. in [2] and implemented in the explicit dynamic finite element code Simpact.

Chapter 2

Modelling of rock cutting

2.1 Physical phenomena in rock cutting

The type of failure during rock cutting depends on the type of rock. In some rocks brittle failure with characteristic chip formation occurs (Fig. 2.1a), while others fail by ductile ploughing (Fig. 2.1b). According to Gehring [3] ductility (or brittleness) of a rock can be measured by the ratio of unconfined compressive strength to unconfined tensile strength, which he called a ductility number. Typical brittle rocks have ductility number greater than 15, while typical ductile rocks are characterised with ductility numbers lower than 9. Ductile cutting is very disadvantageous since the wear of tools is bigger than in case of brittle cutting. By adequate design of tool sometimes it is possible to change the mode of failure in cutting.

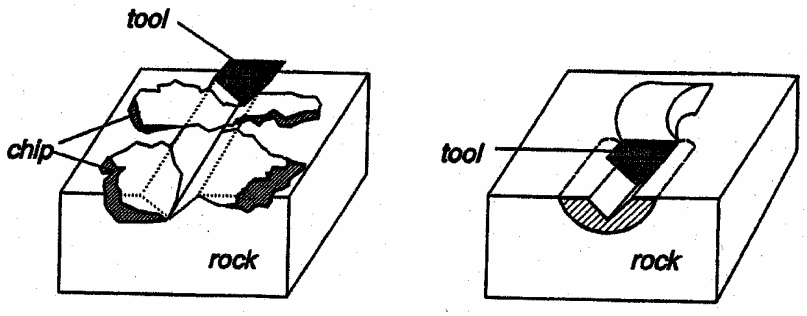

a) b)

Figure 2.1: Modes of failure in rock cutting: a) brittle, b) ductile

Formation of a chip in brittle cutting is initiated in a crushing zone near the tooth tip (Fig. 2.2). The forces are transmitted from the crushing zone to the intact rock and microcracks are initiated. Near the crushing zone localised shear zone is developed. Shear failure further in the intact rock can bifurcate into a tensile crack. This combined

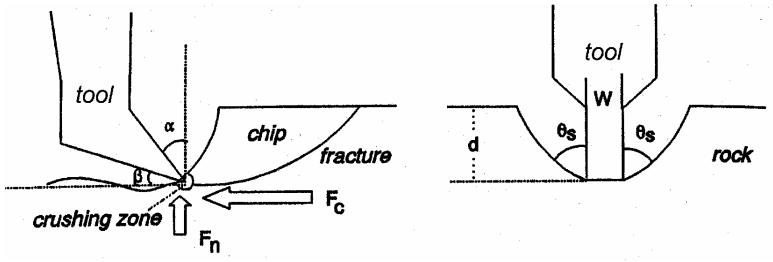

a) b)

Figure 2.2: Rock cutting: a) view parallel to cutting direction, b) view normal to cutting direction; α - rake angle, β - clearance angle, θ_s - breakout angle

action of shear and tensile fracture separates a chip from the intact rock (Fig. 2.2).

2.2 Analytical models of rock cutting

Simple analytical models have been created in attempt to describe cutting processes, particularly those with brittle failure (Whittaker et al [4]). One of the earliest models is that developed by Evans [5] for rock cutting with drag picks. He assumed that the breakage is essentially tensile and occurs along failure surface, which approximates a circular arc (Fig. 2.3). He derived the following formula for the cutting force:

$$F_c = \frac{2\sigma_t dw \sin\frac{1}{2}(90-\alpha)}{1-\sin\frac{1}{2}(90-\alpha)} \tag{2.1}$$

where σ_t is tensile strength, d is depth of cut, w is width of the tool and α is the rake angle.

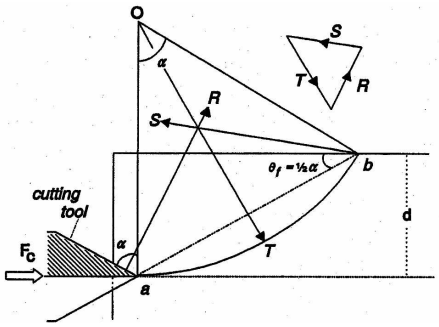

Figure 2.3: Evans' model of rock cutting

The main limitation of the Evans' theory is its two-dimensionality, negligence of the tool penetration and assumption of zero clearance angle β. Formula (2.1) usually underestimates the cutting force.

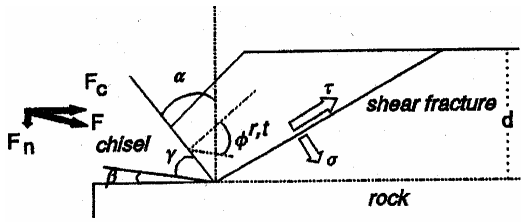

Figure 2.4: Nishimatsu's model of rock cutting

Another two-dimensional model is that developed by Nishimatsu [6] who assumed that failure is purely due to shear and occurs along a plane (Fig. 2.4). He obtained the following equation for resulting force F:

$$F = \frac{2\tau_u dw \cos\phi}{(n+1)(1-\sin(\phi^{r,t}+\phi-\alpha))} \tag{2.2}$$

where τ_u is the unconfined shear strength, d is depth of cut, w is width of the tool, $\phi^{r,t}$ is the angle of sliding friction rock-tool, ϕ is the angle of internal friction of intact rock, α is the rake angle, and n is an stress distribution factor obtained from the tests.

2.3 Basic assumptions of numerical model of rock cutting

This document presents a numerical model of the tool-rock/soil system allowing us to simulate a process of rock cutting and at the same time to estimate the wear of the tool. The main physical phenomenon considered is the interaction of the tool with a rock leading on one hand to failure of the rock and on the other hand to wear of the tool, the latter process usually slower, although in some cases visible change of tool shape can be seen after time as short as a few minutes.

Numerical model of rock/soil media adopted in the present study is based on the spherical discrete element method (DEM) which is widely recognized as a suitable tool to model geomaterials [1, 7, 8, 9]. Formulation of spherical discrete elements (called also distinct elements) following main assumptions of Cundall [1, 10] has been developed by Rojek et al. in [2] and implemented in the explicit dynamic finite element code Simpact. Within the DEM, it is assumed that solid material can be represented as a collection of rigid particles (spheres or balls in 3D and discs in 2D) interacting among themselves in the normal and tangential directions. Material deformation is assumed to be concentrated at the contact points. Appropriate contact laws allow us to obtain desired macroscopic material properties. Contact law used for rock modelling takes into account cohesive bonds between rigid particles. The contact law can be seen as the formulation of the material model on the microscopic level. Cohesive bonds can be broken, which allows us to simulate fracture of material and its propagation.

The tool is assumed rigid in our numerical model. Two kinds of tool discretization has been used. The first one similarly to the finite element method employs straight line segments (in 2D) or triangular facets (in 3D) to represent tool surface. In the second type of discretization the tool is also discretised with distinct elements.

One of the objective of the analysis is to obtain evolution of the tool shape Discretization of the tool with distinct elements allows us to modify the shape of the tool easily by removing "worn" particles.

The formulation of the discrete element method has been extended on thermal and thermo-mechanical coupled problems in order to take into account temperature as one of the important factors influencing wear process. Heat is generated in cutting process due to friction dissipation. In the model friction between the tool and rock particles as well as friction between rock particles themselves are considered. Heat conduction through the tool and rock is analysed and temperature distribution are obtained. Temperature of the tool surface lowers its hardness and increases its wear. This is considered by assuming temperature dependent tool hardness in the equations used to evaluate the tool wear.

Chapter 3

Discrete Element Method formulation

The DEM scheme using spherical rigid elements has been introduced by Cundall [1, 10]. Our study is based on our own implementation of the DEM in the finite element explicit dynamic code Simpact [2].

3.1 Equations of motion

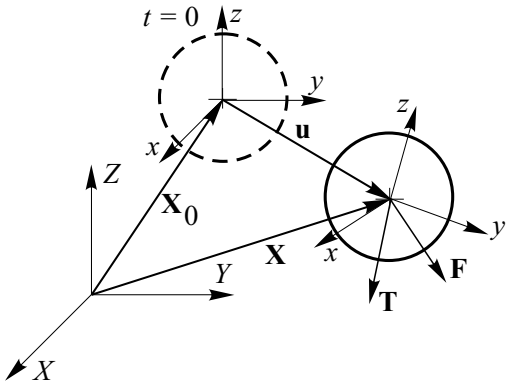

Figure 3.1: Motion of a rigid particle

The translational and rotational motion of rigid spherical or cylindrical particles (Fig. 3.1) is described by means of Newton-Euler equations of rigid body dynamics. For the i-th element we have

$$m_i \ddot{\mathbf{u}}_i = \mathbf{F}_i \,, \tag{3.1}$$

$$I_i \dot{\boldsymbol{\omega}}_i = \mathbf{T}_i \,, \tag{3.2}$$

where $\mathbf{u}$ is the element centroid displacement in a fixed (inertial) coordinate frame $\mathbf{X}$, $\boldsymbol{\omega}$ – angular velocity, m – element (particle) mass, I – moment of inertia, $\mathbf{F}$ – resultant force, and $\mathbf{T}$ – resultant moment about the central axes. Vectors $\mathbf{F}$ and $\mathbf{T}$ are sums of all forces and moments applied to the i-th element due to external load, contact interactions with neighbouring spheres and other obstacles, as well as forces resulting from damping in the system. The form of rotational equation (3.2) is valid for spheres and cylinders (in 2D) and is simplified with respect to a general form for an arbitrary rigid body with the rotational inertial properties represented by the second order tensor. In general case it is more convenient to describe the rotational motion with respect to co-rotational frame $\mathbf{x}$ which is embedded in each element since in this frame the tensor of inertia is constant. The tensor of inertia for a sphere or cylinder (in 2D) does not change in the fixed global coordinate system $\mathbf{X}$, so in this case the rotational motion can be easily considered in this system.

Equations of motion (3.1) and (3.2) are integrated in time using a central difference scheme. Time integration operator for the translational motion at the n-th time step is as follows:

$$\ddot{\mathbf{u}}_i^n = \frac{\mathbf{F}_i^n}{m_i}\,, \tag{3.3}$$

$$\dot{\mathbf{u}}_i^{n+1/2} = \dot{\mathbf{u}}_i^{n-1/2} + \ddot{\mathbf{u}}_i^n \Delta t\,, \tag{3.4}$$

$$\mathbf{u}_i^{n+1} = \mathbf{u}_i^n + \dot{\mathbf{u}}_i^{n+1/2} \Delta t\,. \tag{3.5}$$

The first two steps in the integration scheme for rotational motion are identical to those given by Eqs. (3.3) and (3.4):

$$\dot{\boldsymbol{\omega}}_i^n = \frac{\mathbf{T}_i^n}{I_i}\,, \tag{3.6}$$

$$\boldsymbol{\omega}_i^{n+1/2} = \boldsymbol{\omega}_i^{n-1/2} + \dot{\boldsymbol{\omega}}_i^n \Delta t\,. \tag{3.7}$$

For the rotational plane (2D) motion the rotation angle θ_i can be obtained similarly as displacement vector $\mathbf{u}_i$:

$$\theta_i^{n+1} = \theta_i^n + \omega_i^{n+1/2} \Delta t\,. \tag{3.8}$$

In three-dimensional motion, rotational position cannot be defined by any vector — rotational velocity $\boldsymbol{\omega}$ cannot be integrated, cf. [11]. The rotation matrix $\boldsymbol{\Lambda}_i$ is used to define the rotational position of the moving frame $\mathbf{x}_i$ with respect to the inertial frame $\mathbf{X}$

$$\mathbf{X} = \boldsymbol{\Lambda}_i \mathbf{x}_i\,. \tag{3.9}$$

The rotation matrix $\boldsymbol{\Lambda}_i$ is updated according to the following algorithm, cf. [11], [12]:

$$\Delta \boldsymbol{\theta}_i = \boldsymbol{\omega}_i^{n+1/2} \Delta t\,, \tag{3.10}$$

$$\Delta\mathbf{\Lambda}_i = \cos\|\Delta\boldsymbol{\theta}_i\|\mathbf{1} + \frac{\sin\|\Delta\boldsymbol{\theta}_i\|}{\|\Delta\boldsymbol{\theta}_i\|}\widetilde{\Delta\boldsymbol{\theta}}_i + \frac{1-\cos\|\Delta\boldsymbol{\theta}_i\|}{\|\Delta\boldsymbol{\theta}_i\|^2}\Delta\boldsymbol{\theta}_i\Delta\boldsymbol{\theta}_i^{\mathrm{T}}\,, \tag{3.11}$$

$$\mathbf{\Lambda}_i^{n+1} = \Delta\mathbf{\Lambda}_i\,\mathbf{\Lambda}_i^n\,. \tag{3.12}$$

Here $\Delta\boldsymbol{\theta} = \{\Delta\theta_x\,\Delta\theta_y\,\Delta\theta_z\}^{\mathrm{T}}$ denotes the vector of incremental rotation, $\Delta\mathbf{\Lambda}$ is the incremental rotation matrix, and $\widetilde{\Delta\boldsymbol{\theta}}$ is the skew-symmetric matrix defined as

$$\widetilde{\Delta\boldsymbol{\theta}} = \begin{bmatrix} 0 & -\Delta\theta_z & \Delta\theta_y \\ \Delta\theta_z & 0 & -\Delta\theta_x \\ -\Delta\theta_y & \Delta\theta_x & 0 \end{bmatrix}. \tag{3.13}$$

It must be remarked that knowledge of the rotational configuration is not always necessary. If tangential forces are calculated incrementally, then knowledge of the vector of incremental rotation $\Delta\boldsymbol{\theta}$ is sufficient. Then the steps (3.11) and (3.12) are not necessary which saves considerable computational cost of the time integration scheme.

3.2 Evaluation of contact forces

3.2.1 Decomposition of the contact force

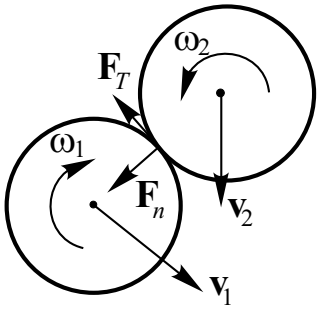

Figure 3.2: Decomposition of the contact force

Once the contact for a pair of particles has been detected, the forces occurring at the contact point are calculated. The interaction between the two bodies can be represented by the contact forces $\mathbf{F}_1$ and $\mathbf{F}_2$, which by the Newton's third law satisfy the following relations:

$$\mathbf{F}_1 = -\mathbf{F}_2\,. \tag{3.14}$$

We take $\mathbf{F} = \mathbf{F}_1$ and decompose $\mathbf{F}$ into normal and tangential components, $\mathbf{F}_n$ and $\mathbf{F}_T$, respectively (Fig. 3.2)

$$\mathbf{F} = \mathbf{F}_n + \mathbf{F}_T = F_n\mathbf{n} + \mathbf{F}_T\,,$$

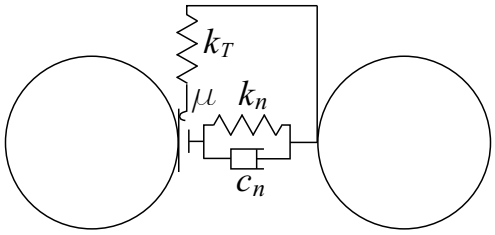

Figure 3.3: Model of the contact interface

where **n** is the unit vector normal to the particle surface at the contact point (this implies that it lies along the line connecting the centers of the two particles) and directed outwards from the particle 1.

The contact forces F_n and $\mathbf{F}_T$ are obtained using a constitutive model formulated for the contact between two rigid spheres (Fig. 3.3). The contact interface in our formulation is characterized by the normal and tangential stiffness k_n and k_T, the Coulomb friction coefficient μ, and the contact damping coefficient c_n.

3.2.2 Normal contact force

The normal contact force F_n is decomposed to the elastic part F_{ne} and to the damping contact force F_{nd}

$$F_n = F_{ne} + F_{nd}\,. \tag{3.15}$$

The damping is used to decrease oscillations of the contact forces and to dissipate kinetic energy.

The elastic part of the normal contact force F_{ne} is proportional to the normal stiffness k_n and the penetration of the two particle surfaces u_{rn}

$$F_{ne} = k_n u_{rn}\,. \tag{3.16}$$

The penetration is calculated as

$$u_{rn} = d - r_1 - r_2\,, \tag{3.17}$$

where d is the distance of the particle centres, and r_1, r_2 their radii. In the formulation used in the present study no cohesion is allowed, so no tensile normal contact forces are allowed

$$F_{ne} \leq 0\,. \tag{3.18}$$

If $u_{rn} < 0$, the formula (3.16) is valid, otherwise $F_{ne} = 0$.

The contact damping force is assumed to be of viscous type

$$F_{nd} = c_n v_{rn} \tag{3.19}$$

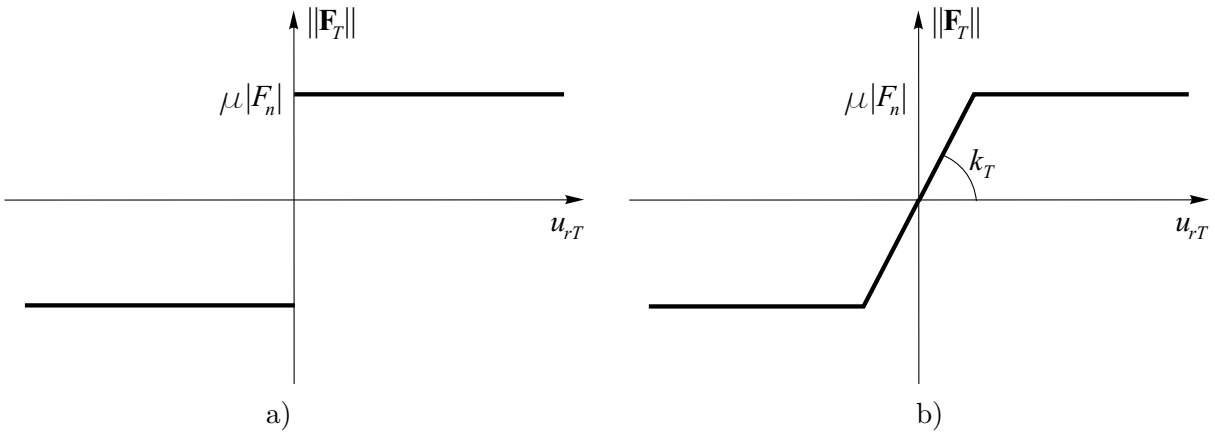

Figure 3.4: Friction force vs. relative tangential displacement a) Coulomb law, b) regularized Coulomb law

proportional to the normal relative velocity v_{rn} of the centres of the two particles in contact

$$v_{rn} = (\dot{\mathbf{u}}_2 - \dot{\mathbf{u}}_1) \cdot \mathbf{n}\,. \tag{3.20}$$

The value of damping c_n can be taken as a fraction of the critical damping C_{cr} for the system of two rigid bodies with masses m_1 and m_2, connected with a spring of the stiffness k_n (cf. [13])

$$C_{cr} = 2\sqrt{\frac{m_1 m_2 k_n}{m_1 + m_2}}\,. \tag{3.21}$$

3.2.3 Tangential frictional contact

In the absence of cohesion (if the particles were not bonded at all or after the cohesive bond has been broken) the tangential reaction $\mathbf{F}_T$ is brought about by friction opposing the relative motion at the contact point. The relative tangential velocity at the contact point $\mathbf{v}_{rT}$ is calculated from the following relationship

$$\mathbf{v}_{rT} = \mathbf{v}_r - \mathbf{v}_r \cdot \mathbf{n}\,, \tag{3.22}$$

$$\mathbf{v}_r = (\dot{\mathbf{u}}_2 + \boldsymbol{\omega}_2 \times \mathbf{r}_{c2}) - (\dot{\mathbf{u}}_1 + \boldsymbol{\omega}_1 \times \mathbf{r}_{c1})\,, \tag{3.23}$$

where $\dot{\mathbf{u}}_1$, $\dot{\mathbf{u}}_2$, and $\boldsymbol{\omega}_1$, $\boldsymbol{\omega}_2$ are the translational and rotational velocities of the particles, and $\mathbf{r}_{c1}$ and $\mathbf{r}_{c2}$ are the vectors connecting particle centres with contact points.

The relationship between the friction force $\|\mathbf{F}_T\|$ and relative tangential u_{rT} displacement for the classical Coulomb model (for a constant normal force F_n) is shown in Fig. 3.4a. This relationship would produce non physical oscillations of the friction force in the numerical solution due to possible changes of the direction of sliding velocity. To prevent this the Coulomb friction model must be regularized. A possible

regularization procedure involves decomposition of the tangential relative velocity into a reversible and irreversible parts, $\mathbf{v}_{rT}^{\mathrm{r}}$ and $\mathbf{v}_{rT}^{\mathrm{ir}}$, respectively:

$$\mathbf{v}_{rT} = \mathbf{v}_{rT}^{\mathrm{r}} + \mathbf{v}_{r}^{\mathrm{ir}} \,. \tag{3.24}$$

This is equivalent to formulation of the frictional contact as a problem analogous to that of elastoplasticity, which can be seen clearly from the friction force-tangential displacement relationship in Fig. 3.4b. This analogy allows us to calculate the friction force employing the radial return algorithm analogous to that used in elastoplasticity. First a trial state is calculated

$$\mathbf{F}_T^{\mathrm{trial}} = \mathbf{F}_T^{\mathrm{old}} - k_T \mathbf{v}_{rT} \Delta t \,, \tag{3.25}$$

and then the slip condition is checked

$$\phi^{\mathrm{trial}} = \|\mathbf{F}_T^{\mathrm{trial}}\| - \mu |F_n| \,. \tag{3.26}$$

If $\phi^{\mathrm{trial}} \leq 0$, we have the case of stick contact and the friction force is assigned the trial value

$$\mathbf{F}_T^{\mathrm{new}} = \mathbf{F}_T^{\mathrm{trial}} \,, \tag{3.27}$$

otherwise (slip contact) a return mapping is performed

$$\mathbf{F}_T^{\mathrm{new}} = \mu |F_n| \frac{\mathbf{F}_T^{\mathrm{trial}}}{\|\mathbf{F}_T^{\mathrm{trial}}\|} \,. \tag{3.28}$$

3.3 Background damping

A quasi-static state of equilibrium of the assembly of particles can be achieved by application of adequate damping. Described previously contact damping is a function of the relative velocity of contacting body. It is sometimes necessary to apply damping for non-contacting particles to dissipate their energy. There are two types of such damping, referred here as background, implemented in our formulation, one of viscous type and the other of non-viscous type. In both cases damping terms $\mathbf{F}_i^{\mathrm{damp}}$ and $\mathbf{T}_i^{\mathrm{damp}}$ are added to equations of motion (3.1) and (3.2)

$$m_i \ddot{\mathbf{u}}_i = \mathbf{F}_i + \mathbf{F}_i^{\mathrm{damp}} \,, \tag{3.29}$$

$$I_i \dot{\boldsymbol{\omega}}_i = \mathbf{T}_i + \mathbf{T}_i^{\mathrm{damp}} \,. \tag{3.30}$$

with damping terms given by:

- for viscous damping

$$\mathbf{F}_i^{\mathrm{damp}} = -\alpha^{vt} m_i \dot{\mathbf{u}}_i \,, \tag{3.31}$$

$$\mathbf{T}_i^{\mathrm{damp}} = -\alpha^{vr} I_i \boldsymbol{\omega}_i \,, \tag{3.32}$$

- for non-viscous damping

$$\mathbf{F}_i^{\mathrm{damp}} = -\alpha^{nvt} \|\mathbf{F}_i\| \frac{\dot{\mathbf{u}}_i}{\|\dot{\mathbf{u}}_i\|} \,, \tag{3.33}$$

$$\mathbf{T}_i^{\mathrm{damp}} = -\alpha^{nvr} \|\mathbf{T}_i\| \frac{\boldsymbol{\omega}_i}{\|\boldsymbol{\omega}_i\|} \,. \tag{3.34}$$

where α^{vt}, α^{vr}, α^{nvt} and α^{nvr} are respective damping constants. It can be seen from Eqs. (3.31)–(3.34) that non-viscous like viscous damping is opposite to velocity, the difference consists in the evaluation of the magnitude of damping force – viscous damping is proportional to the magnitude of velocity, while non-viscous damping is proportional to the magnitude of resultant force and moment.

3.4 Numerical stability

Explicit integration in time yields high computational efficiency. Therefore the method enables us to analyse large models. The known disadvantage of the explicit integration scheme is its conditional numerical stability imposing the limitation on the time step Δt. The time step Δt must not be larger than a critical time step Δt_{cr}

$$\Delta t \leq \Delta t_{\mathrm{cr}} \tag{3.35}$$

determined by the highest natural frequency of the system $\omega_{\max}$

$$\Delta t_{\mathrm{cr}} = \frac{2}{\omega_{\max}} \,. \tag{3.36}$$

If damping exists, the critical time increment is given by

$$\Delta t_{\mathrm{cr}} = \frac{2}{\omega_{\max}} \left(\sqrt{1+\xi^2} - \xi \right) \,, \tag{3.37}$$

where ξ is the fraction of the critical damping corresponding to the highest frequency $\omega_{\max}$. Exact determination of the highest frequency $\omega_{\max}$ would require solution of the eigenvalue problem defined for the whole system of connected rigid particles. In an approximate solution procedure, eigenvalue problems can be defined separately for every rigid particle using the linearized equations of motion

$$\mathbf{m}_i \ddot{\mathbf{r}}_i + \mathbf{k}_i \mathbf{r}_i = \mathbf{0} \,, \tag{3.38}$$

where

$$\mathbf{m}_i = \{m_i \; m_i \; m_i \; I_i \; I_i \; I_i\}^{\mathrm{T}} \,, \quad \mathbf{r}_i = \{(u_x)_i \; (u_y)_i \; (u_z)_i \; (\theta_x)_i \; (\theta_y)_i \; (\theta_z)_i\}^{\mathrm{T}} \,, \tag{3.39}$$

and $\mathbf{k}_i$ is the stiffness matrix accounting for the contributions from all the penalty constraints active for the i-th particle. Equation (3.39) defines the vectors $\mathbf{m}_i$ and $\mathbf{r}_i$ for a spherical particle in three-dimensional space. For a cylindrical particle in a two-dimensional model the respective vectors are defined as follows:

$$\mathbf{m}_i = \{m_i \; m_i \; I_i\}^{\mathrm{T}} \,, \quad \mathbf{r}_i = \{(u_x)_i \; (u_y)_i \; (\theta_z)_i\}^{\mathrm{T}} \,. \tag{3.40}$$

Equation (3.38) leads to an eigenproblem

$$\mathbf{k}_i \mathbf{r}_i = \lambda_j \mathbf{m}_i \mathbf{r}_i \,, \tag{3.41}$$

where eigenvalues λ_j ($j = 1, \ldots, 6$ in 3D case, and $j = 1, 2, 3$ for 2D case) are the squared frequencies of free vibrations:

$$\lambda_j = \omega_j^2 \,. \tag{3.42}$$

In a 3D problem, three of six frequencies ω_j are translational, and the other three – rotational.

In the algorithm implemented, a further simplification is assumed. The maximum frequency is estimated as the maximum of natural frequencies of mass–spring systems defined for all the particles with one translational and one rotational degree of freedom. The translational and rotational free vibrations are governed by the following equations:

$$m_i \ddot{u}_n + k_n u_n = 0 \,, \tag{3.43}$$

$$I_i \ddot{\theta} + k_\theta \theta = 0 \,, \tag{3.44}$$

where it is assumed that the translational motion is due to the contact interaction in the normal direction (the spring stiffness k_n represents the penalty stiffness in the normal direction), and the rotational stiffness is due to the contact stiffness (penalty) in the tangential direction. Given the tangential penalty k_T, it can be shown that the rotational stiffness k_θ can be obtained as

$$k_\theta = k_T r^2 \,, \tag{3.45}$$

where r is the length of the vector connecting the mass centre to the contact point.

The natural frequency of the translational vibrations is given by the following equation:

$$\omega_n = \sqrt{\frac{k_n}{m_i}} \,, \tag{3.46}$$

while the rotational frequency ω_θ can be obtained from the formula

$$\omega_\theta = \sqrt{\frac{k_\theta}{I_i}} \,. \tag{3.47}$$

With the rotational inertia of a sphere

$$I = \frac{2}{5} m r^2 \tag{3.48}$$

and k_θ given by Eq. (3.45), the rotational frequency can be calculated as

$$\omega_\theta = \sqrt{\frac{5 k_T}{2 m_i}} \,. \tag{3.49}$$

If $k_T = k_n$, the rotational frequency ω_θ is considerably higher than the translational frequency ω_n obtained from Eq. (3.46), which results in a smaller critical time increment, cf. Eq. (3.36). To avoid the determination of a critical time step by the rotational frequencies, the rotational inertia terms are scaled adequately. The concept of scaling rotational inertia terms is commonly used for shell elements, cf. [14].

3.5 Contact detection

Changing contact pairs of elements during the analysis process must be automatically detected. The simple ("brute-force") approach to identify interaction pairs by checking every sphere against every other sphere would be very inefficient, with the computational time proportional to n^2 (of order $O(n^2)$), where n is the number of elements.

A number of more effective methods has been developed to determine the particle interaction. An overview of contact detection methods developed for discrete element method can be found in [9] and [15]. In usually used contact detection schemes prior to the contact resolution objects are spatially ordered using an appropriate sorting algorithm, cf. [9]. Spatial sorting enables efficient determination of neighbouring objects, so the subsequent contact check can be limited to the pairs of objects lying close to each other.

In the absence of cohesion the contact is found if the penetration between two bodies is found. In case of spheres or cylinders this is expressed by the simple condition

$$u_{rn} \leq 0 \,, \tag{3.50}$$

where u_{rn} is calculated according to the formula (3.17). If cohesive bonds are active the interaction between the spheres can also occur if $u_{rn} > 0$. The condition (3.50) is then replaced by

$$u_{rn} \leq u^+_{rn,max} \,, \tag{3.51}$$

where $u^+_{rn,max}$ is the separation of two spheres or cylinders corresponding to the complete breakage of cohesive bonds, which must be evaluated for a given constitutive model and material properties.

Since the verification of the contact condition (3.50) or (3.51) is simple, we can say, that basically the effectiveness of the contact detection scheme in our case depends on the effectiveness of the sorting algorithm.

Various spatial sorting algorithms are known. Most popular of them can be classified into following groups:

- grid subdivision (Löhner [16])
- binary trees (Knuth [17], Bonet [18])
- quad-trees (in 2D) and octrees (in 3D) (Knuth [17], Samet [19])
- body based cells (Greengard [20])
- spatial heapsort (Williams [9])

Grid subdivision

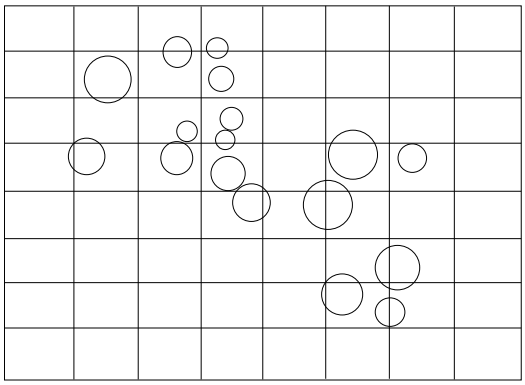

Figure 3.5: Grid subdivision

The problem domain in this method is discretized into equal rectangular (in 2D) or hexahedral (in 3D) cells shown in Fig. 3.5 for 2D case. Cells are sometimes called bins, cf. [16]. Objects are associated with cells (bins) based on their coordinates. The performance of this method depends on the trade-off between the cell size and the number of objects per cell. The efficiency of this method is assured if the objects are evenly distributed among cells. Adaptive grid method can be employed in case if the distribution of the objects is not uniform.

Binary trees

An effective sorting technique for an uneven space distribution of objects is based on the binary tree structures. The main concept of this scheme is shown in Fig. 3.6. The

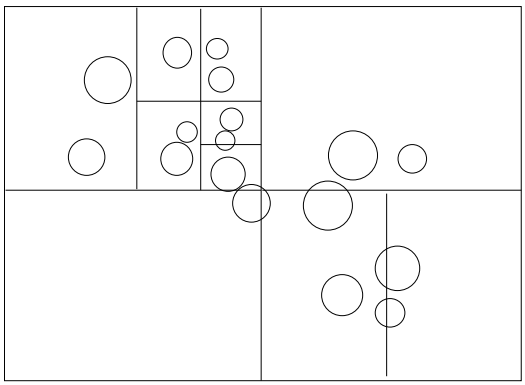

Figure 3.6: Binary trees

domain with objects is divided into rectilinear cells which has maximum 2 objects. In case the number of objects exceeds 2 the cell is subdivided into two cells. The subdivision is usually done alternately along x, y and z axes, cf. [18]. The domain with objects discretized in this way is represented by a binary tree. The structure allows us to identify easily objects lying in a particular subdomain by traversing the tree from the top downwards. The cost of this search is of order $O(N \log_2 N)$.

Quadtrees and octrees

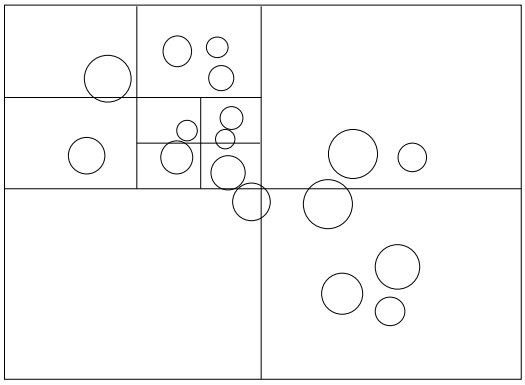

Figure 3.7: Quadtree sorting

Another effective sorting technique for an uneven space distribution of objects is based on quadtree (2D) and octree (3D) structures. The main concept of the quadtree sorting is shown in Fig. 3.7. In the quadtree sorting scheme a 2D domain with objects is divided into rectilinear cells (quads) with up to 4 objects assigned. In case the number of objects exceeds 4, the cell is subdivided into four cells (quads), and the objects relocated into new cells. The domain with objects discretized in this way is

represented by a quad-tree. The structure allows us to identify easily objects lying in a particular subdomain by traversing the quadtree from the top downwards. The cost of this search is of order $O(N \log_4 N)$.

Extension of the quadtree scheme on on the octree scheme for 3D contact search is straightforward. Now a 3D domain is discretized recursively into brick cells (octants) with up to eight objects. In the number of objects in an octant exceeds eight, the octant is subdivided into eight cells, and the objects are assigned to these cells. Objects lying in a particular subdomain are found by traversing the octree from the top downwards. The cost of this search is of order $O(N \log_8 N)$.

This method will be used in our search algorithm combined with body based cells.

Body based cells

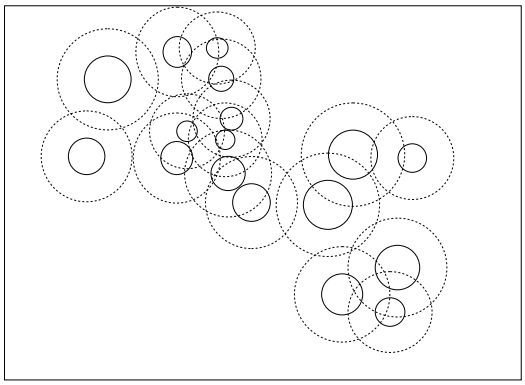

Figure 3.8: Body based cells

Another search scheme takes advantage of the assumption that object configuration evolves slowly and the new contacts can be formed only between objects that are sufficiently close at a certain stage. The list of potential contacts for each object includes the objects lying within a cell surrounding an object under consideration. The concept of this method is presented graphically in Fig. 3.8. This method will be used in our search algorithm combined with quadtree and octree sorting scheme.

Spatial heapsort

The basis of spatial heapsort method is sorting of the objects according to their co-ordinates, cf. [9]. Sorted objects are stored in a binary tree structure. Heapsort is of order $O(N \log_2 N)$

3.6 Contact search algorithm

In our formulation the contact search is based on the quad-tree and octree sorting coupled with the body based cell technique.

Building octree or quad-tree structures at every time step can be quite expensive. Since time steps are very small, most of contacting pairs can be the same as those in the previous step. Using the information about contact pairs existing in the previous step can speed up the contact search. Therefore the algorithm of contact detection scheme consists of two stages: (i) global search, identifying the pairs of potential contacts, based on the quadtree and octree sorting, (ii) local search, verifying the list of potential contacts (typical for body based cell algorithm).

Stage 1: Global search

Balls are ordered in space using octree or quad-tree structures. A list of existing and potential contact pairs is created. In the list of potential contacting balls the body based cell concept is employed, each object has a circular or spherical cell assigned and neighbouring objects lying within the cell or intersecting it are included into the list of potential contacts.

Global search with a quad-tree (or octree) structure being rebuilt and the list of contacting balls being updated is performed every certain number of steps.

Stage 2: Local search

Local search is done at each time step. Contact conditions for the ball pairs from the list of potential contacts are verified and actual contacting pairs are found.

The body cell radius is assumed to be equal to the sphere/cylinder radius increased by a constant distance which is a function of a user defined parameter c_{tol} (Fig. 3.9a). This parameter determines the length of the list of potential contacts and the frequency of global search (updating the list of potential contacts).

New potential contacts are added to the list if the separation between two balls is smaller than $2\sqrt{2}c_{\text{tol}}$ in two-dimensional problem and $2\sqrt{3}c_{\text{tol}}$ in three-dimensional problem. Conversely if the separation in an existing contact pair gets larger than these distances the contact pair is deleted from the list.

Global search interval is determined by monitoring the maximum displacement component of any ball accumulated from the time of last contact search

$$u_{\max} = \max_{\substack{i=1,n_d \\ n=1,\,N_B}} \left(u_i^{(n)} \right) \tag{3.52}$$

where n_d is the dimension of the problem ($n_d = 2$ for two-dimensional problem and $n_d = 3$ for three-dimensional problem) and N_B is the number of balls. If displacement

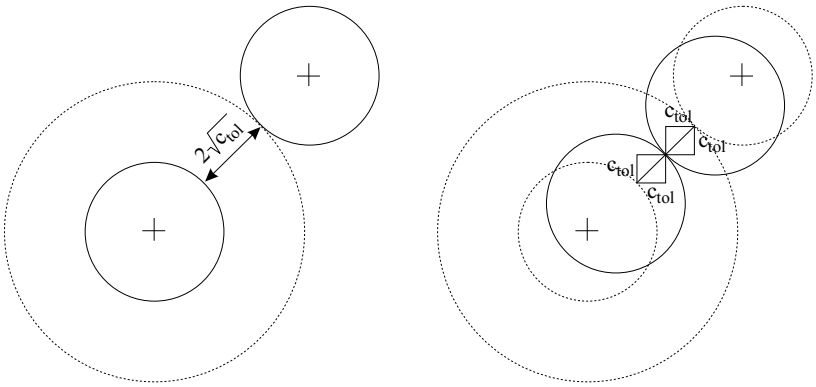

a) b)

Figure 3.9: Updating potential contact pairs, a) limit separation of two balls during global search, b) maximum permitted displacement between update of list of potential contacts

of any ball along any axes exceeds a user defined distance c_{tol}, cf. Fig. 3.9b,

$$u_{\max} > c_{\text{tol}} \tag{3.53}$$

then the global contact search is performed and the list of contacts is updated.

The contact detection algorithm developed has been found to be very efficient allowing us to use it for large particle systems. The user defined distance c_{tol} has big influence on the efficiency of the analysis. The bigger it is the most seldom is global search and updating of the list of potential contacts, but at the same time the longer the list is. The longer the list the most time is spent at each time step on verification of contact. A certain optimum value of c_{tol} has to be found. In our calculations we usually used $c_{\text{tol}} = (0.1 \div 0.5)r$, where r is the average radius of the balls.

3.7 Numerical implementation – programming aspects

Computer implementation of discrete elements is based on data structures that allow flexible and efficient treatment of changing contact conditions. Discrete element database structure is based on dynamic linked lists which are presented graphically in Fig. 3.10.

Computer program is coded in Fortran 90. Data structure for the basic ball entity which is used to create the linked list is defined by the following derived type:

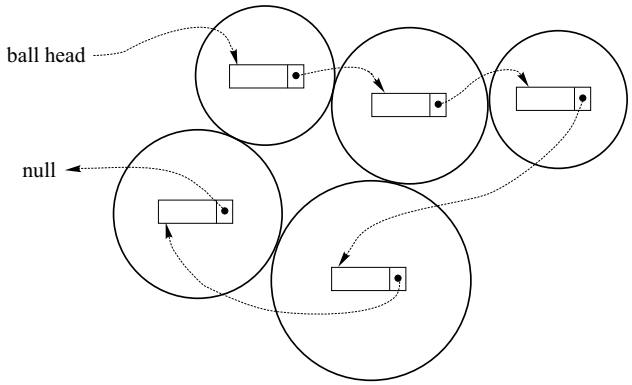

Figure 3.10: Linked list of balls

```
TYPE ball
  INTEGER (kind=4) :: &
    lnode, &      ! node label
    matno         ! material ID
  REAL (kind=8) :: &
    radius, &     ! ball radius
    mass          ! ball mass
  TYPE (ball), POINTER :: next
END TYPE ball
```

A linked list enables us to add and delete balls easily if necessary. The basic information stored for each ball consisted of ball label, radius and mass as well as property identification number. Treatment of contact according to the algorithm presented earlier requires some additional information for each ball.

Information about existing and potential contacting pairs must be stored. This information is stored in the form of a linked list of entities that are called contacts. The structure of the contact entity is as follows:

```
TYPE contact
  TYPE (ball), POINTER :: c_ball1, &  ! 1st ball in the contact pair
                          c_ball2     ! 2nd ball in the contact pair
  INTEGER (kind=4) :: &
    bflag, &     ! contact bond flag, 0 - no bond, 1 - bond is active
    broken       ! contact bond broken flag, 1 - broken, 0 - otherwise
  REAL (kind=8) :: &
    fn,      &      ! normal contact force
    ft(3),   &      ! tangential contact force
    gap0,    &      ! initial gap/penetration
    r01(3),  &      ! vector center of b1 to contact point at t=0
```

```
    r02(3),  &      ! vector center of b2 to contact point at t=0
  TYPE (contact), POINTER :: &
    c_b1clist, &    ! next cont. around 1st ball
    c_b2clist  &    ! next cont. around 2nd ball
    next            ! pointer to next contact in global list
END TYPE contact
```

The two global lists, that of balls and that of contacts, are connected with each other. Pointers `c_ball1` and `c_ball2` of contact entities point on elements of global list of balls. The connection in the opposite direction is formed by pointers `b_clist`, which is added to the structure of ball and points on the head of the list of contacts around a given ball.

```
TYPE ball
  INTEGER (kind=4) :: &
    lnode, &      ! node label
    matno         ! material ID
  REAL (kind=8) :: &
    radius, &     ! ball radius
    mass, &       ! ball mass
    wear, &       ! wear thickness
  TYPE (contact), POINTER :: b_clist ! header of contacts around ball
  TYPE (ball), POINTER :: next
END TYPE ball
```

Global linked lists of balls and of contacts are presented graphically in Fig. 3.11. Connections between global lists of balls and contacts as well as local lists of contacts around each ball are shown in Fig. 3.12.

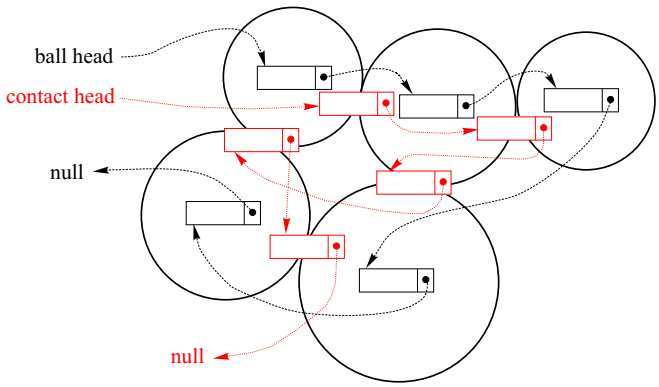

Figure 3.11: Global linked lists of balls and contacts

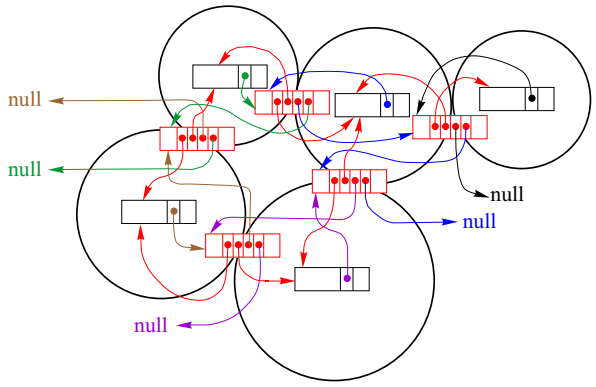

Figure 3.12: Local linked lists of contacts around balls

Presented structure of the discrete element database allows us to verify efficiently existing contacts, extract contacts around each ball, eliminate elements from the lists (both balls and contacts). New elements can also be added to the lists efficiently. Elimination of balls is carried out for balls representing "worn out" particles. Elimination and adding new contacts is carried out every certain time when contact search is done. When a certain ball is eliminated all the contact around this ball are eliminated from the list of contacts as well.

Chapter 4

Micromechanical models with cohesion

This section reviews micromechanical models defining contact interface behaviour for discrete element models of soil and rock materials. Model of the contact interface presented in Section 3.2 takes into account normal compressive interaction and tangential frictional forces. Modelling soil and rock materials requires consideration of cohesion between particles. Cohesive bonds allow tensile normal contact force as well as yield tangential reaction.

Contact models with cohesion implemented in the program Stampack range from the simple elastic perfectly brittle model to the most general elasto-plastic constitutive model developed by the University of Padova.

4.1 Elastic perfectly brittle contact model

The elastic perfectly brittle contact model is characterized with linear elastic behaviour when cohesive bonds are active and with instantaneous breakage of these bonds when the interface strength is exceeded. When two particles are bonded the contact forces in both normal and tangential directions are calculated from the linear constitutive relationships:

$$\sigma = k_n u_n \,, \tag{4.1}$$

$$\tau = k_t \, u_t \,, \tag{4.2}$$

where:

σ — normal contact force,

τ — tangential contact force,

k_n — interface stiffness in the normal direction,

k_t — interface stiffness in the tangential direction,

u_n — normal relative displacement,

u_t — tangential relative displacement.

Cohesive bonds are broken instantaneously when the interface strength is exceeded in the tangential direction by the tangential contact force or in the normal direction by the tensile contact force. The failure (decohesion) criterion can be written as:

$$\sigma \leq R_n \,, \tag{4.3}$$

$$\|\tau\| \leq R_t \,, \tag{4.4}$$

where:

R_n — interface strength in the normal direction,

R_t — interface strength in the tangential direction.

In the absence of cohesion the normal contact force can be compressive only:

$$\sigma \leq 0 \tag{4.5}$$

and tangential contact force can be nonzero due to friction

$$\|\tau\| = \mu|\sigma| \tag{4.6}$$

if $\sigma < 0$ or zero otherwise. The friction force is given by Eq. (4.6) expressing the Coulomb friction law, with μ being the Coulomb friction coefficient.

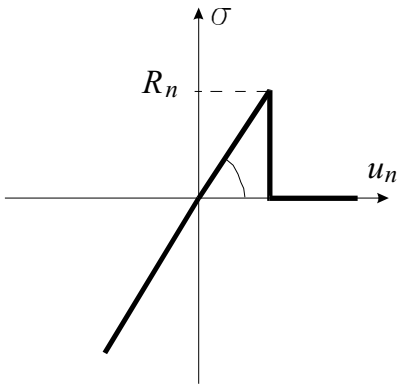

Figure 4.1: Normal contact force in the elastic perfectly brittle model

Contact laws for the normal and tangential direction for the elastic perfectly brittle model are shown in Figs. 4.1 and 4.2, respectively. The failure surface for the elastic perfectly brittle model defined by conditions (4.3) and (4.4) is shown in Fig. 4.3.

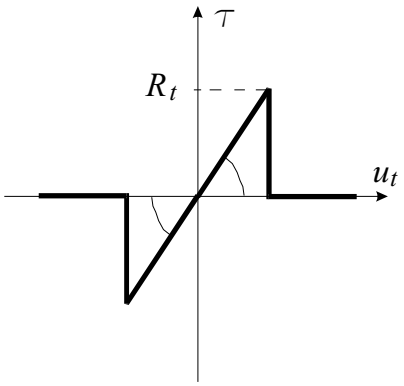

Figure 4.2: Tangential contact force in the elastic perfectly brittle model (tensile normal contact force)

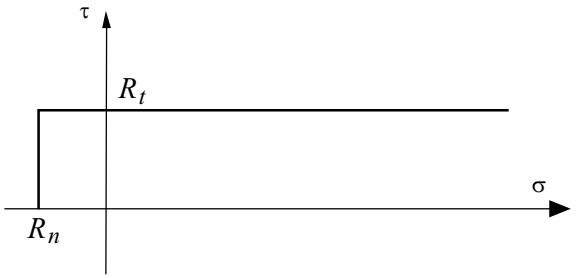

Figure 4.3: Failure surface for the elastic perfectly brittle model

4.2 Elasto-plastic contact model with nonlinear softening

This section summarizes the theoretical formulation of the constitutive model for geomaterials developed in the University of Padova which has been presented in more detail in the First Year Activity Report.

A contact law relates the contact force acting between two spheres to their relative displacement. The model developed is based on the nonlinear elasto-plastic relationships established for the normal and tangential direction

$$\sigma_i = k_i(u_i - u_i^p)\,, \quad i = n, t \tag{4.7}$$

where:

σ_i — normal or tangential contact force;

u_i — total relative displacement;

u_i^p — plastic component of the relative displacement;

k_i — elastic parameters, which characterize contact interface stiffness

n, t — normal and tangential direction;

Two separate different potential functions: one for the normal and another for the tangential stress-strain relation are adopted. A general non-linear one-dimensional yield criterion has been taken in the following form:

$$f(\sigma, \alpha) = |\sigma| - [\sigma_Y + H(\alpha)] \,, \tag{4.8}$$

where $H(\alpha)$ is the function of the plastic strain and it is expressed as a function of the softening or hardening parameter α, the so called internal hardening variable. Two different forms of $H(\alpha)$ can be chosen:

1. parabolic
$$H(\alpha) = b_1 \alpha^2 + b_2 \alpha + b_3 \,, \tag{4.9}$$
2. hyperbolic (used only for tangential direction)
$$H_t(\alpha) = \frac{b_1 \alpha_t^d}{b_2 + b_3 \alpha_t^d} \,, \tag{4.10}$$

where b_1, b_2, b_3 and m are parameters defining plastic function, defined separately for tension, compression and shear action. The variation of constants defining $H(\alpha)$ changes significantly the shape of the yield surface and allows us to apply the model to different soils and rocks.

Dependence of the tangential force on the normal force is expressed by the application of a two-dimensional failure criterion. In the proposed criterion the slip between two surfaces of a continuum is assumed to occur when the shear stress τ on any plane at a point in the soil material reaches a so-called critical value. This value depends non-linearly upon the normal stress in the same plane. In the numerical implementation at each step the value of the normal force is fixed and a two-dimensional yield surface is used in order to establish the elastic range of the tangential force, as shown in Fig. 4.4.

The basic concept of the strength criterion is that the shear strength of a rock material is made up of two parts varying with the normal stress: an elastic "cohesive" part and a frictional plastic part. The shear strength can be mathematically resumed as follow:

$$\tau = f(u_t, u_t^p) + f^1(\sigma_n, H) \,, \tag{4.11}$$

where:

τ — critical tangential contact force;

σ_n — normal contact force;

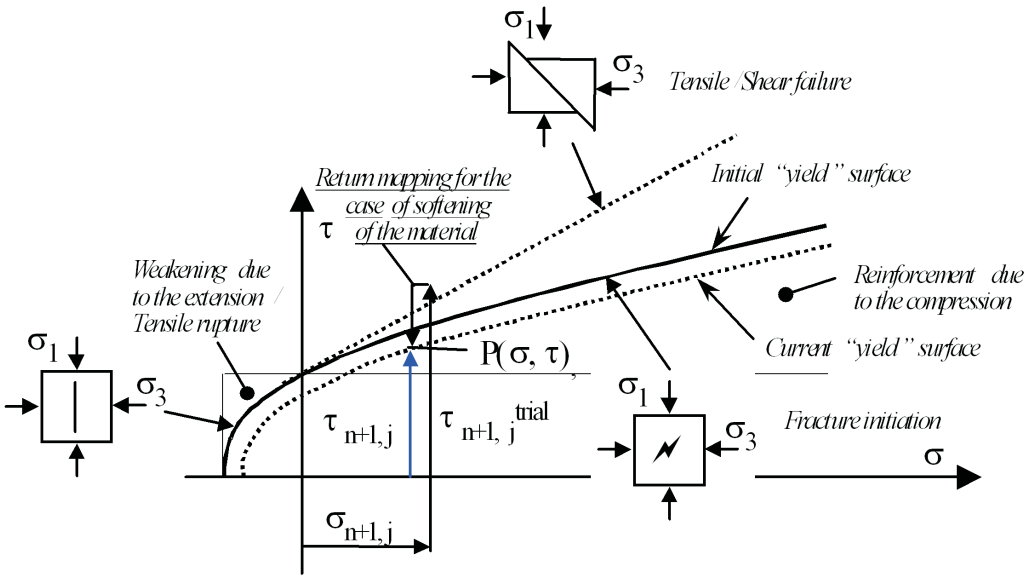

Figure 4.4: Scheme of application of the 2D yield surface in return mapping algorithm for one-dimensional constitutive law

u_t, u_t^p — tangential total and plastic relative displacements, respectively;

H — general non-linear function of plasticity.

The cohesive part of the formulation is non-linear elastic regarding the shear modulus: in fact it was experimentally noticed that for some soils, such as the stiff clay, the slope of the shear-normal stresses relationship changes when the normal applied stress increases or decreases. Moreover it was deducted that there is a sort of contribute which affects the real value of the shear modulus of the material. In this way it is possible to explain the heavy dependency on the normal applied load.

The plastic softening (or hardening) frictional behavior starts after that the value of τ reaches the limit flow stress value, which is a function of the normal applied stress. As experimentally observed, if the normal applied stress increases, also the tangential peak stress increases. Due to the previous considerations the equation (4.11) can be more specifically rewritten as follows

$$\tau = k_t(\sigma_n)(u_t - u_t^p) - [n(\sigma_n) + H^1(\alpha)]\,, \tag{4.12}$$

where:

α — internal hardening variable,

$n(\sigma_n)$ — parameter which delimits the flow range,

k_t — shear modulus of the contact interface, and it depends on the applied normal contact force

$$k_t = m\sqrt[3]{||\sigma_n| - r|}\,, \tag{4.13}$$

where m and r are constants which depend on the material.

The parameter $n(\sigma_n)$ in this case it is represented as function of the normal stress and is expressed trough two terms:

$$n(\sigma_n) = \eta(\sigma_n + c)\,. \tag{4.14}$$

This formulation of $n(\sigma_n)$ was chosen in order to reproduce the behavior of a cohesive soil that presents the characteristic of increasing the shear strength by increasing the normal applied stress. This behavior is characteristic of a wide range of soils, from sand to some soft rock. The material parameters η and c are constant during the loading process and they respectively represent:

η — parameter that gives a contribute to the frictional behavior of the material;

c — is a constant which correlates the cohesive properties of the material.

Flow rule

The plastic strain increments for both the formulations (i.e. the normal and tangential strain) are calculated from the following flow rule:

$$\dot{u}^p = \gamma\,\mathrm{sign}(\sigma)\,, \tag{4.15}$$

where

γ — absolute value of the slip rate ($\gamma > 0$);

$\dot{u}^p$ — derivative of the plastic relative displacement (normal or tangential);

σ — contact force in the normal or tangential direction.

4.3 Simplified elasto-plastic contact model with softening

A special case of the previously presented elasto-plastic contact formulation has been taken using the following simplifying assumptions:

1. Elasto-plastic contact law with linear softening is assumed for shear and normal tensile contact forces
2. Elastic linear law is assumed for compression

3. Contact stiffness (elastic modulus) in the tangential direction is constant and independent of normal contact force

Simplified contact laws for the normal and tangential direction are shown in Figs. 4.5 and 4.6, respectively.

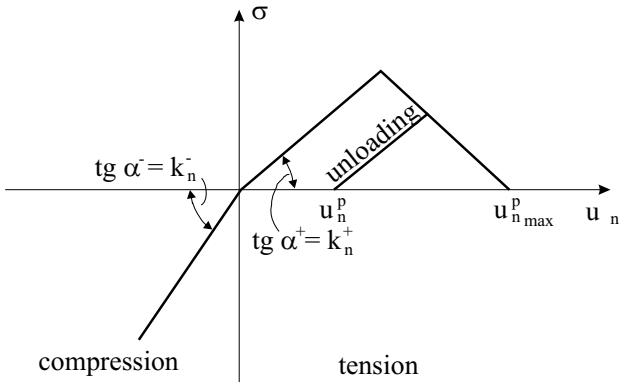

Figure 4.5: Simplified elasto-plastic contact law for the normal direction

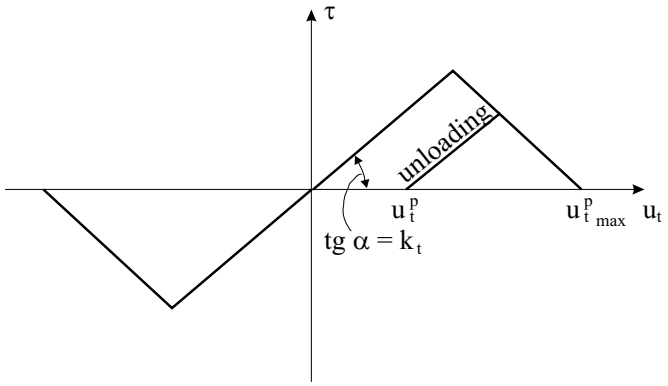

Figure 4.6: Simplified elasto-plastic contact law for the tangential direction

The softening function $H(\alpha)$ given by Eq. (4.9) is now simplified to

$$H(\alpha) = b_2\alpha = -H'u^p\,, \tag{4.16}$$

where H' is the constant softening modulus (assumed positive value) and the plastic part of the relative displacement u^p taken as the softening parameter α.

Contact yield condition for the simplified model is shown in Fig. 4.7. Yielding of contact bonds can occur under a combined tension and shear action (if the normal contact force is tensile) or due to shear only (if the normal contact force is compressive). After contact bonds are broken due to yielding standard frictional contact can occur between the spherical elements.

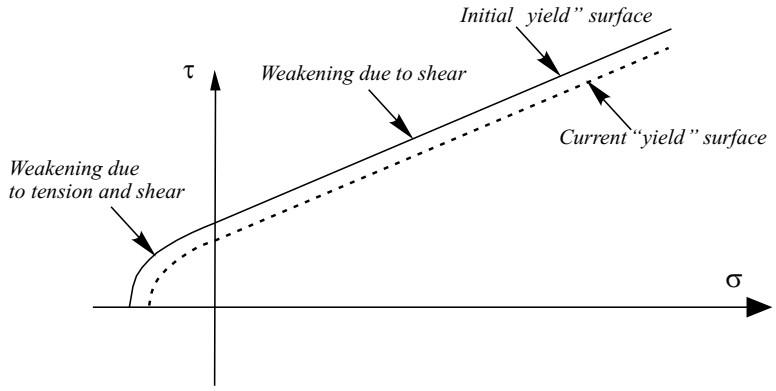

Figure 4.7: Contact yield condition for simplified model

4.4 Contact model with elastic damage

This model can be considered as a generalization of the elastic perfectly brittle model in place of brittle failure a certain softening slope defined by softening modulus H is introduced into the force-displacement relationship (Fig. 4.8).

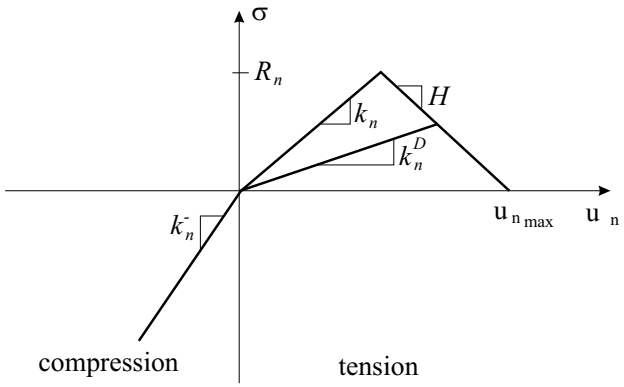

Figure 4.8: Normal contact force in the contact model with elastic damage

The constitutive relationship for 1D elastic damage is given by:

$$\sigma = k_n^D \, u_n = (1 - \omega) k_n u_n \tag{4.17}$$

where:

k_n^D — elastic damaged secant modulus,

ω — scalar damage variable.

Scalar damage variable ω is a measure of material damage, for undamaged state $\omega = 0$ and for damaged state $0 < \omega \leq 1$. Scalar damage variable ω can be written in the following form:

$$\omega = \frac{\psi(u_n) - 1}{\psi(u_n)} \tag{4.18}$$

where $\psi(u_n)$ is a function of total relative displacement. For linear strain softening $\psi(u_n)$ is defined by

$$\psi(u_n) = \begin{cases} 1 & \text{for} \quad u_n \leq \dfrac{R_n}{k_n} \\ \dfrac{k_n^2 u_n}{H R_n + k_n R_n - H k_n u_n} & \text{for} \quad \dfrac{R_n}{k_n} \leq u_n \leq \dfrac{R_n}{k_n} + \dfrac{R_n}{H} \\ \infty & \text{for} \quad u_n \geq \dfrac{R_n}{k_n} + \dfrac{R_n}{H} \end{cases} \tag{4.19}$$

where R_n is the initial tensile strength and H is the softening modulus (taken as positive).

Similar contact force–displacement law with damage (Fig. 4.9) can be introduced for the tangential direction. Then the bond decohesion can occur either due to tension or shear.

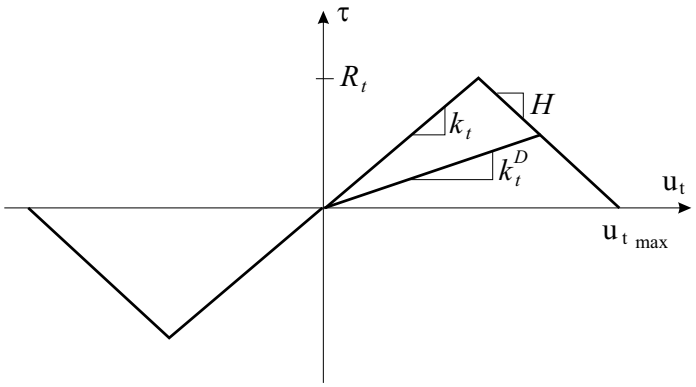

Figure 4.9: Tangential contact force in the contact model with elastic damage

An optional failure criterion has been implemented in this model with failure criterion based on the tensile contact force only. This criterion is supposed to model better fracture of brittle materials, as this macroscopic failure is explained by brittle rupture of atomic bonds in tension. This microscopic mechanism explains macroscopic strain softening behaviour both under compression or tension.

After contact bonds are broken due to damage ($\omega = 0$) standard frictional contact can occur between the spherical elements.

4.5 Contact model with friction, wear and heat generation

Contact model taking into account friction, wear and heat generation is used to model tool-rock/soil interaction. Cohesion is not included into the formulation of this model. Normal contact forces can be compressive only. Normal contact force σ is calculated from the linear relationships:

$$\sigma = k_n u_n \tag{4.20}$$

where $u_n \leq 0$ is the normal relative displacement (penetration of one sphere against another). Frictional contact force is evaluated using the regularized Coulomb law

$$\tau = \mu|\sigma| \tag{4.21}$$

where μ is the Coulomb friction coefficient. The frictional dissipation rate $\dot{D}$ is calculated as

$$\dot{D} = \tau v_t \tag{4.22}$$

where v_t is the relative tangential velocity. The frictional dissipation is used to calculate wear rate $\dot{w}$ and heat generated by friction Q_{gen}.

Heat generated by friction is equal

$$Q_{gen} = \chi \dot{D} \tag{4.23}$$

where χ is the part of the friction work converted to heat ($\chi \leq 1$). Heat generation through frictional dissipation is assumed to be absorbed equally by the two particles in contact.

Wear rate is calculated using the Archard law presented later on in Sec. 6.3.

4.6 Validation of micromechanical models

Micromechanical models have been implemented in the Stampack (program developed by CIMNE) and numerical implementation has been validated by running test examples of shear, tension and compression as well as of shear combined with tension and compression. This section presents results of the tests for the simplified elasto-plastic contact model with linear softening and the contact model with elastic damage. Numerical tests for the general elasto-plastic model with non-linear softening are presented in a separate section. Numerical tests presented here allowed us to use the program to model rock specimen. Results of material model calibration are presented in an annex to WP6.

Validation tests were carried out using a discrete element model of two discs (Fig. 4.10). The load was introduced under displacement control. The lower disc was fixed

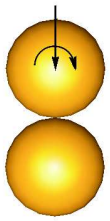

Figure 4.10: Discrete element micromechanical model

and translational motion was prescribed for the upper disc in order to obtain compression or tension at the contact interface between the discs. For the rotational motion prescribed for the upper disc the relative tangential displacement at the contact interface produced shear action at the interface. The combination of translation and rotation of the upper disc allowed us to obtain combined normal and tangential contact action. Parameters defining contact interface properties Contact interface is defined with the following parameters:

$k_n = 2 \cdot 10^{10}\text{N/m},$
$k_t = 10^5\text{N},$
$R_n = 10^5\text{N},$
$H = 10^{10}\text{N/m},$
$\mu = 0.839.$

4.6.1 Elasto-plastic contact model with linear softening

Simulation of pure tension, compression and shear

The normal and tangential force were calculated for pure tension, compression and shear. Loading was applied under displacement control. Variation of the normal contact force against the normal relative displacement under monotonic loading is shown in Fig. 4.11. The peak force of 100 kN is achieved for relative displacement 0.005 mm, and then the yielding of the contact bond occurs until complete breakage at separation of 0.015 mm. Figure 4.12 shows variation of the normal contact force under tensile loading with unloading and reloading which occurs with elastic modulus. Compressive normal force under monotonic loading is shown in Fig. 4.13. Compression is treated as an elastic process. Tangential contact force vs. tangential relative displacement under shear monotonic loading is shown in Fig. 4.14. Elastic increase of the tangential force and subsequent drop due to yielding can be observed.

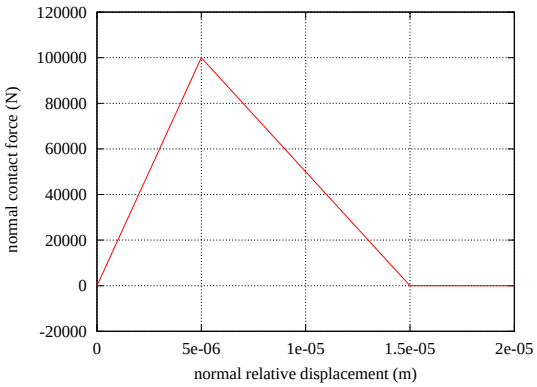

Figure 4.11: Normal contact force vs. normal relative displacement under monotonic tensile loading (elasto-plastic contact model with linear softening)

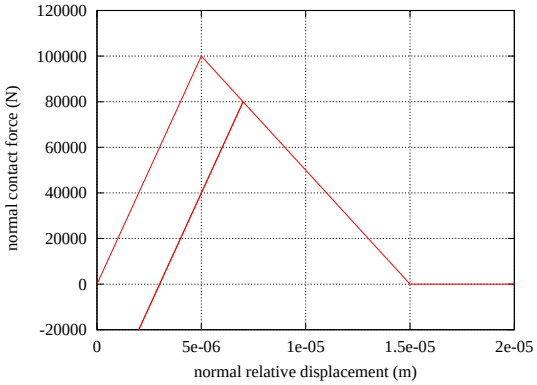

Figure 4.12: Normal contact force vs. normal relative displacement under tensile loading with unloading and reloading (elasto-plastic contact model with linear softening)

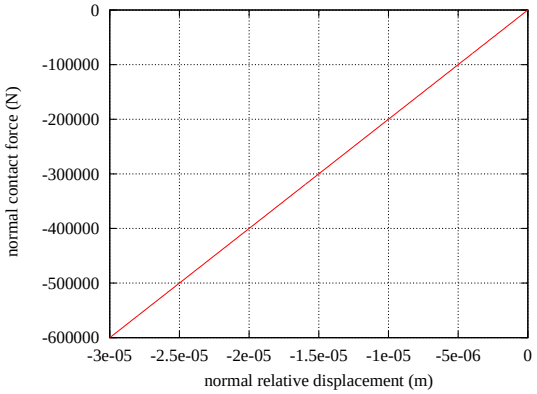

Figure 4.13: Normal contact force vs. normal relative displacement under compressive monotonic loading (elasto-plastic contact model with linear softening)

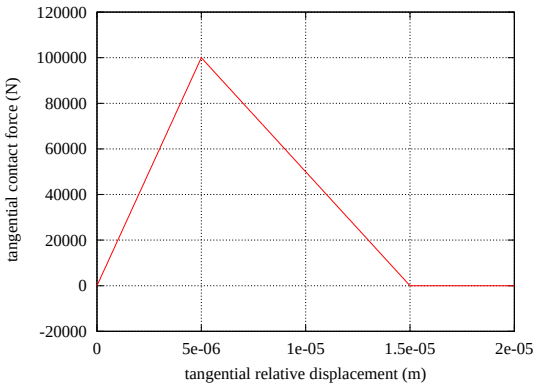

Figure 4.14: Tangential contact force vs. tangential relative displacement under shear monotonic loading (elasto-plastic contact model with linear softening)

Simulation of combined shear with tension and compression

The interface has been subjected to combined loading. Shear combined with compression or tension has been achieved by adequate prescribing translational and rotational motion. Relative translational velocity was 10 times higher than relative normal velocity. The normal compressive force is shown in Fig. 4.15 — it is calculated using the linear relationship. Figure 4.16 presents variation of tangential force along with increasing relative tangential velocity. It reaches its peak value and then drops due to strain softening until the failure when the elasto-plastic force is equal to friction force. Then the tangential force is calculated using the Coulomb law of friction.

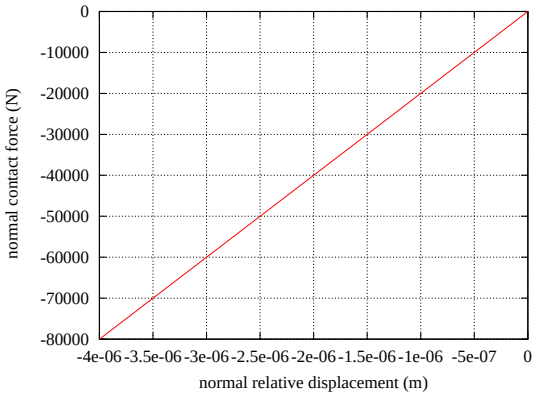

Figure 4.15: Normal contact force vs. normal relative displacement under shear combined with compression (elasto-plastic contact model with linear softening)

Tangential and normal contact forces versus respective relative displacements are shown in Figs. 4.17 and 4.18 for shear combined with tension. Tangential relative velocity was twice as high as normal one therefore final relative tangential displacement

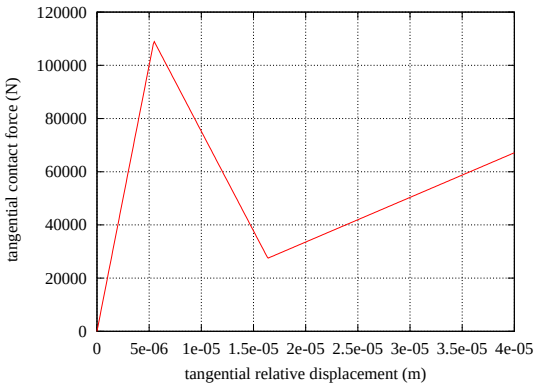

Figure 4.16: Tangential contact force vs. tangential relative displacement under shear combined with compression (elasto-plastic contact model with linear softening)

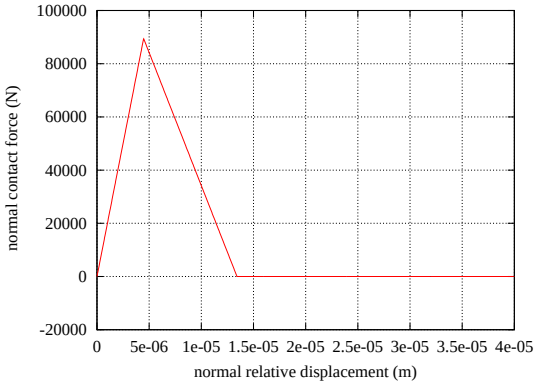

Figure 4.17: Normal contact force vs. tangential relative displacement under shear combined with tension (elasto-plastic contact model with linear softening)

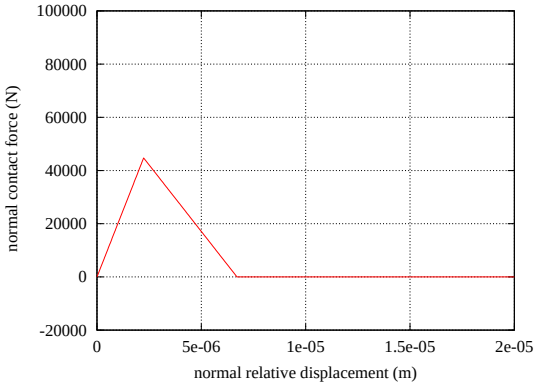

Figure 4.18: Tangential contact force vs. tangential relative displacement under shear combined with tension (elasto-plastic contact model with linear softening)

(Fig. 4.17) is twice as large as final relative normal displacement. The force curves are typical for elasto-plastic model with linear softening. It must be noted that the peak values of the normal and tangential components are lower than the interface strengths to shear or tension, however the resultant contact force has prescribed peak value.

4.6.2 Elastic damage contact model with linear softening

Simulation of pure tension, compression and shear

Tests of pure tension, compression and shear similar as for the previous model were carried out. Loading was applied under displacement control. Variation of the normal contact force against the normal relative displacement under monotonic tensile loading is shown in Fig. 4.19. The peak force of 100 kN is achieved for relative displacement 0.005 mm, and then the yielding of the contact bond occurs until complete breakage at separation of 0.015 mm. This curve is the same as obtained for the same test for elastic-plastic model with linear softening (Fig. 4.11). Difference can be observed for the tension test with unloading and reloding, Fig. 4.20, when compared to Fig. 4.12. Now unloading and reloading occurs with secant elastic modulus. Compressive normal force under monotonic loading is shown in Fig. 4.21. Compression is treated as an elastic process similarly as in the previous model. Tangential contact force vs. tangential relative displacement under shear monotonic loading is shown in Fig. 4.22. Elastic increase of the tangential force and subsequent drop due to yielding can be observed. Since no unloading was introduced the curve in Fig. 4.22 is the same as the curve in Fig. 4.14.

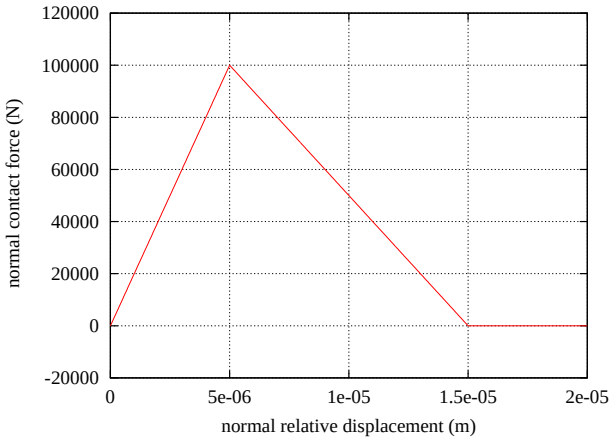

Figure 4.19: Normal contact force vs. normal relative displacement under monotonic tensile loading (elastic damage contact model with linear softening)

Simulation of combined shear with tension and compression

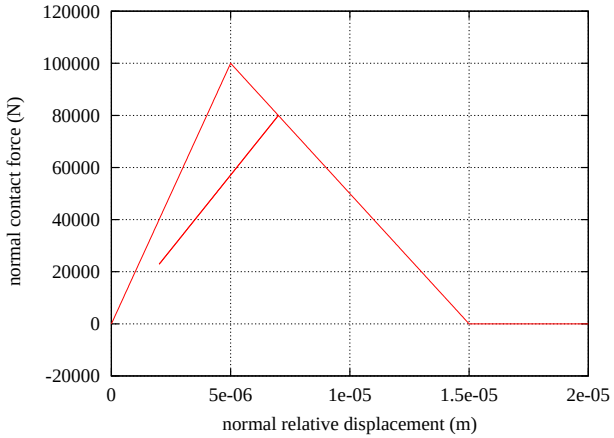

Figure 4.20: Normal contact force vs. normal relative displacement under tensile loading with unloading and reloading (elastic damage contact model with linear softening)

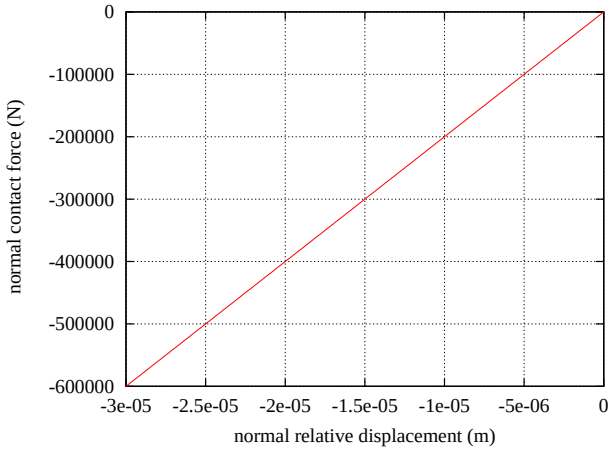

Figure 4.21: Normal contact force vs. normal relative displacement under compressive monotonic loading (elastic damage contact model with linear softening)

The interface has been subjected to combined loading. The test conditions were the same as those used in the tests of elasto-plastic model with linear softening. The linear relationship for normal compressive force is shown in Fig. 4.23. Figure 4.24 presents variation of the tangential force versus the relative tangential displacement along with increasing compressive force.

Tangential and normal contact forces versus respective relative displacements are shown in Figs. 4.25 and 4.26 for shear combined with tension. Test conditions are the same as for the elasto-plastic model with linear softening (tangential relative velocity is twice as high as normal one). It should be noted that now the peak value of the tangential component (of a higher value of the two components) is equal to the shear interface strength. The other (normal) component does not reach the maximum

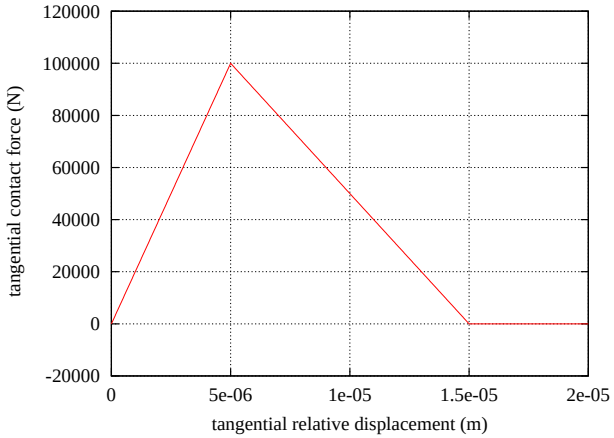

Figure 4.22: Tangential contact force vs. tangential relative displacement under shear monotonic loading (elastic damage contact model with linear softening)

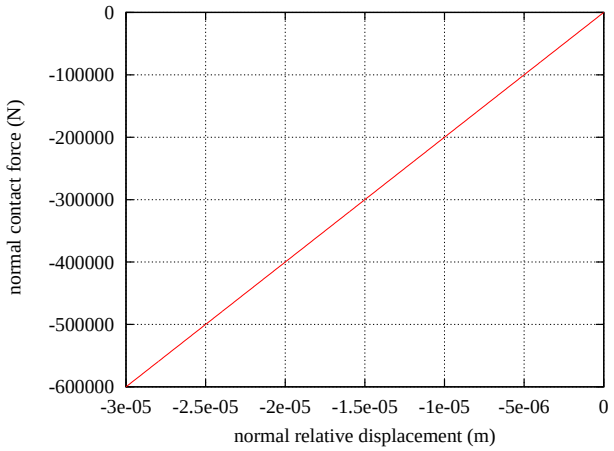

Figure 4.23: Normal contact force vs. normal relative displacement under shear combined with compression (elastic damage contact model with linear softening)

strength for pure tension because when the tangential force reaches its peak value the interface damage also affects the interface strength in the normal direction.

4.7 Summary

Other more sophisticated micromechanical models have been implemented in the program Stampack within the discrete element method formulation in order to give better possibilities to model soil and rock materials.

A generalized elastic-plastic model has been implemented with nonlinear softening as well as its simplified version with linear softening.

The micromechanical models use both elastic-plastic and damage formulation with

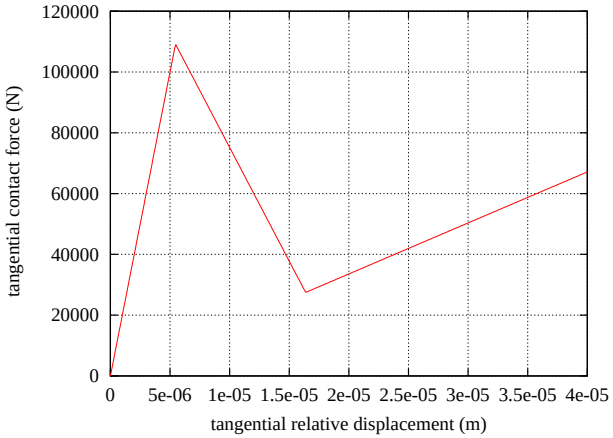

Figure 4.24: Tangential contact force vs. tangential relative displacement under shear combined with compression (elastic damage contact model with linear softening)

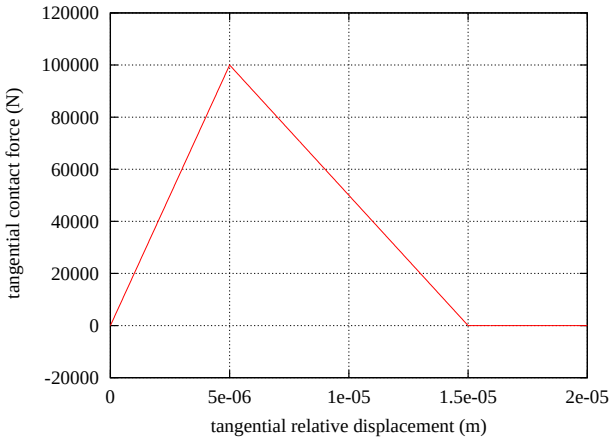

Figure 4.25: Tangential contact force vs. tangential relative displacement under shear combined with tension (elastic damage contact model with linear softening)

strain softening.

Simplified elasto-plastic model was implemented in the program as well. Simplification consist in assuming linear softening only and yielding due to tension and shear only. These assumptions are aimed to decrease the number of parameters to calibrate and at the same time allow us to represent strain-softening macroscopic behaviour of the material. On the other hand the elastic perfectly brittle material was improved by introduction of strain softening with elastic damage.

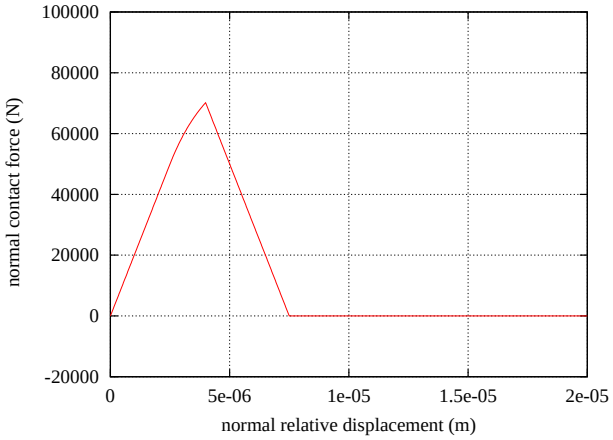

Figure 4.26: Normal contact force vs. normal relative displacement under shear combined with tension (elastic damage contact model with linear softening)

Chapter 5

Study of macroscopic material properties

Introduction

This study is aimed to find out similarities and differences in macroscopic behaviour of a material modelled with different micromechanical models and influence of micromechanical parameters on macroscopic material behaviour. Uniaxial compression test has been chosen as a test example.

5.1 Simulation of uniaxial compression test

5.1.1 Numerical model

Macroscopic response of a square material sample subjected to uniaxial compression has been studied. Figure 5.1 presents the material sample prepared for testing. Material sample 109×109 mm is represented by an assembly of randomly compacted 2100 discs of radii $1 \div 1.5$ mm.

The loading has been introduced under kinematic control by prescribing the motion of the right and left walls. The deformation in the y direction was free. The velocity of the displacement of the walls was 1 mm/s which was found to be sufficiently low to obtain quasi-static loading.

The micromechanical parameters constant in all the numerical tests are the following: contact stiffness in the normal and tangential directions $k_n = k_T = 20$ GPa and the friction coefficient $\mu = 0.839$.

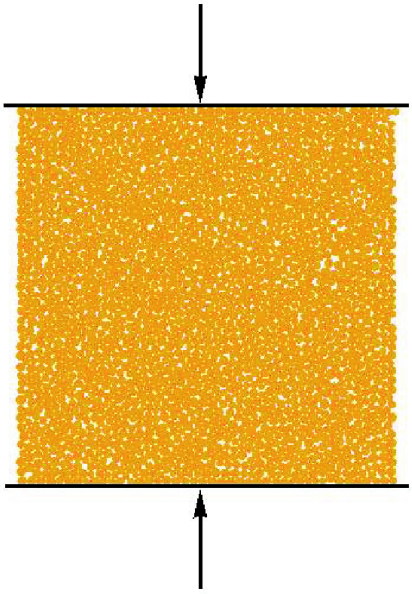

Figure 5.1: Initial geometry of a material sample

5.1.2 Numerical results

Numerical simulation of the compression test using elastic perfectly brittle micromechanical model with the cohesive bond strengths $R_n = 0.1$ MN/m $R_T = 1$ MN/m has been found out to give macroscopic behaviour corresponding to sandstone, cf. [21].

The stress-strain relationships obtained for three different micro-mechanical models yielding similar macroscopic compressive strength are shown in Fig. 5.2. The stresses were calculated by taking the sum of the contact interactions between the walls and particles. Elastic perfectly brittle model as well as the model with elastic damage with

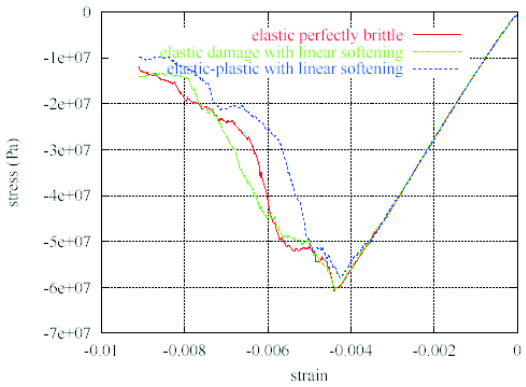

Figure 5.2: Stress-strain relationships for three different constitutive models giving similar macroscopic compressive strength

linear softening were used with the same cohesive bond strengths $R_n = 0.1$ MN/m and $R_T = 1$ MN/m. The softening in the latter model was defined by the softening modulus $H = 2 \cdot 10^{11}$ N/m. The parameters for the elastic-plastic micromechanical model were the following: cohesive bond strengths $R_n = 0.04$ MN/m and $R_T = 0.16$ MN/m, softening modulus $H = 10^{10}$ N/m. The values yielding the desired macroscopic strength were assumed here. It can be seen in Fig. 5.2 that stress-strain curves obtained with different micromechanical models are similar. It shows that similar macroscopic behaviour can be reproduced using different micromechanical models. Failure modes obtained for different micromechanical models are shown in Figs. 5.3–5.5 in the form of final deformed configurations with displacement field and distribution of broken bonds. One can see localization zones and discontinuities of the displacement fields.

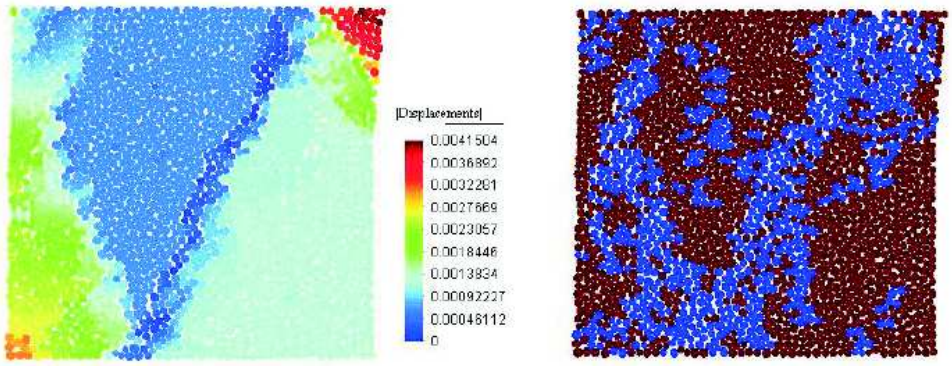

a) b)

Figure 5.3: Failure mode obtained for the elastic perfectly brittle model, a) displacement distribution, b) broken bonds

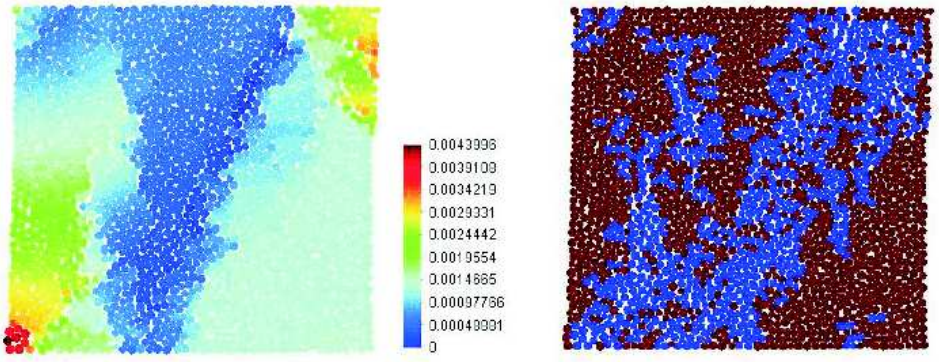

a) b)

Figure 5.4: Failure mode obtained for the elastic damage model with linear softening (softening modulus $H = 2 \cdot 10^{11}$ N/m), a) displacement distribution, b) broken bonds

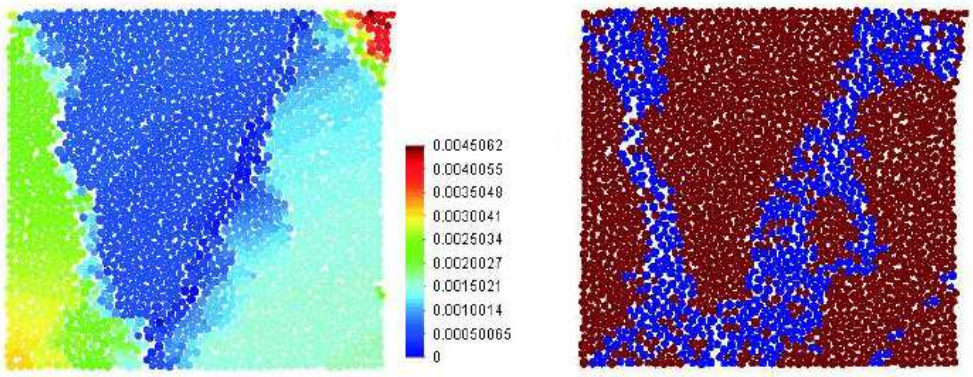

a) b)

Figure 5.5: Failure mode obtained for the elastic plastic model with linear softening (softening modulus $H = 10^{10}$ N/m), a) displacement distribution, b) broken bonds

Comparison of Figs. 5.3-5.5 indicates that the failure modes obtained with the three models analysed are similar, strain localisation and fracture occurs along the same lines although some differences can be noted between elastic plastic model (Fig. 5.5) and the other two models (Figs. 5.3 and 5.4), broken bonds obtained with elastic-plastic model are localized in smaller zones along fracture lines.

Elastic damage with different softening moduli

A number of analyses have been carried out using different softening moduli. Influence of softening value on macroscopic behaviour has been studied. Stress-strain relationships for micromechanical model with elastic damage using different softening moduli are shown in Fig. 5.6. It can be seen that in a certain range of values of softening modulus the stress-strain curve does not change much, the compressive strength and

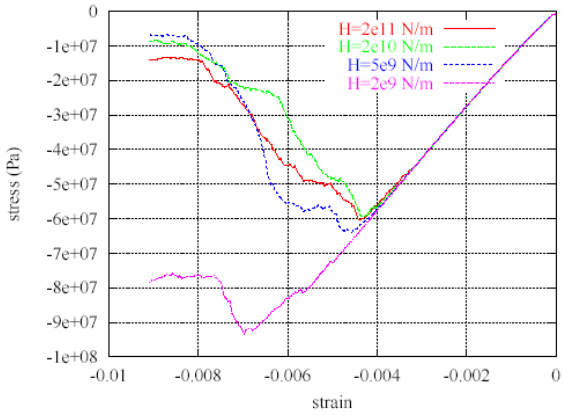

Figure 5.6: Stress-strain relationships for elastic damage micromechanical model with different softening moduli

curves in post-critical deformation are similar for softening moduli of $2 \cdot 10^{11}$, $2 \cdot 10^{10}$ and $5 \cdot 10^{9}$ N/m. Significant difference can be observed for the lowest softening modulus only. This difference can be understood by analysing the failure modes presented in Figs. 5.4 and 5.7–5.9. While the failure mode obtained for softening moduli of $2 \cdot 10^{11}$, $2 \cdot 10^{10}$ and $5 \cdot 10^{9}$ N/m (Figs. 5.4, 5.7 and 5.8) are similar one to another, in case of the softening modulus $2 \cdot 10^{9}$ N/m (Fig. 5.9) different localisation zones can be observed.

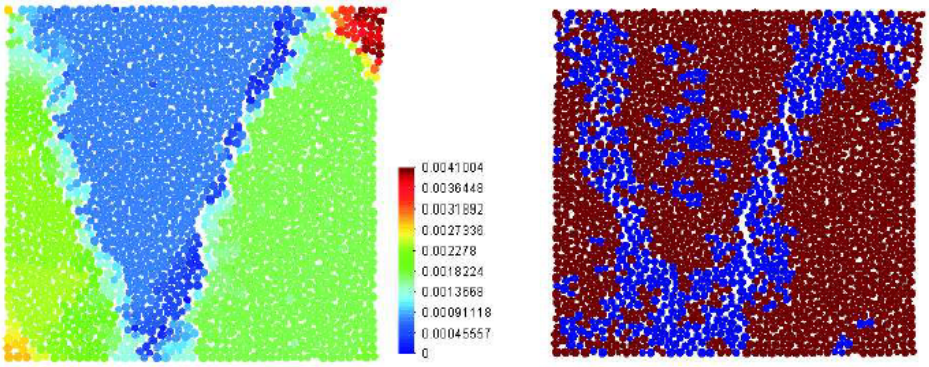

a) b)

Figure 5.7: Failure mode obtained for the elastic damage model with linear softening (softening modulus $H = 2 \cdot 10^{10}$ N/m), a) displacement distribution, b) broken bonds

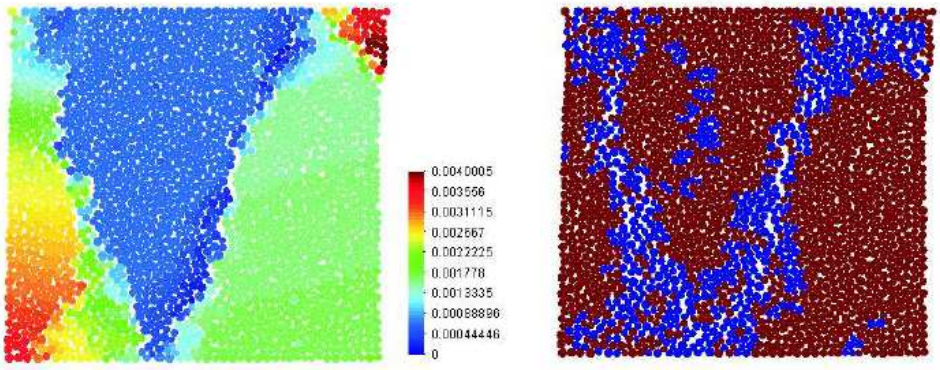

a) b)

Figure 5.8: Failure mode obtained for the elastic damage model with linear softening (softening modulus $H = 5 \cdot 10^{9}$ N/m), a) displacement distribution, b) broken bonds

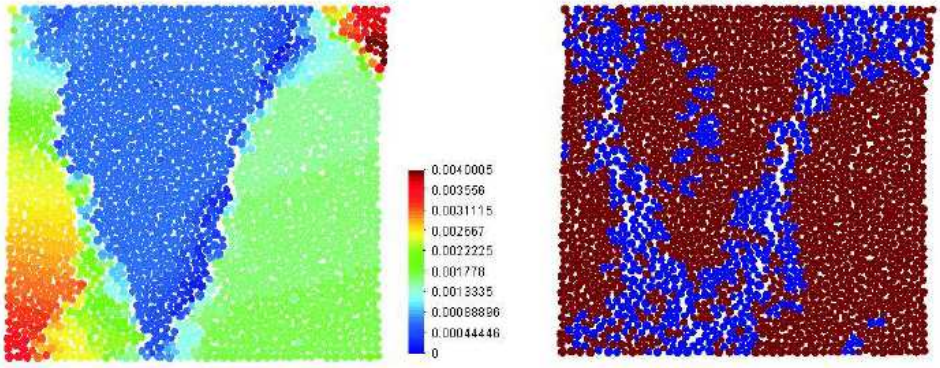

a) b)

Figure 5.9: Failure mode obtained for the elastic damage model with linear softening (softening modulus $H = 2 \cdot 10^9$ N/m), a) displacement distribution, b) broken bonds

Elastic plastic model with different softening moduli

A number of analyses have been carried out using elastic plastic model with different softening moduli. Influence of softening value on macroscopic behaviour has been studied. Stress-strain relationships for different softening moduli are shown in Fig. 5.10.

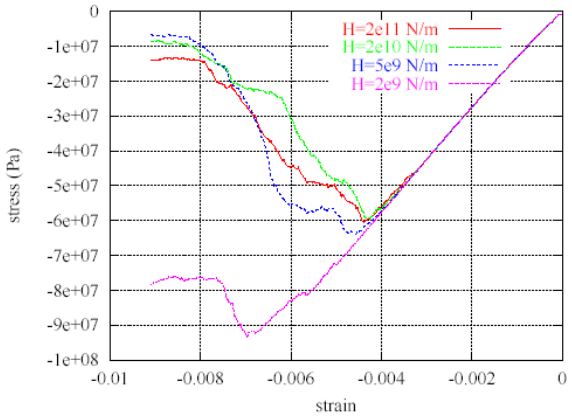

Figure 5.10: Stress-strain relationships for elastic-plastic micromechanical model with different softening moduli

It can be seen that in this case the solution is very sensitive to softening value. Although the failure modes (Figs. 5.5, 5.11–5.13) are similar, macroscopic compressive strength increases significantly with the increase of softening modulus. In this model softening is very important parameter influencing the macroscopic strength.

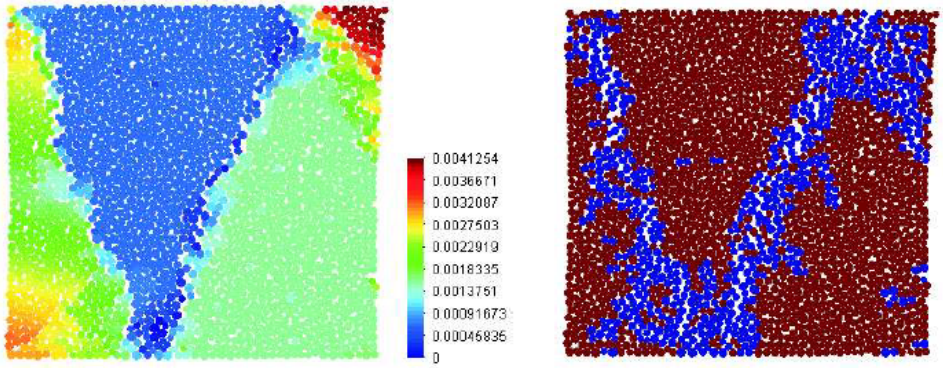

a) b)

Figure 5.11: Failure mode obtained for the elastic-plastic model with linear softening (softening modulus $H = 2 \cdot 10^{10}$ N/m), a) displacement distribution, b) broken bonds

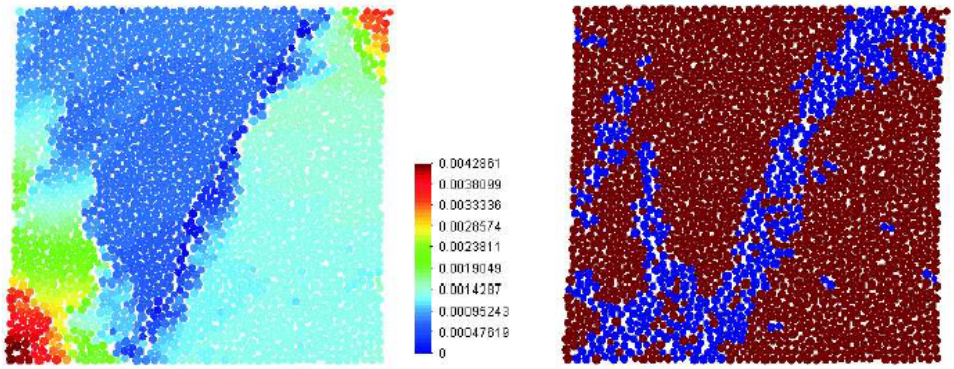

a) b)

Figure 5.12: Failure mode obtained for the elastic-plastic model with linear softening (softening modulus $H = 5 \cdot 10^9$ N/m), a) displacement distribution, b) broken bonds

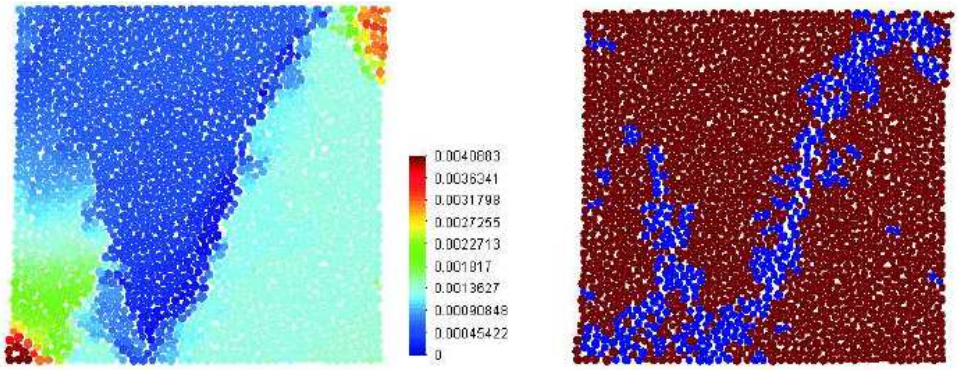

a) b)

Figure 5.13: Failure mode obtained for the elastic-plastic model with linear softening (softening modulus $H = 2 \cdot 10^9$ N/m), a) displacement distribution, b) broken bonds

Conclusions

Numerical studies carried out with different micromechanical models show that similar macroscopic behaviour can be reproduced using different micromechanical models. Failure modes obtained using these models are quite similar. Strain localisation occurs in the same zones. Macroscopic properties were compared using stress-strain curves. Influence of strain softening on macroscopic material behaviour has been studied. It has been found out that elastic-plastic model is more sensitive to changes of strain softening.

Chapter 6

Wear evaluation

In this section numerical model is extended on the problems of wear evaluation. Main factors influencing wear are identified. Temperature must be taken into account in wear evaluation, therefore thermal effects have been included in the numerical algorithm of wear of rock cutting. Discrete element model was extended into analysis of transient heat flow. Thermal analysis can be carried out along with the solution of mechanical problem. Thermal equations are coupled with equations of motion yielding a set of equations describing thermomechanical problem.

6.1 Basic concepts of wear

Wear is the process of progressive loss of material from the surface of a solid body due to mechanical action, i.e. the contact and relative motion against a solid, liquid or gaseous counterbody. There are different wear mechanisms. These mechanisms can be classified into the following four basic groups, cf. [22]:

- adhesive wear,
- abrasion,
- surface fatigue,
- tribochemical reaction.

Adhesive wear is the process of wear accompanied by formation and breaking of interfacial adhesive bonds. Adhesive wear can occur when two surfaces slide along each other (Fig. 6.1a). High local pressure between contacting asperities results in plastic deformation, adhesion and formation of local junctions. Breaking of these junctions due to shear leads to wear. Abrasion is the process of wear characterised with removal or displacement of material at a solid surface due to presence of hard particles in between or embedded in one or both of two solid surfaces in relative sliding motion. If

two surfaces are involved (Fig. 6.1a), or one surface against particles (Fig. 6.1b,c), the process is called two-body abrasive wear. If particles are present between two surfaces (Fig. 6.1d), the abrasive mechanism is called three-body abrasive wear.

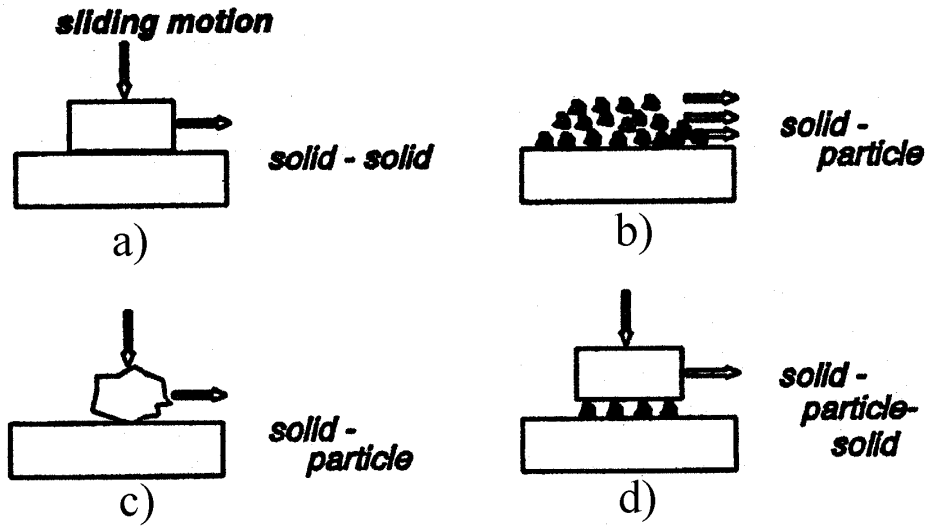

Figure 6.1: Tribological wear systems: a, b, c) two-body systems, d) three-body system

Surface fatigue is a wear mechanism occurring due repeated dynamic loading of a surface, which can lead to crack formation. Tribochemical reaction is a wear process caused by corrosive reactions of two rubbing surfaces with environmental medium. In most cases of real wear processes combined action of different wear mechanisms occurs. Wear processes are very complex and depend on many system properties and process parameters including:

- loads and velocities and their change in time
- ambient and interfacial temperature
- characteristics of solid and counterbody such as
  - their geometry
  - interfacial friction coefficients
  - material properties (strength, hardness, thermal conductivity and temperature dependency of these parameters).

6.2 Wear of rock cutting tools

In our case the wear of the steel cutting tool is under study. In the tribological system considered the cutting tool is a solid body, which undergoes wear and the cut rock

forms a solid counterbody. Rock debris present in between the tool and intact rock can constitute a third body. In such a tribological system different wear mechanism can operate. When the cutter teeth cut a rock, impacting and sliding motion occur. Impact loading can lead to surface fatigue, while sliding motion can lead to adhesive or abrasive wear. Abrasive wear is especially high when the abrasive (rock) is harder than the tool material (Fig. 6.2). The tool surface can be softened by high temperatures developed on the surface due to heat generated by friction between tool and rock. In some cases temperature on the tool surface can reach as much as 550–800°C, cf. [23]. Thermal softening of the tool material caused by high temperature increases wear.

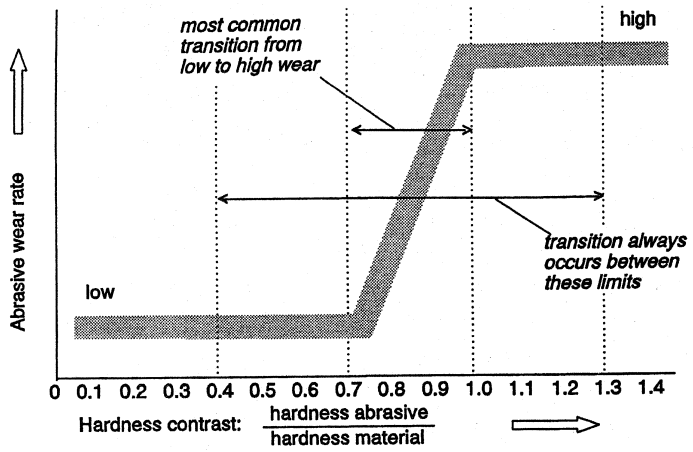

Figure 6.2: Amount of abrasive wear in function of the ratio of the abrasive hardness to the tool material hardness (according to [23])

The following factors have been identified as the most important ones influencing wear of rock cutting tools, cf. [23]:

1. Rock/soil properties
    - mechanical properties (strength, hardness, fracture properties)
    - thermal properties (heat capacity, thermal conductivity)
    - texture, discontinuities existing in the rock
    - particle size/shape
    - abrasive capacity of rock or soil
2. Tool characteristics
    - mechanical properties of the tool material (temperature dependent strength, hardness)

- thermal properties (heat capacity, thermal conductivity)
- geometry of the tool

3. Cutting process parameters

   - position of a tool with respect to rock (penetration depth, rake and cutting angles)
   - relative sliding velocity
   - normal pressure on the tool surface
   - heat generation/convection, temperature

6.3 Modelling of wear

Among the quantitative laws of wear the classical law of Archard [24] is still widely used. It assumes that the wear rate $\dot{w}$ is proportional to the contact pressure p_n and to the slip velocity v_T

$$\dot{w} = k\frac{p_n v_T}{H} \tag{6.1}$$

where H denotes the hardness of worn surface and k is a dimensionless parameter. The Archard law was derived originally for adhesive wear, the same form of law, however, can be obtained for abrasive wear, cf. [25]. Values of adhesive and abrasive wear constants k for different combinations of materials can be found in [25]. It is commonly accepted that wear is related to friction and thus friction coefficients are often introduced into Eq. (6.1). If Coulomb friction holds

$$p_T = \mu p_n \tag{6.2}$$

μ being the friction coefficient, the Archard wear law can be written in the following equivalent form:

$$\dot{w} = \bar{k}\frac{p_T v_T}{H} = \bar{k}\frac{\dot{D}}{H} \tag{6.3}$$

in which the wear rate is related to frictional dissipation rate $\dot{D}$ and $\bar{k} = k/\mu$. Stupkiewicz and Mróz [26] generalised the Archard law combining in one equation different wear modes

$$\dot{w} = \frac{1}{H}\sum_i \bar{k}_i \dot{D}_i = \frac{1}{H}\sum_i \bar{k}_i p_{Ti} v_T \tag{6.4}$$

where $\dot{D}_i = p_{Ti} v_T$ is the dissipation rate associated with the specific mode. This law must be associated with an appropriate friction model allowing us to decompose the

total frictional dissipation. A more general rule can be formulated by assuming non-linear relations between wear rates and the dissipation rates of particular modes (see also [25])

$$\dot{w} = v_T \sum_i \left(\frac{p_{Ti}}{\tau_i} \right)^{n_i} = v_T \sum_i \left(\frac{p_{Ti}}{\bar{\tau}_i H} \right)^{n_i} \tag{6.5}$$

where n_i are dimensionless exponents and τ_i are the reference shear stresses for respective wear modes, it can be related to the hardness of the worn surface H.

6.4 Wear model with thermal effects included

High temperatures developed on the surface (in some cases temperature on the tool surface can reach as much as 550–800°C, cf. [23] due to heat generated by friction between tool and rock reduce the hardness of the surface and increase adhesive and abrasive wear.

Influence of temperature on wear can be taken into account by adaptation of the law of Archard [24] given by Eq. (6.1). Thermal effects can be captured approximately by taking hardness H changing with temperature T

$$H = H(T) \tag{6.6}$$

$$\dot{w} = k \frac{p_n v_T}{H(T)} \tag{6.7}$$

Friction forces will be evaluated assuming the Coulomb law:

$$p_T = \mu p_n \tag{6.8}$$

where μ is the friction coefficient. Substituting relationship (6.8) into (6.7) we obtain the following temperature dependent law to evaluate the wear:

$$\dot{w} = \bar{k} \frac{p_T v_T}{H(T)} = \bar{k} \frac{\dot{D}}{H(T)} \tag{6.9}$$

where $\dot{D}$ is the frictional dissipation rate and $\bar{k} = k/\mu$.

6.5 Numerical implementation of wear evaluation algorithm

The tool wear w, i.e. the amount (depth) of removed material is obtained by integrating the wear rate $\dot{w}$ in time

$$w = \int \dot{w} \, \mathrm{d}t \, . \tag{6.10}$$

The Archard law given by Eq. (6.9) has been implemented in the numerical algorithm. Distribution of the wear for one cycle can be estimated.

Wear is a relatively slow process and it can be observed after many work cycles. In the numerical algorithm developed wear is accelerated using scaled wear constants. Thus visible wear is obtained in one cycle analysed.

The developed numerical algorithm of wear evaluation takes advantage of the tool discretization with distinct elements. This will allow us to easily modify the shape of the tool. The tool shape is changed eliminating particles if the accumulated wear exceeds the particle diameter. Particles are eliminated automatically and the analysis is continued with modified shape of the tool. Elimination of the particles was easy to implement thanks to the structure of linked list adopted for database of distinct elements. Numerical examples included in this report present the possibilities of the numerical analysis with calculation of wear.

Evolution of the tool shape is obtained in a number of consecutive simulations of work cycles. The tool shape is modified continuously during the analysis. After finishing one work cycle the tool with a new shape is again used in the simulation of another work cycle. The whole procedure can be repeated a certain number of times. This will allow us to obtain the evolution of change of tool shape in wear process during its whole service life.

Thermal effects are taken into account in the wear model algorithm. Heat generated in cutting process due to friction dissipation is calculated in the solution of mechanical problem and passed to the thermal analysis. In the simulation of thermal problem heat conduction through the tool and rock is analysed giving the temperature distribution in the tool. Temperature on the tool surface lowers its hardness and increases its wear. This is considered by assuming temperature dependent tool hardness in the equations used to evaluate the tool wear.

In order not to introduce additional irregularities into the tool geometry the particles discretising a tool are considerably smaller than the particles of material.

To achieve better computational efficiency (by reducing the number of nodal points) a part of the tool, which does not undergo wear, can be represented by rigid triangular facets. This kind of geometric representation can be used for the whole tool if the shape of the tool will not be modified.

Assumption of rigidity of the tool introduces rigid constraints on all the particles used in the discretisation of the tool. Since there is no relative displacement, there is no necessity to perform contact search among the particles discretising the tool. The contact analysis will be carried out to find the interaction between the set of particles discretising the tool and the set of particles modelling rock specimen.

6.6 Estimation of wear constants from laboratory tests

Evaluation of wear using Eqs. (6.1) or (6.7) requires the knowledge of material constants k and $H(T)$ or their ratio $k/H(T)$. These values are specific for the pair of materials. The value of wear coefficient k depends on many factors. There is no straight relationship between these factors and k so the only possibility is to obtain this value experimentally. Our numerical studies will be based on the values of these constants calculated using the results of laboratory wear tests carried out in ZFS. Here we present calculations for selected tests.

From Eq. (6.7) we obtain the formula to calculate wear coefficient k:

$$k = \frac{\dot{w}}{p_n v_T} H(T) \tag{6.11}$$

Hardness was introduced into the formula (6.1) by assumption of the straight proportionality between hardness and yield stress, cf. [24, 25]. Actually different scales of hardness measure can be used. The choice of a given hardness measure only affects the value of k. Hardness measure in pressure units, for instance the Brinell hardness, gives dimensionless coefficient of wear k.

Temperature dependent Brinell hardness $H = H(T)$ has been obtained in laboratory tests carried out by Metalogenia for materials used in the production. Details of these tests and the results are given elsewhere. The results for steels MET 71 and MET 91 are given in Table 6.1. Numerical algorithm employs piecewise linear interpolation of hardness in function of temperature. From Table 6.1 we can see that tested steels soften considerably in temperatures higher than 300°C.

Table 6.1: Brinell hardness at different temperatures

Temperature	0°C	200°C	300°C	400°C	500°C	600°C
MET 71	500	491	480	439	362	241
MET 91	515	509	498	457	375	247

The other data necessary to calculate wear coefficient k using Eq. (6.11) are taken from the laboratory wear tests carried out in ZFS. The test set-up of these tests is shown in Fig. 6.3. More details of the tests are given in another document.

Results of the laboratory wear tests for steels MET 71 and MET 91 carried out in ZFS are given in Tables 6.2 and 6.3.

Using the values from Table 6.2 and taking the hardness for the given temperature we can calculate wear coefficient k using the formula (6.11) in the following way.

$$k = \frac{\dot{w}}{p_n v_T} H(T) = \frac{\Delta w}{p_n \Delta s} H(T) = \frac{1.6 \cdot 10^{-3}}{34 \cdot 10^6 \cdot 100} \cdot 493 \cdot 10^6 \cdot 10 = 0.0023 \tag{6.12}$$

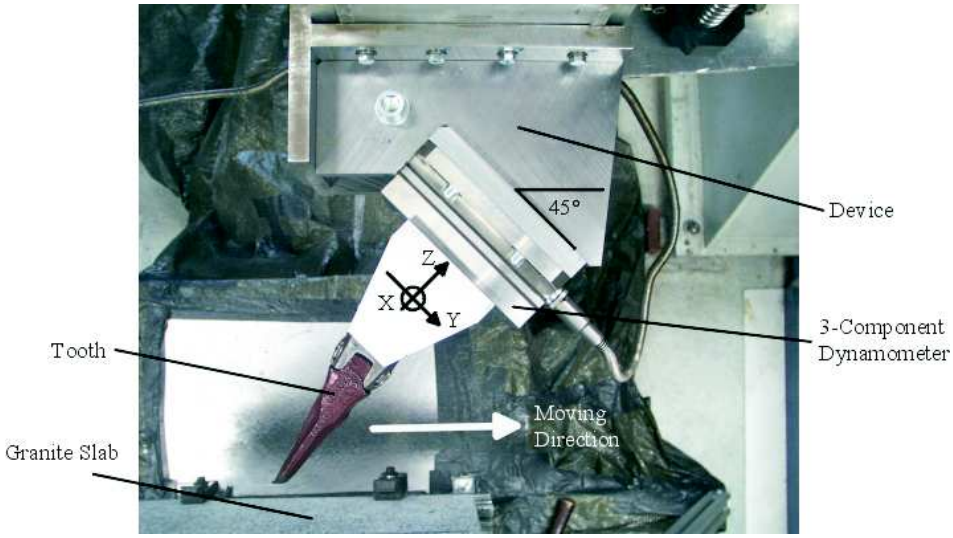

Figure 6.3: Set-up of the laboratory wear tests

Table 6.2: Results of the laboratory wear tests for steels MET 71

distance (m)	100	200
cutting velocity (m/s)	0.117	0.117
normal force (N)	885	840
contact surface (mm^2)	26	30
contact pessure (MPa)	34	28.2
wear depth (mm)	0.4	2
temperature (°C)	156	146

Table 6.3: Results of the laboratory wear tests for steels MET 91

distance (m)	100	200
cutting velocity (m/s)	0.117	0.117
normal force (N)	622	1237
contact surface (mm^2)	68	138
contact pessure (MPa)	9.1	9.0
wear depth (mm)	4	6
temperature (°C)	128	213

or

$$k = \frac{\Delta w}{p_n \Delta s} H(T) = \frac{1.6 \cdot 10^{-3}}{28.2 \cdot 10^6 \cdot 100} \cdot 494 \cdot 10^6 \cdot 10 = 0.0028 \qquad (6.13)$$

An average value of wear coefficient $k = 0.0025$ and hardness given in Table 6.1 define the wear of steel MET 71 calculated from the Archard extended formula 6.7 and will be used in numerical simulations presented later.

Using the data for steel MET 91 from Tables 6.3 and 6.1 we can calculate wear coefficient k in a similar way as above

$$k = \frac{\Delta w}{p_n \Delta s} H(T) = \frac{2 \cdot 10^{-3}}{9.1 \cdot 10^6 \cdot 100} \cdot 512 \cdot 10^6 \cdot 10 = 0.0113 \tag{6.14}$$

or

$$k = \frac{\Delta w}{p_n \Delta s} H(T) = \frac{2 \cdot 10^{-3}}{9.0 \cdot 10^6 \cdot 100} \cdot 509 \cdot 10^6 \cdot 10 = 0.01125 \tag{6.15}$$

Chapter 7

Discrete Element formulation for thermal and thermo-mechanical problem

7.1 Heat balance equation

Evaluation of wear requires determination of forces of cutting as well as temperature distribution. This means necessity to analyse rock cutting as a thermo-mechanical process. Temperature increases due to heat generated by friction between tool and rock. Heat is adsorbed and conducted by the tool and rock. These processes depend on thermal properties (heat capacity, thermal conductivity) of the tool and rock.

Thermal phenomena during rock cutting are described by the heat balance equation. This equation can be written for a single particle in the following form:

$$m_i c \dot{T}_i = Q_i \,, \tag{7.1}$$

where the following notation has been used:

c – solid heat capacity,

T_i – particle temperature;

Q_i – heat sources or heat fluxes per single particle.

Q_i includes externally supplied heat source Q_{ext}, heat generated through friction dissipation and adsorbed by the particle Q_{gen}, heat conducted through the contact interface with another material Q_{contact}, heat conducted to particles of the same material Q_{cond} and convective and radiative heat transfer between particles and environment on the free surface, $Q_{\text{convection}}$ and $Q_{\text{radiation}}$

$$Q_i = (Q_{\text{ext}} + Q_{\text{gen}})_i - (Q_{\text{cond}} + Q_{\text{contact}} + Q_{\text{convection}} + Q_{\text{radiation}})_i \tag{7.2}$$

It should be remembered that Q_{cond} contains contributions from all the neighbouring particles which are in contact with the i-th particle, similarly Q_{gen} gathers contributions from all the neighbouring particles in contact with the i-th particle. The term Q_{contact} is included for the particles on the contact interface, and terms $Q_{\text{convection}}$ and $Q_{\text{radiation}}$ are evaluated for the particles on the free surface.

Particle-to-particle conductive heat transfer rate Q_{cond} is estimated as the transfer through an equivalent bar element of length d equal to the distance between the particle centres and of certain equivalent area $\bar{A}$ (function of particle radii)

$$Q_{\text{cond}} = h_{\text{cond}}(T_i - T_j) = \kappa \frac{\bar{A}}{d}(T_i - T_j) \tag{7.3}$$

with h_{cond} being the heat transfer coefficient between material particles, κ being the solid heat conductivity, and T_i and T_j being contacting particles temperatures.

7.2 Thermal boundary conditions

Thermal boundary conditions can be specified for temperatures T or for heat fluxes/sources Q. Thus the boundary Γ can be split into two disjoint parts, one with prescribed temperature Γ_T and the other with prescribed heat flux Γ_Q

$$\Gamma = \Gamma_T \cup \Gamma_Q \tag{7.4}$$

$$\Gamma_T \cap \Gamma_Q = \emptyset \tag{7.5}$$

Heat fluxes can be specified in different ways:

1. Point heat flux (representing either heat source or sink). It is represented in Eq. (7.2) by the term Q_{ext}. A special case of the prescribed heat flux is the case of insulation – with all external fluxes set to zero

$$Q_{\text{ext}} = 0\,, \quad Q_{\text{contact}} = 0\,, \quad Q_{\text{convection}} = 0\,, \quad Q_{\text{radiation}} = 0 \tag{7.6}$$

2. Convection to the environment (on the free surface, represented by the term $Q_{\text{convection}}$)

3. Radiation to the environment (on the free surface, represented by the term $Q_{\text{radiation}}$)

4. Heat transfer between contacting bodies (at the contact interface, represented by the term Q_{contact}).

Application of the thermal boundary conditions for the free surface and contact interface requires detection of these parts of boundary in the discrete element model. The boundary itself in the model of particles changes when fractures appear in the material

and some particle become new surface particles. In the model of free particles (without cohesive bonds) the motion of the particles leads to change of the free boundary. In the wear analysis is carried out modification of the tool shape also leads to change of free surface. These features of the particle model make it necessary to update free surface definition, which can only be effective by employing an automatic procedure. Parts of the boundaries in contact with another body must also be detected, this however does not mean additional effort, since the detection of the contact interface is done in the solution of the mechanical problem. It is assumed that a given particle can be either on the contact interface or on the free surface. Therefore for particles with detected contact excluded from the free surface.

Heat generation through frictional dissipation is calculated using the following formula

$$Q_{gen} = \chi \left| F_{fric}\, v_{rT} \right| , \tag{7.7}$$

where F_{fric} is the friction force, v_{rT} is the relative tangential velocity, and χ is the part of the friction work converted to heat.

7.3 Solution of thermo-mechanical problem

The thermo-mechanical problem is solved by coupling the heat balance equation (7.1) with equations of motion (3.1) and (3.2).

Equations (3.1), (3.2) and (7.1) describing a thermo-mechanical problem are integrated in time using a staggered scheme – solution at the n-th time step can be summarised as follows:

(i) equations of motion (3.1) and (3.2) are integrated in time using a central difference scheme given by Eqs. (3.3)–(3.10); in the solution of mechanical problem frictional dissipation and heat generation is calculated according to Eq. (7.7); wear is estimated using the material hardness at a given temperature

(ii) heat balance equation (7.1) is integrated in time using the explicit forward Euler scheme

$$T_i^{n+1} = T_i^{n+1} + \frac{\Delta t}{m_i c} Q_i^n , \tag{7.8}$$

Thermal problem is solved at the fixed updated geometrical configuration and the heat rate generation through frictional dissipation being supplied by the solution of the mechanical problem. Heat generation through frictional dissipation is assumed to be absorbed equally by the two particles in contact. Q_{gen} gathers contributions from all the neighbouring particles in contact with the i-th particle. The particle temperatures obtained in the thermal step solution are in turn passed to the mechanical problem modifying material properties.

Explicit integration in time used in the solution of mechanical and thermal equations yields high computational efficiency. This solution scheme has been implemented in the in-house explicit dynamic code Simpact [27].

7.4 Material thermal properties

Materials considered in the model of rock cutting are steel and rock/soil. Thermomechanical analysis of rock cutting process requires knowledge of the following thermal properties of the materials such as their heat capacity and heat conductivity as well as heat transfer coefficients for the contact between rock and tool and for the convection at free surface of the tool and rock. The following thermal properties have been assumed from the literature:

- steel
  - heat capacity $c = 450$ J/(kg·K),
  - heat conductivity $\kappa = 60$ W/(m·K), (low carbon steel 66.9 W/(m·K)
  - density $\rho = 7830$ kg/m^3
  - (specific heat $c = 0.12$ cal/(g·K)= 0.12·4.1868·1000 W/(m·K) = 502 W/(m·K)
- sandstone
  - heat capacity $c = 1970$ J/(kg·K),
  - heat conductivity $\kappa = 0.0125$ cal/(s·cm·K) $= 0.0125 \cdot 4.1868 \cdot 100$ W/(m·K)= 5.2 W/(m·K)
  - density $\rho = 2500$ kg/m^3
- sandy soil
  - heat capacity c = 1004 J/(kg·K),
  - heat conductivity $\kappa = 0.58$ W/(m·K),
  - density $\rho = 1820$ kg/m^3
- marble
  - heat capacity c = 860 J/(kg·K),
  - heat conductivity $\kappa = 3$ W/(m·K),
  - density $\rho = 2700$ kg/m^3

- tuff
  - heat capacity $c = 950$ J/(kg·K),
  - heat conductivity $\kappa = 0.5 \div 2.5$ W/(m·K) ($\kappa = 2$ W/(m·K)
  - density $\rho = 2500$ kg/m^3
- sand (dry)
  - heat capacity $c = 800$ J/(kg·K),
  - heat conductivity $\kappa = 0.35$ W/(m·K),
  - density $\rho = 1600$ kg/m^3

1cal = 4.1868 J

7.5 Parameters characterizing heat transfer on the surface

Heat to be removed from the surface or the heat to be absorbed by the surface is a function of the temperature difference between the surface and surrounding media and heat transfer coefficient dependent on surrounding media (air, water) and heat transfer process (convection, radiation):

- Radiation

  The heat transfer coefficient depending on radiation is assumed to be about 60 W/(m^{2}K) for a metal surface temperature of 1000 °C. In our applications temperature is usually lower. We will consider radiation jointly with convection.

- Convection

  Typical values of the heat transfer coefficient for convection with air or gas are typically $h = 10 \div 100$ W/(m^{2}K). The heat transfer coefficient depending on natural convection is of the magnitude of 30 W/(m^{2}K). Forced air-cooling may increase the convection to ≈ 100 W/(m^{2}K).

- Water cooling

  In dredging we will have heat transfer from the tooth surface to surrounding water. Depending on the flow and pressure of water, it is possible to reach values between 5000 and 50000 W/(m^{2}K). Normal values for the water cooling are $5000 \div 25000$ W/(m^{2}K). Values above 25000 W/(m^{2}K) are reached in special cooling equipment.

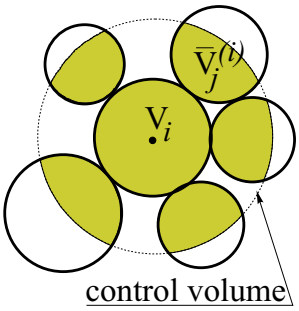

Figure 7.1: Definition of the control volume for density evaluation

Density evaluation

To evaluate the density map using the discrete element method an algorithm has been developed. For each particle a control volume is defined as it is shown in Fig. 7.1. Then an average density is defined according to the following expressions:

$$\bar{\rho}^{(i)} = \rho \frac{V_c - V_0^{(i)}}{V_c}\,, \quad V_0^{(i)} = V_c - V_i - \sum_j \bar{V}_j^{(i)}\,. \tag{7.9}$$

In the computation of the average density associated to a particle, the intersection of the control volume with the volumes of interacting particles must be computed. An exact analytical expression is used to compute these volumes.

7.6 Benchmarks of thermal analysis using DEM

Benchmarks chosen to test thermal DEM formulation are test examples for finite element thermal analysis program DOT [28].

7.6.1 Internal heat generation in parallel-sided slab

An 8-inch thick slab, infinite in extent, is initially at 0°F. Starting at time $t = 0$ heat is generated internally in the slab at a uniformly distributed rate $\dot{q} = 2000$ BTU/(sec·in^3). The external surfaces of the slab are maintained at 0°F for all time. The material properties are as follows:

- specific heat $c = 1$ BTU· in/(sec^{2}lb·°F),
- heat conductivity $\kappa = 16$ BTU/(sec· m·°F),
- mass density $\rho = 1$ sec^{2}lb/in^4

The finite element model used taking advantage of the plane symmetry is shown in Fig. 7.2. Comparison between FEM and DEM solutions is shown in Fig. 7.3 for the

temperature distributions. A very good agreement is shown. The DEM model with temperature distributions for different time instants is shown in Fig. 7.4.

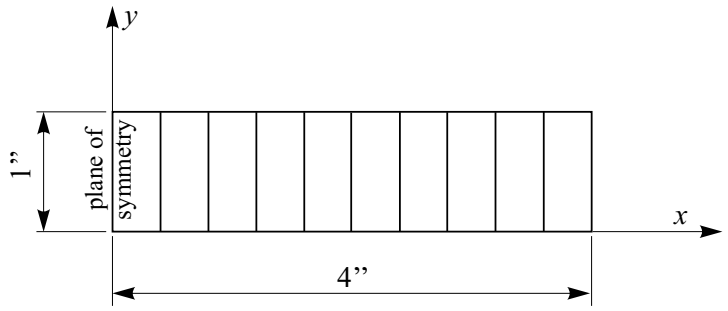

Figure 7.2: Internal heat generation in parallel-sided slab - finite element model

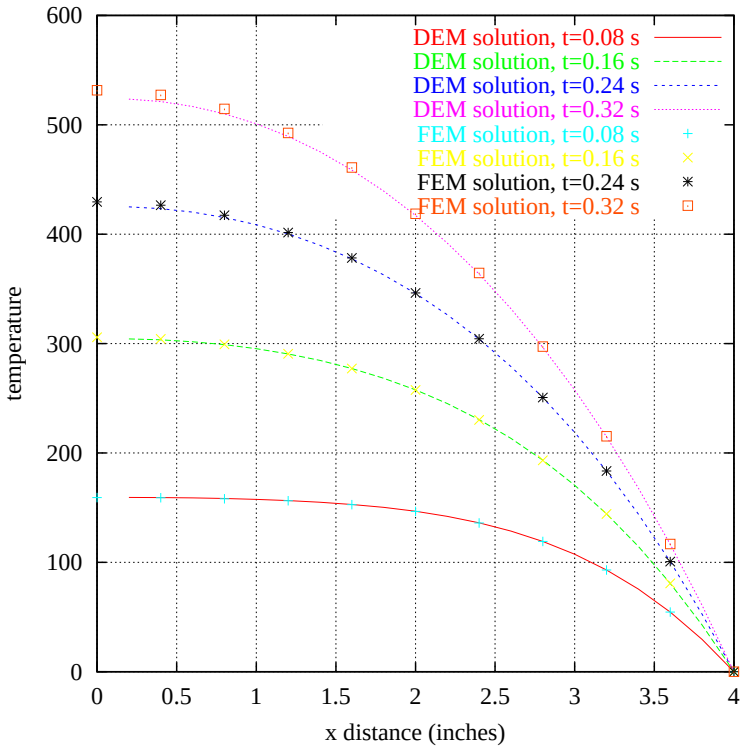

Figure 7.3: Internal heat generation in parallel-sided slab – temperature distribution – comparison of FEM and DEM results

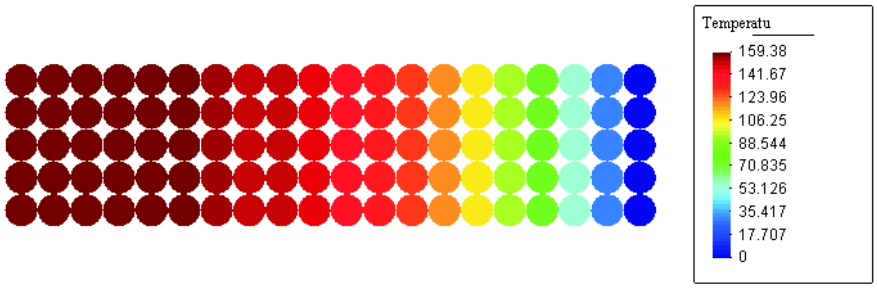

a) t = 0.08 s

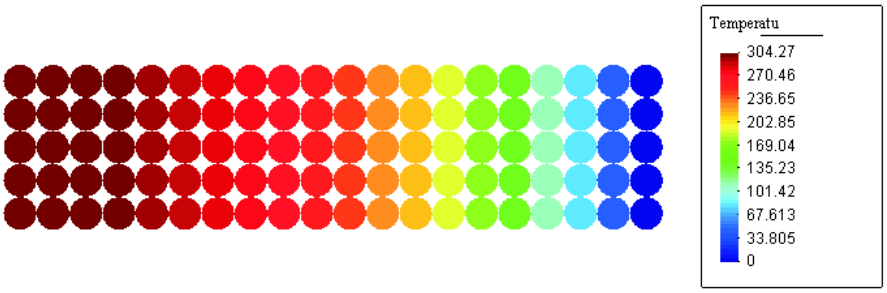

b) t = 0.16 s

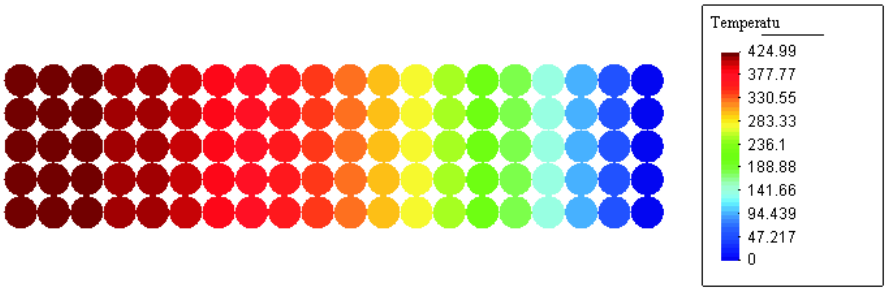

c) t = 0.24 s

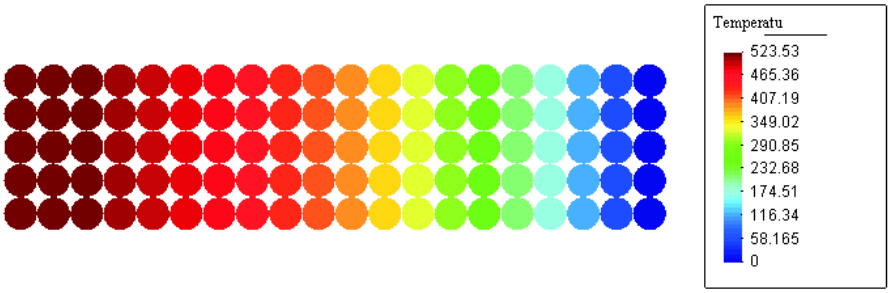

d) t = 0.32 s

Figure 7.4: Internal heat generation in parallel-sided slab - temperature distribution at different time instants (discrete element method results)

7.6.2 Semi-infinite solid subjected to a unit surface heat flux

A semi-infinite solid initially at zero temperature is exposed to a constant surface heat flux of unit intensity. The material properties are assigned unit values:

- specific heat $c = 1$ BTU$\cdot$ in/(sec^{2}lb$\cdot^\circ$F),
- heat conductivity $\kappa = 1$ BTU/(sec$\cdot$ m$\cdot^\circ$F),
- mass density $\rho = 1$ sec^{2}lb/in^4

The finite element model used in the calculations is shown in Fig. 7.5. Comparison between FEM and DEM solutions is shown in Fig. 7.6 for the temperature distributions. Again a very good agreement is found out. The DEM model with temperature distributions for different time instants is shown in Fig. 7.7.

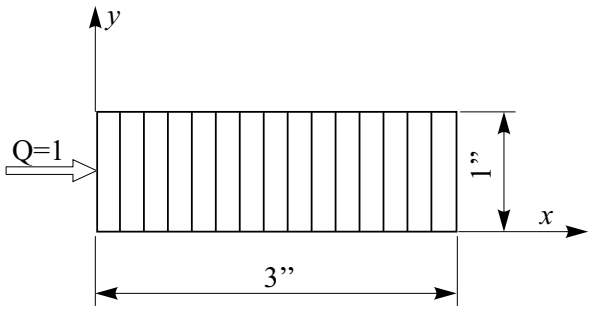

Figure 7.5: Semi-infinite solid subjected to a unit surface heat flux - finite element model

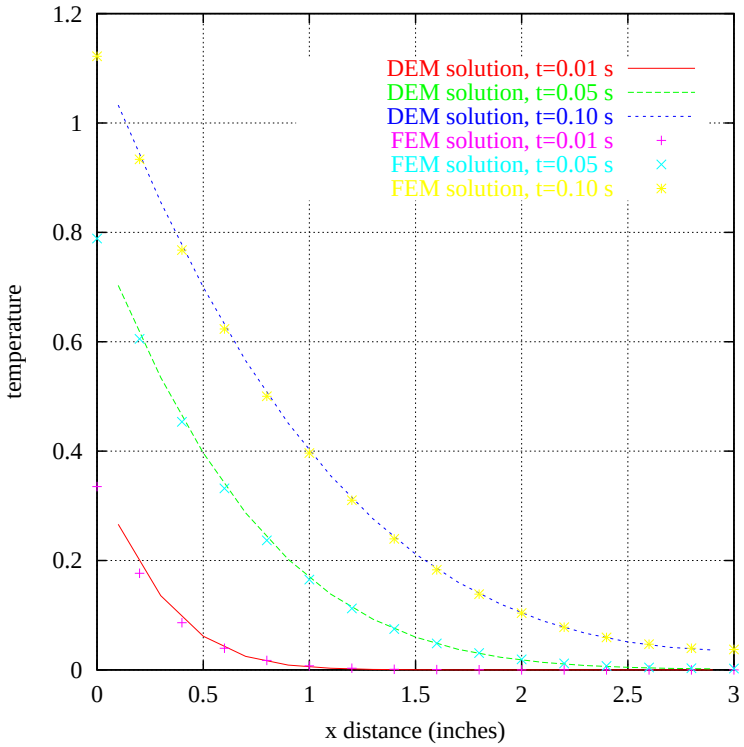

Figure 7.6: Semi-infinite solid subjected to a unit surface heat flux – temperature distribution – comparison of FEM and DEM results

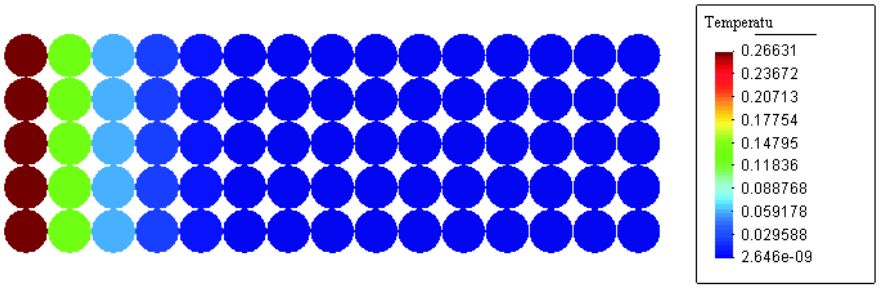

a) t = 0.1 s

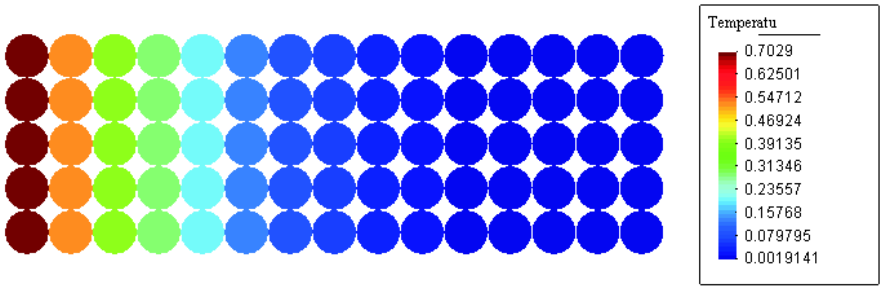

b) t = 0.5 s

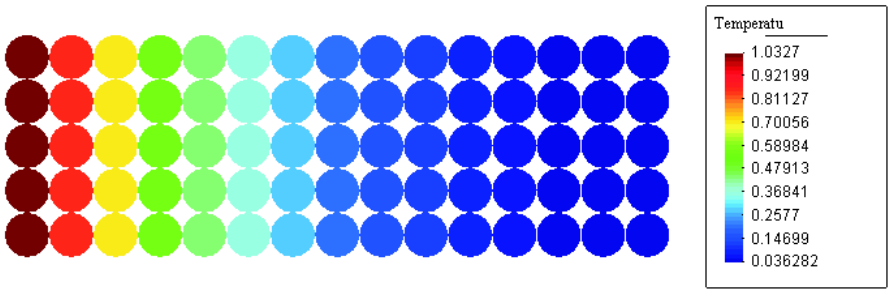

c) t = 1.0 s

Figure 7.7: Semi-infinite solid subjected to a unit surface heat flux - temperature distribution at different time instants (discrete element method results)

7.6.3 Transient heat conduction in an infinite parallel-sided slab

A one-inch thick slab, infinite in extent, is initially at 0°F. At time $t = 0^+$, both faces of the slab are raised to 100°F and held constant for all time. The thermal material properties are as follows:

- specific heat $c = 2$ BTU$\cdot$ in/(sec^{2}lb$\cdot$°F),
- heat conductivity $\kappa = 6$ BTU/(sec$\cdot$ m$\cdot$°F),
- mass density $\rho = 3$ sec^{2}lb/in^4

The finite element model taking advantage of the plane symmetry is shown in Fig. **??**. Comparison between FEM and DEM solutions is shown in Fig. 7.9 for the temperature distributions. A very good agreement is found out. The DEM model with temperature distributions for different time instants is shown in Fig. 7.10.

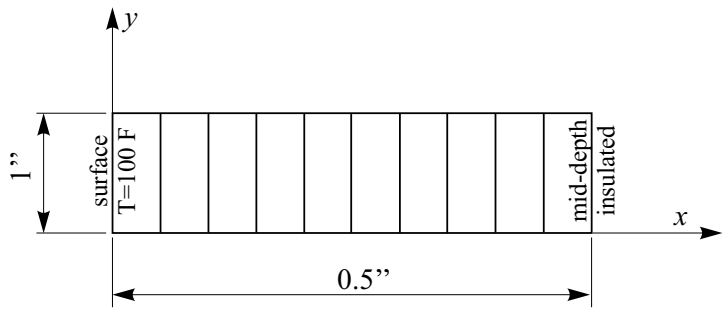

Figure 7.8: Transient heat conduction in an infinite parallel-sided slab – finite element model

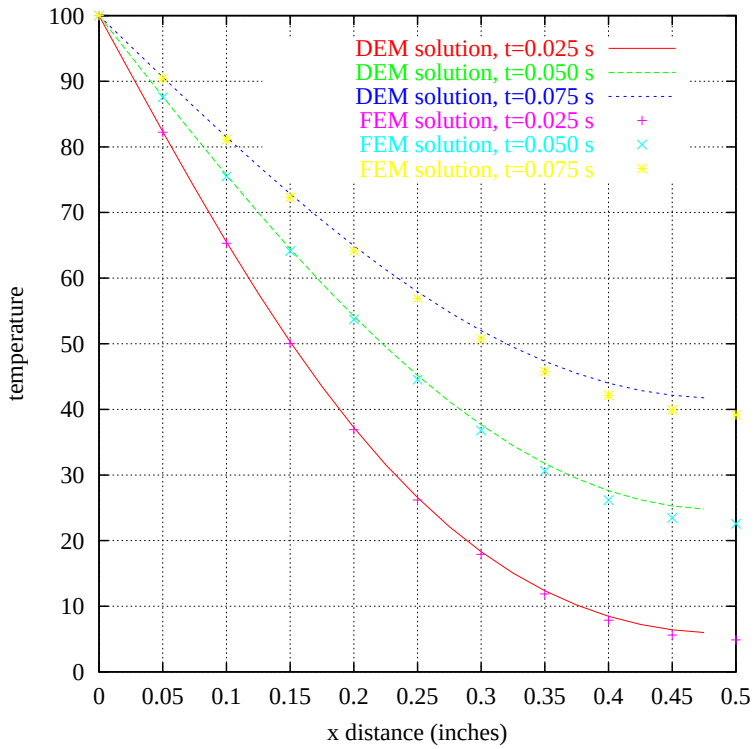

Figure 7.9: Transient heat conduction in an infinite parallel-sided slab – temperature distribution – comparison of FEM and DEM results

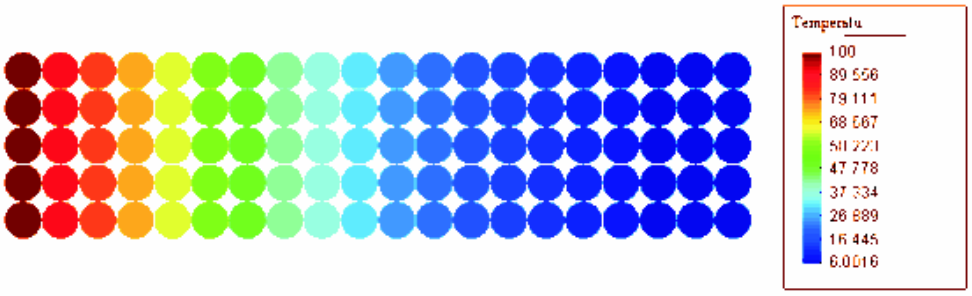

a) t = 0.025 s

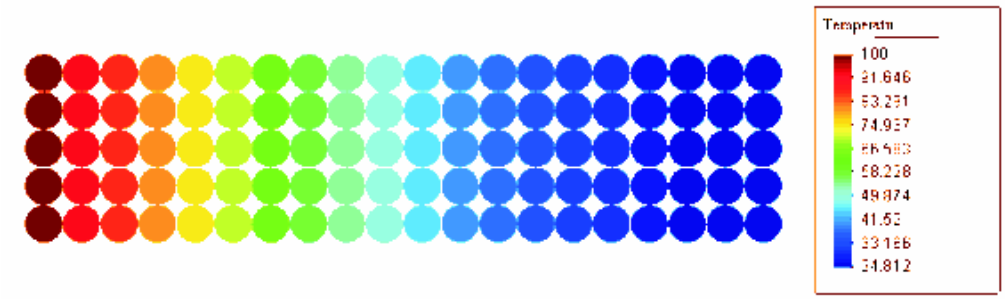

b) t = 0.050 s

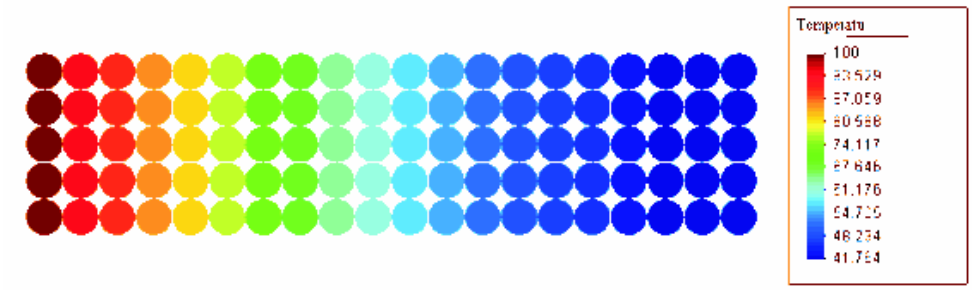

c) t = 0.075 s

Figure 7.10: Transient heat conduction in an infinite parallel-sided slab – temperature distribution at different time instants (discrete element method results)

Chapter 8

Numerical simulation of rock cutting and wear evaluation

8.1 2D mechanical simulation of rock cutting – model I

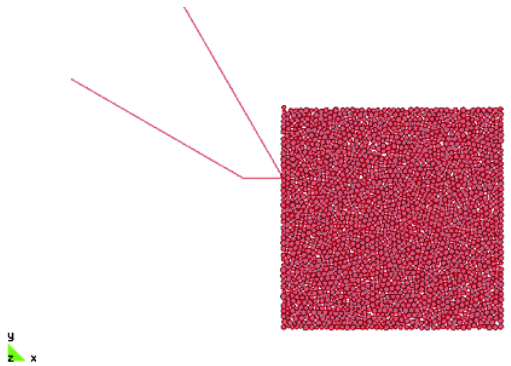

Figure 8.1: Initial set-up of 2D model of rock cutting – tool discretized with straight segments

2D mechanical simulation of rock cutting has been carried out using a model shown in Fig. 8.1. Material sample 109×109 mm is represented by an assembly of randomly compacted 2100 discs of radii 1–1.5 mm. Other model parameters are as follows: contact stiffness in the normal and tangential directions $k_n = k_T = 20$ GPa, the cohesive bond strengths $R_n = 0.1$ MN/m, $R_T = 1$ MN/m, and the friction coefficient $\mu = 0.839$. The surface of the rigid tool has been modelled with straight segments. The following parameters have been assumed for the tool-rock interface: contact stiffness modulus $k_n = 20$ GPa, Coulomb friction coefficient $\mu = 0.839$.

Cutting has been carried out with prescribed horizontal velocity of the tool 0.04 m/s. Process of cutting is shown in Fig. 8.2. In this figure we can also see the failure mode – particles with broken bonds are coloured in blue. It can be clearly seen formation of a chip during cutting typical for brittle materials.

Initial wear pattern has been obtained in the analysis. The wear distribution calculated for one work cycle is shown in Fig. 8.3. Calculated wear was obtained using Eq. (6.1) with assumed parameters $\bar{k} = 1$ and $H = 1$ Pa. Obtained values although not real show distribution of wear on the surface — zones with higher wear are indicated.

8.2 2D mechanical simulation of rock cutting (model II)

2D simulation of rock cutting has been carried out using the model shown in Fig. 8.4. Material sample is the same as in model I, and the rigid tool is now modelled with distinct elements. The tool is modelled with 4649 equal particles of radius 0.5 mm (average radius of particles modelling rock 1.25 mm). The following parameters have been assumed for the tool-rock interface: contact stiffness modulus $k_n = 20$ GPa, Coulomb friction coefficient $\mu = 0.839$. Cutting has been carried out with prescribed horizontal velocity of the tool 0.04 m/s. Analysis has been carried out without modification of tool shape. Process of cutting is shown in Fig. 8.5. Failure mode is presented in Fig. 8.5 by colouring blue particles with broken bonds. Formation of a chip in the initial phase of the cutting can also be seen in this simulation. The same model and the same process parameters have been used for the simulation of cutting with modification of tool shape due to wear. Wear has been calculated according to Eq. (6.1) using the constants $\bar{k} = 5 \cdot 10^{-9}$ and $H = 1$ Pa, which produced accelerated wear. This allowed us to test our algorithm in short simulation. Tool shape was modified by removal of particles from the surface when the accumulated wear (thickness) exceeded their diameter. Process of cutting and failure mode with formation of a chip are shown in Fig. 8.6 for different time instants. Profile of wear on the surface of the tool is shown for different stages in Fig. 8.7. Some of the particles on the cutting tip have been eliminated. This can be seen better in detail presented in Fig. 8.8.

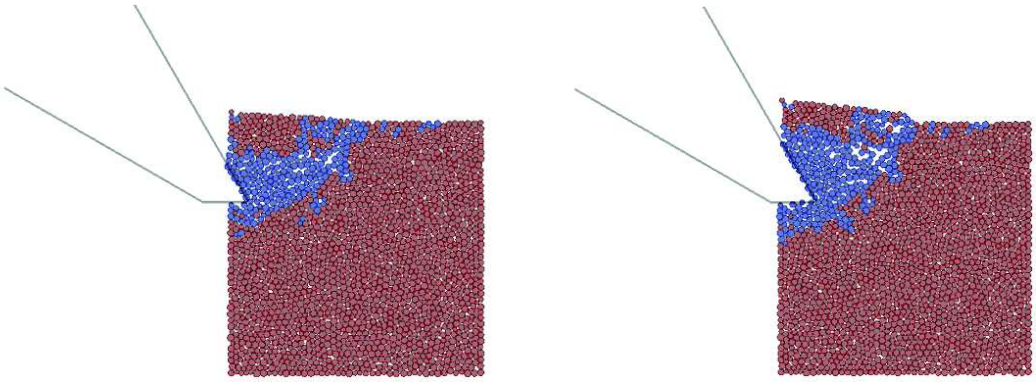

a) t = 0.2 s

b) t = 0.4 s

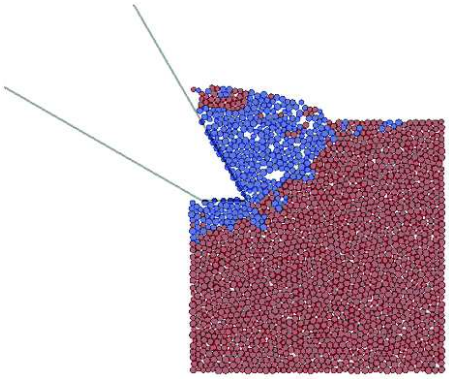

c) t = 0.6 s

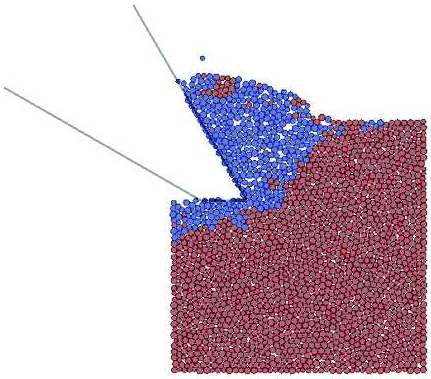

d) t = 0.8 s

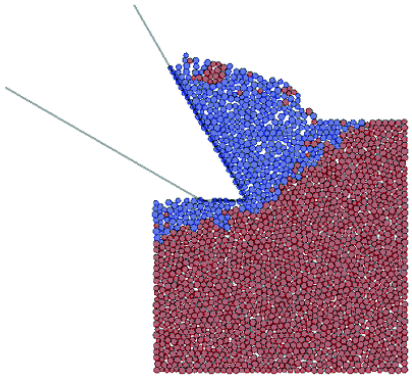

e) t = 1.0 s

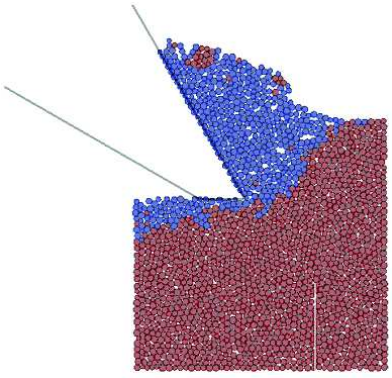

f) t = 1.2 s

Figure 8.2: Process of cutting - failure mode

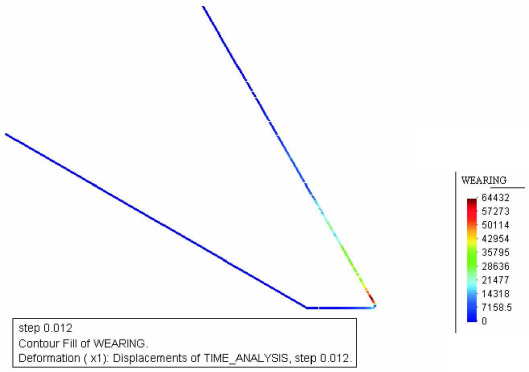

Figure 8.3: Distribution of wear on the tool surface at the end of work cycle (model I)

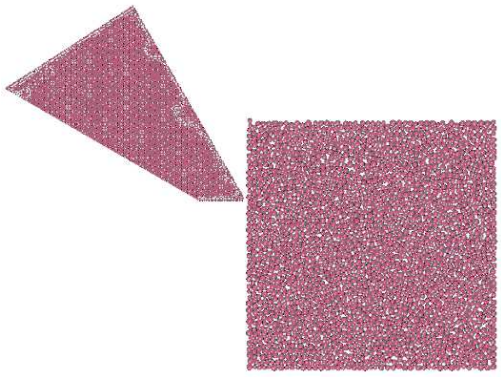

Figure 8.4: Initial set-up of 2D model of rock cutting – tool discretized with distinct elements

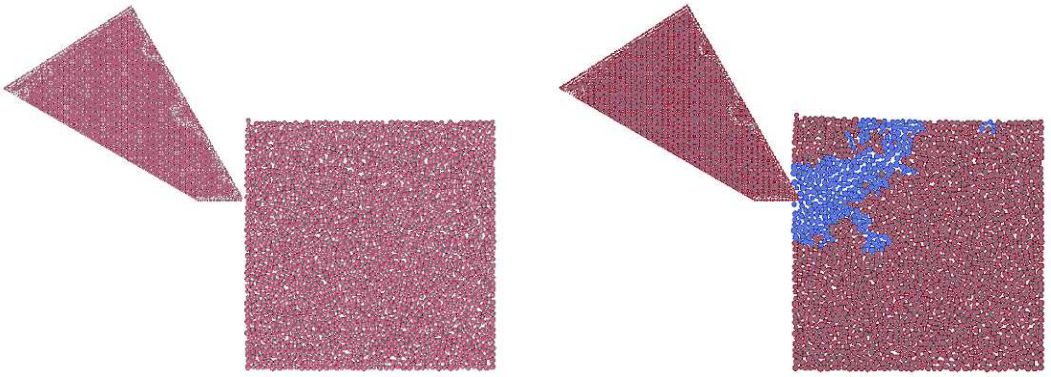

a) t = 0.0 s

b) t = 0.1 s

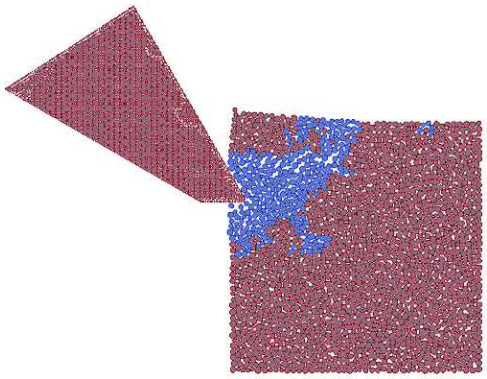

c) t = 0.2 s

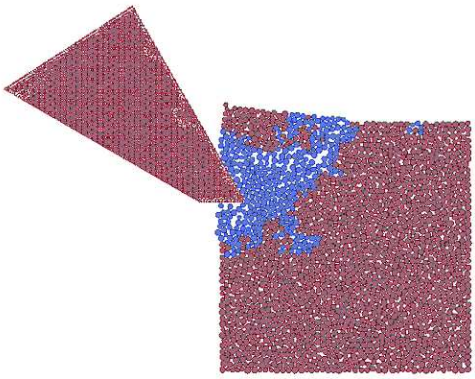

d) t = 0.3 s

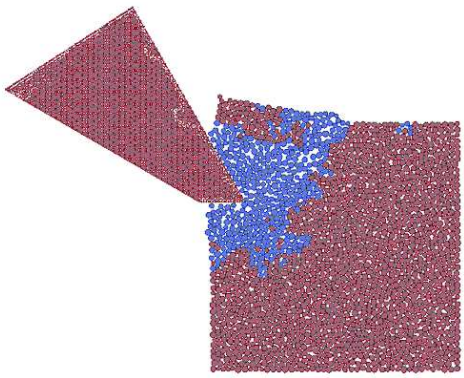

e) t = 0.4 s

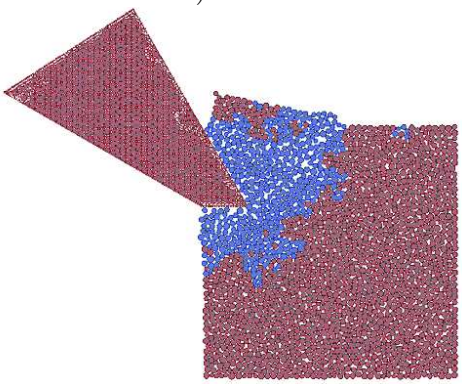

f) t = 0.5 s

Figure 8.5: Process of cutting with failure mode (model II, tool shape without change)

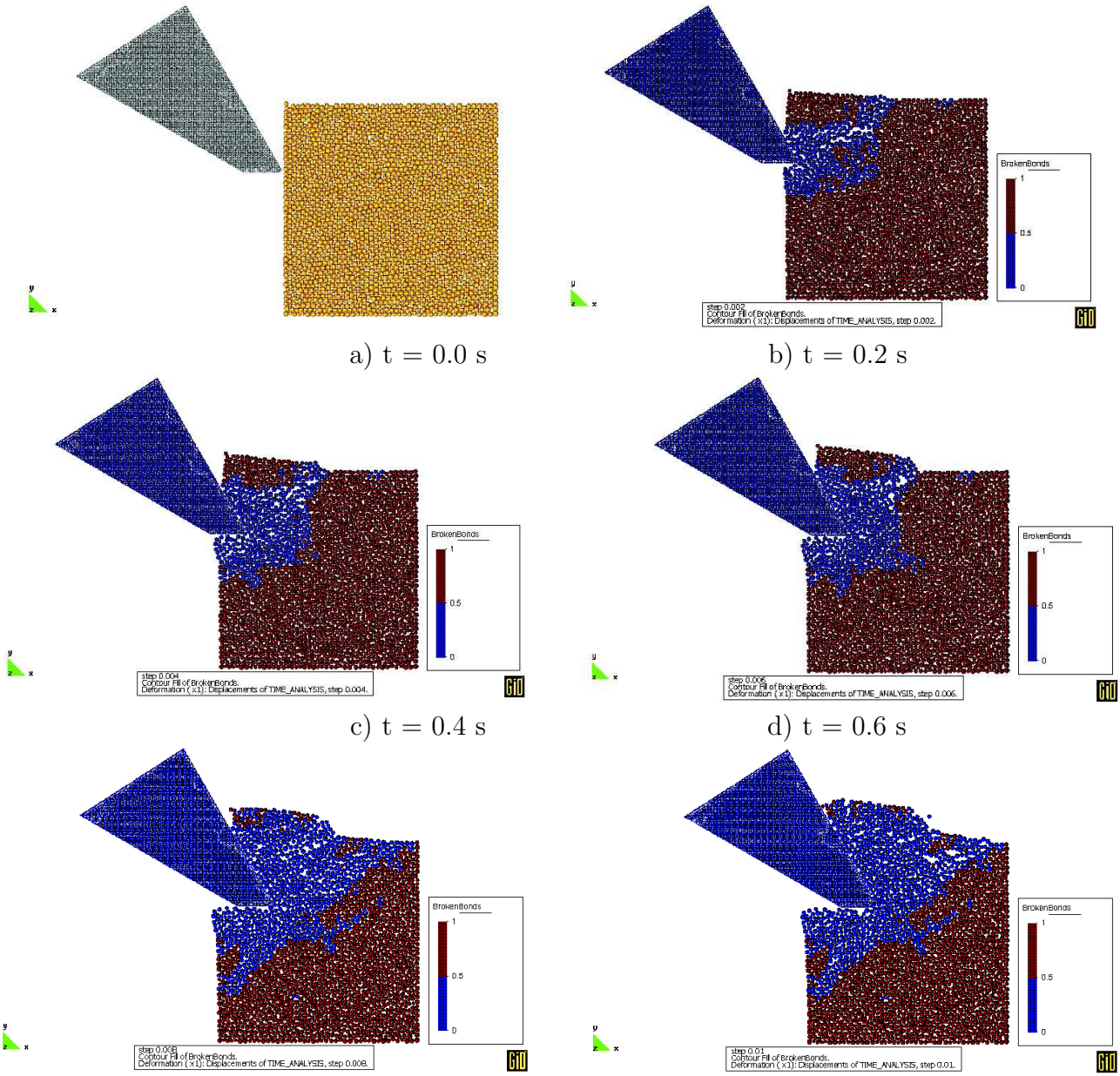

a) t = 0.0 s b) t = 0.2 s

c) t = 0.4 s d) t = 0.6 s

e) t = 0.8 s f) t = 1.0 s

Figure 8.6: Process of cutting with failure mode (model II, tool shape changed)

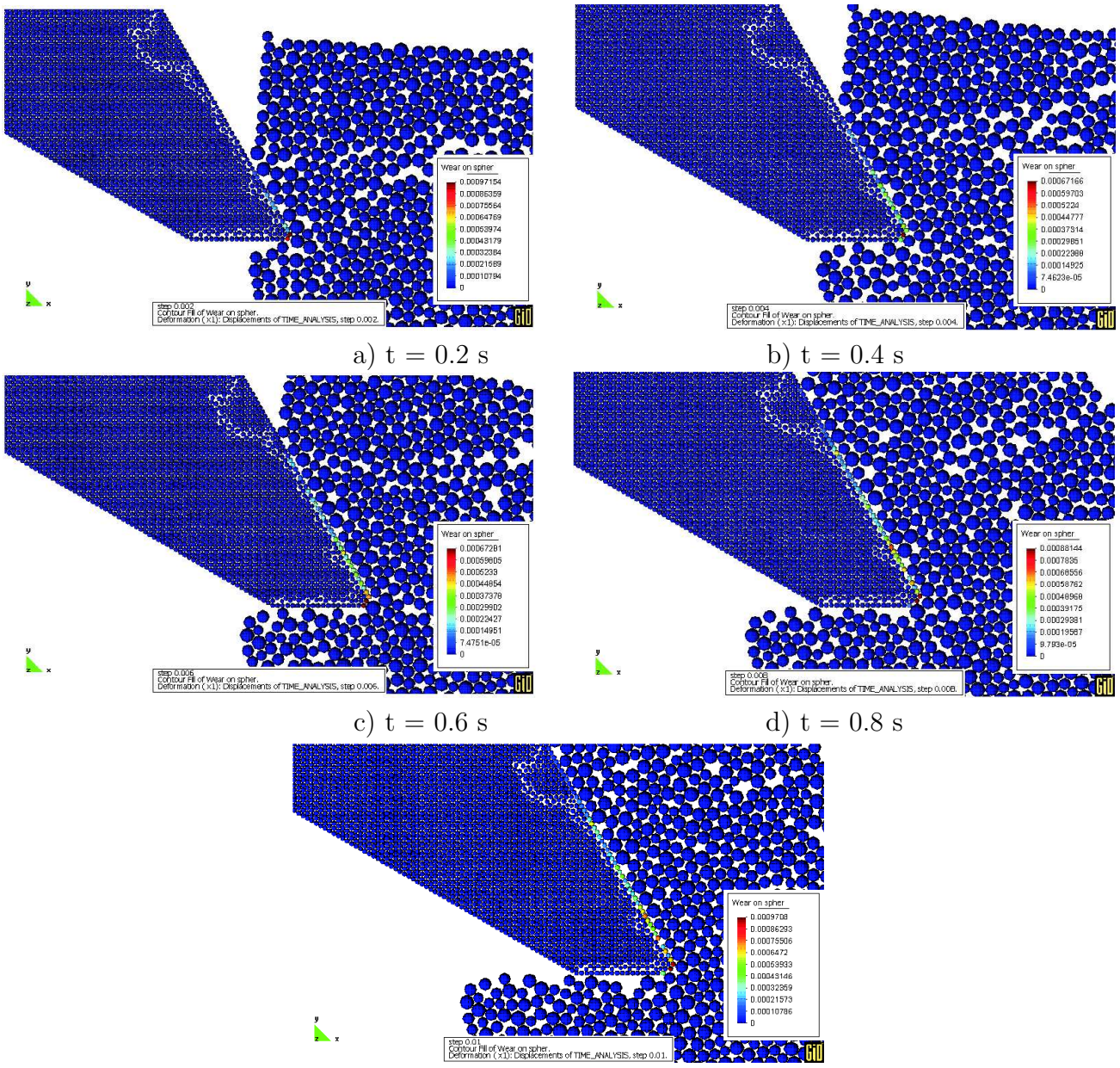

a) t = 0.2 s

b) t = 0.4 s

c) t = 0.6 s

d) t = 0.8 s

e) t = 1.0 s

Figure 8.7: Process of cutting with profile of wear (model II, tool shape changed)

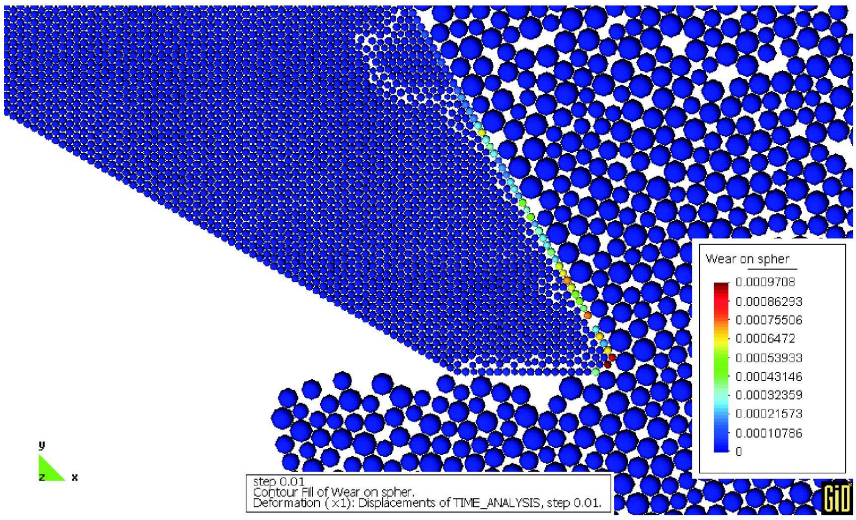

Figure 8.8: Profile of wear at time instant t = 1.0 s (model II, tool shape changed) – detail

Chapter 9

Wear evaluation in multi-cycle analysis of rock cutting

9.1 Methodology

The objective of the present study is determination of the wear of a cutting tool due to interaction with sandstone during the excavation process.

To disc assembly modelling the sandstone sample and micro-scale parameters have been previously determined. The cutting tool travels at a constant prescribed velocity of 4m/s. The wear process have been accelerated, so that lower computational time have been needed.

First, we excavate the material during a brief lapse of time (0.005 s). The final configuration of this stage (Fig. 9.1) has been used as the initial configuration of the following stages. At the end of the stages we move back the cutting tool and continue excavating in the next stage.

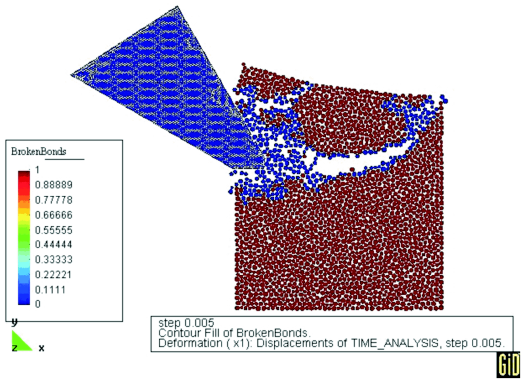

Figure 9.1: Configuration at $t = 0.005$ s from the beginning of the analysis

9.2 Simulation of wear of the test tooth

9.2.1 Description of the model

The particles that form the cutting tool have been radii randomly generated in the range between 0.4 and 0.52 mm. The tooth material has been assumed steel MET 91.

The constitutive parameters of the contact interface between spheres and the cutting tools are the following:

- contact stiffness in the normal direction $k_n = 90$ GPa ,
- Coulomb friction coefficient $\mu = 0.3$,
- wear constant k and steel hardness in the ambient temperature $H(T = 20°\text{C})$ as given in Sec. 6.6.

The simulation has been carried out using the constant tooth hardness. The oscillations with highest frequencies are damped out by adequate damping at the contact interface between the spheres that conform the material and the cutting tool (90% of the critical damping). We also apply a global viscous damping so that the lowest vibration modes decrease.

9.2.2 Results

Tooth shapes at different stages of wear are shown in Fig. 9.2. During 0.203 seconds of excavation 40% of the tool mass has been lost. Figure 9.3 presents the tool mass loss as a fraction of the initial tool mass versus analysis time. Scaling analysis time by 7000 allows us to obtain the wear curve, which agrees with experimental curves for a ripper tooth, cf. Fig. 9.4.

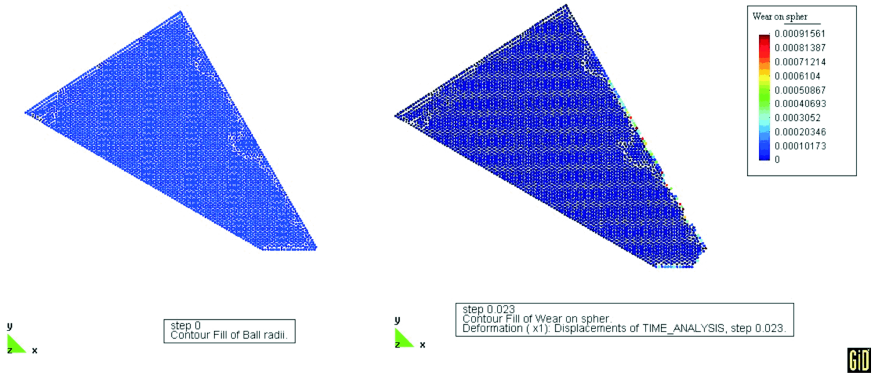

a) t = 0.0 s b) t = 0.023 s

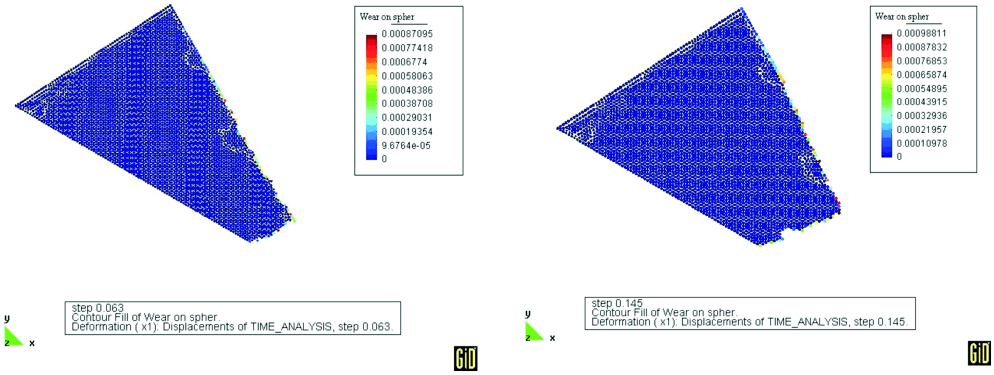

c) t = 0.063 s d) t = 0.145 s

Figure 9.2: Shape of cutting tool at different stages

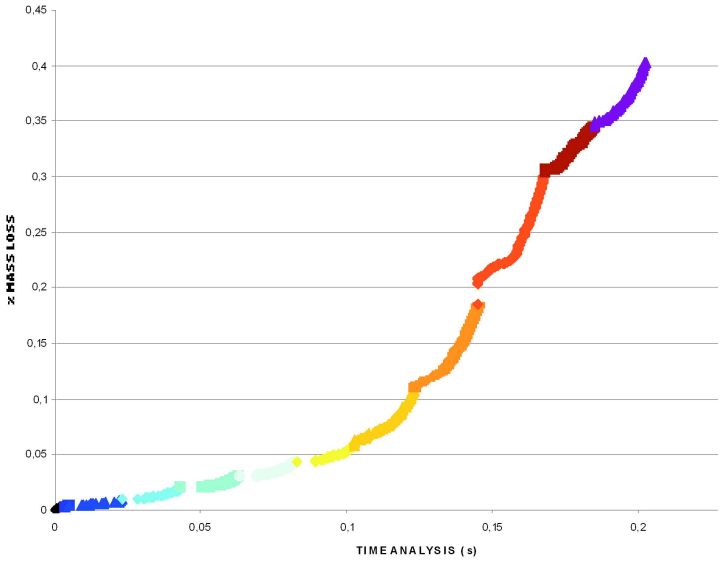

Figure 9.3: Mass loss fraction versus analysis time

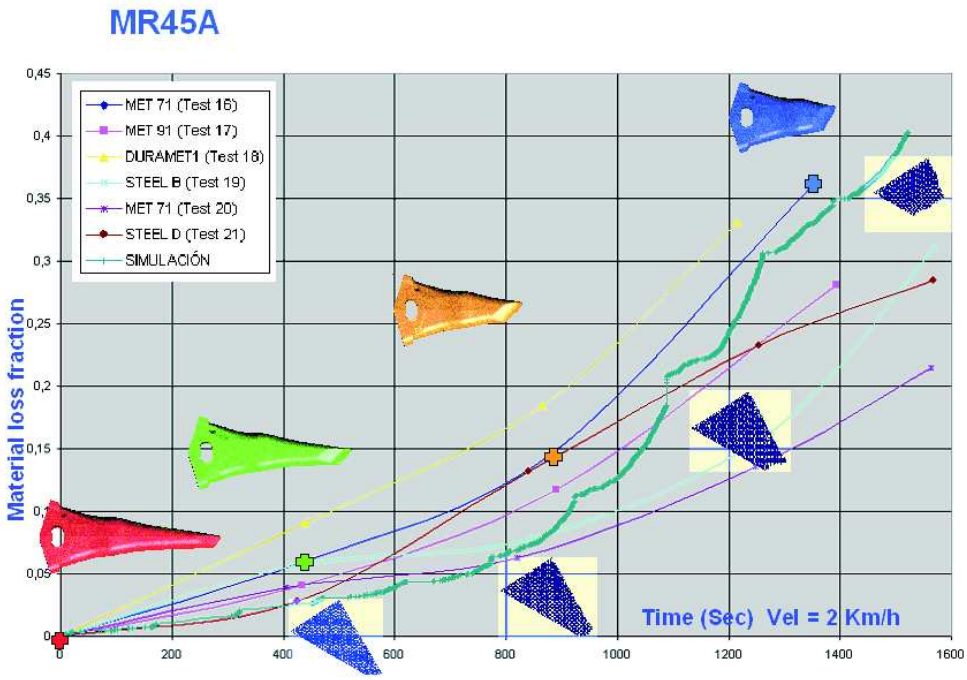

Figure 9.4: Mass loss fraction versus analysis time — comparison of experimental and simulation wear curves

9.3 Wear simulation of a ripper tooth

9.3.1 Model definition

Numerical simulation of wear of a ripper tooth has been carried out. Initial geometry of the model is shown in Fig. 9.5. Material sample of dimensions 109 × 109 mm is represented by an assembly of randomly compacted 2100 discs of radii 1–1.5 mm. Other model parameters are as follows: contact stiffness in the normal and tangential directions $k_n = k_T = 90$ GPa, the cohesive bond strengths $R_n = 0.1$ MN/m, $R_T = 1$ MN/m, and the friction coefficient $\mu = 0.839$. The material macroscopic behaviour corresponds to sandstone properties which has been found in previous numerical tests.

The rigid tool is modelled with distinct elements, 6500 disc of radii randomly varying from 0.4 to 0.6 mm. The following parameters have been assumed for the tool-rock interface: contact stiffness modulus $k_n = 20$ GPa, Coulomb friction coefficient $\mu = 0.3$. The tooth material has been assumed steel MET 91. Wear constant k and steel hardness in the ambient temperature $H(T = 20°\text{C})$ are given in Sec. 6.6. The simulation has been carried out using the constant tooth hardness. Wear has been calculated using the constant k scaled 7000 times, which previously has been found out as giving good agreement with field experiments.

Cutting has been carried out with prescribed horizontal velocity of the tool 4 m/s.

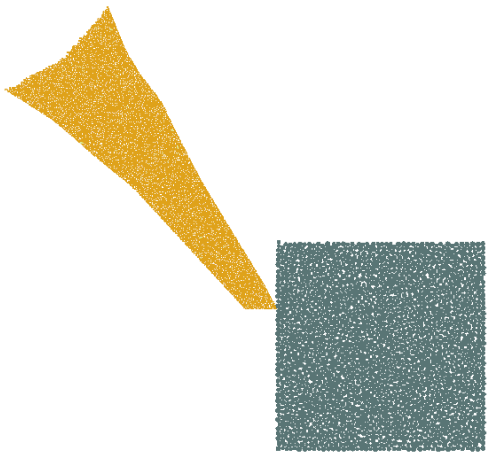

Figure 9.5: Initial set-up of 2D model of rock cutting with a ripper

9.3.2 Numerical results

Wear analysis has been carried out in 20 cycles. Cutting of the rock at initial step is shown in Fig. 9.6. In figure 9.7 we can see the failure mode — particles with broken bonds are coloured in blue. It can be clearly seen formation of a chip during cutting typical for brittle materials. Figure 9.8 presents wear distribution on the tooth surface at the initial stage of wear.

Process of cutting, failure mode and wear and distribution on the tool surface at different stages of a tooth wear are shown in Figs. 9.9–9.11. Significant wear of the tooth can be seen. Quantitative numerical results (wear amounts) have been compared with experimental results in Fig. 9.12. A fairly good agreement can be seen.

9.3.3 Conclusions

Numerical results agree pretty well with experimental results. Numerical wear profile agrees with change of shape of real teeth. Quantitative results (wear amounts) have also been obtained by scaling wear parameters to produce accelerated wear

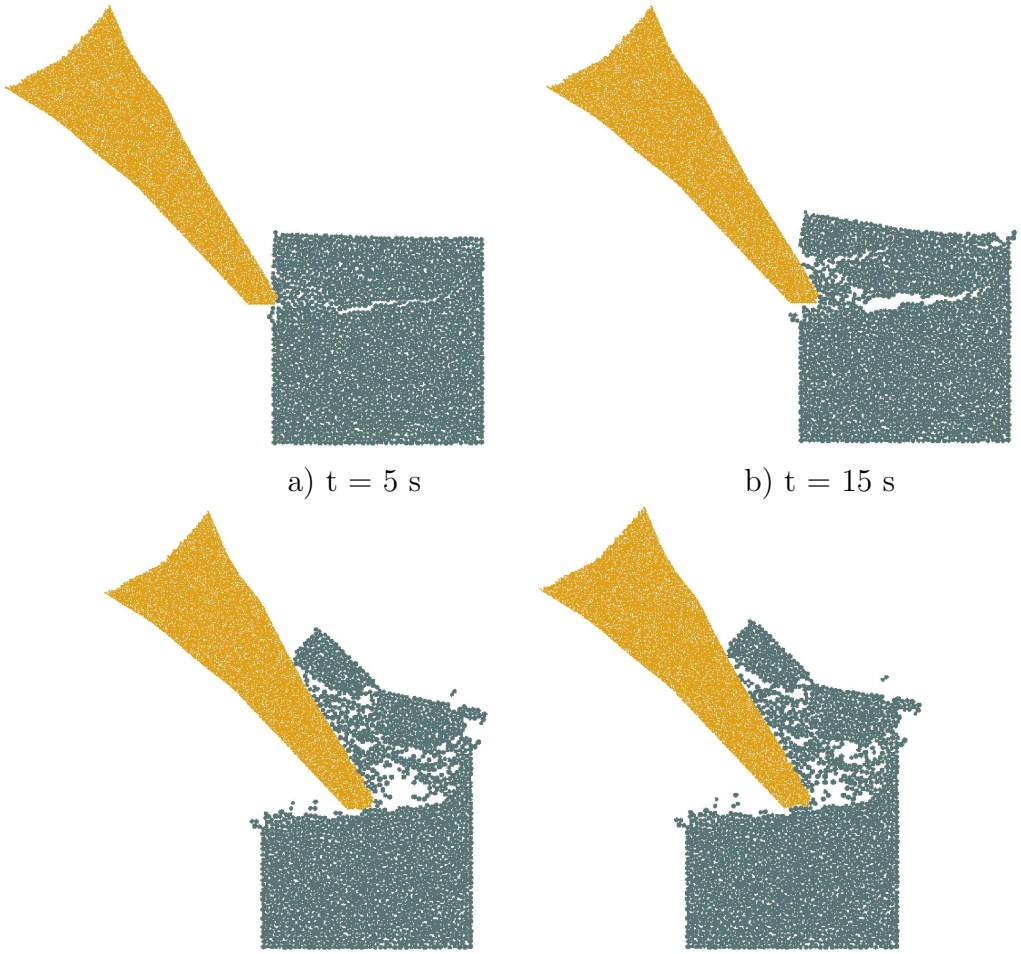

a) t = 5 s b) t = 15 s

c) t = 90 s d) t = 100 s

Figure 9.6: Process of cutting at initial stage

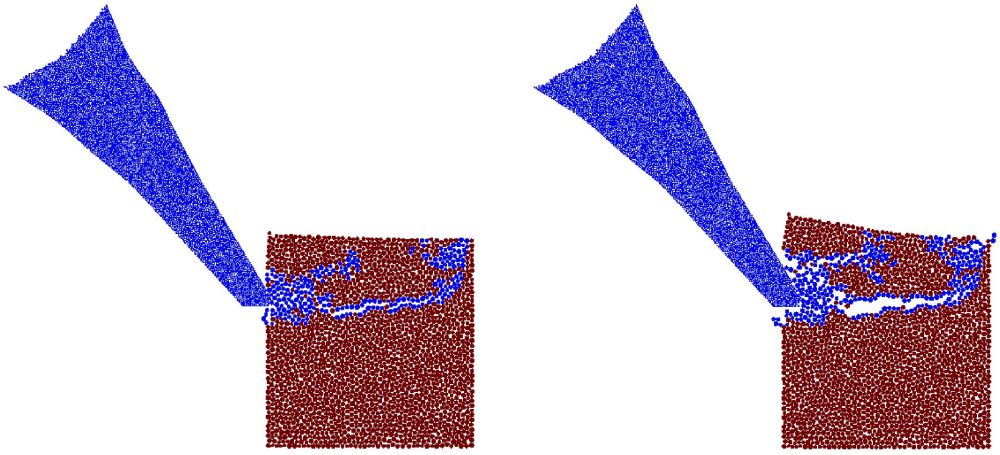

a) t = 5 s

b) t = 15 s

c) t = 90 s

d) t = 100 s

Figure 9.7: Process of cutting — failure mode at initial stage

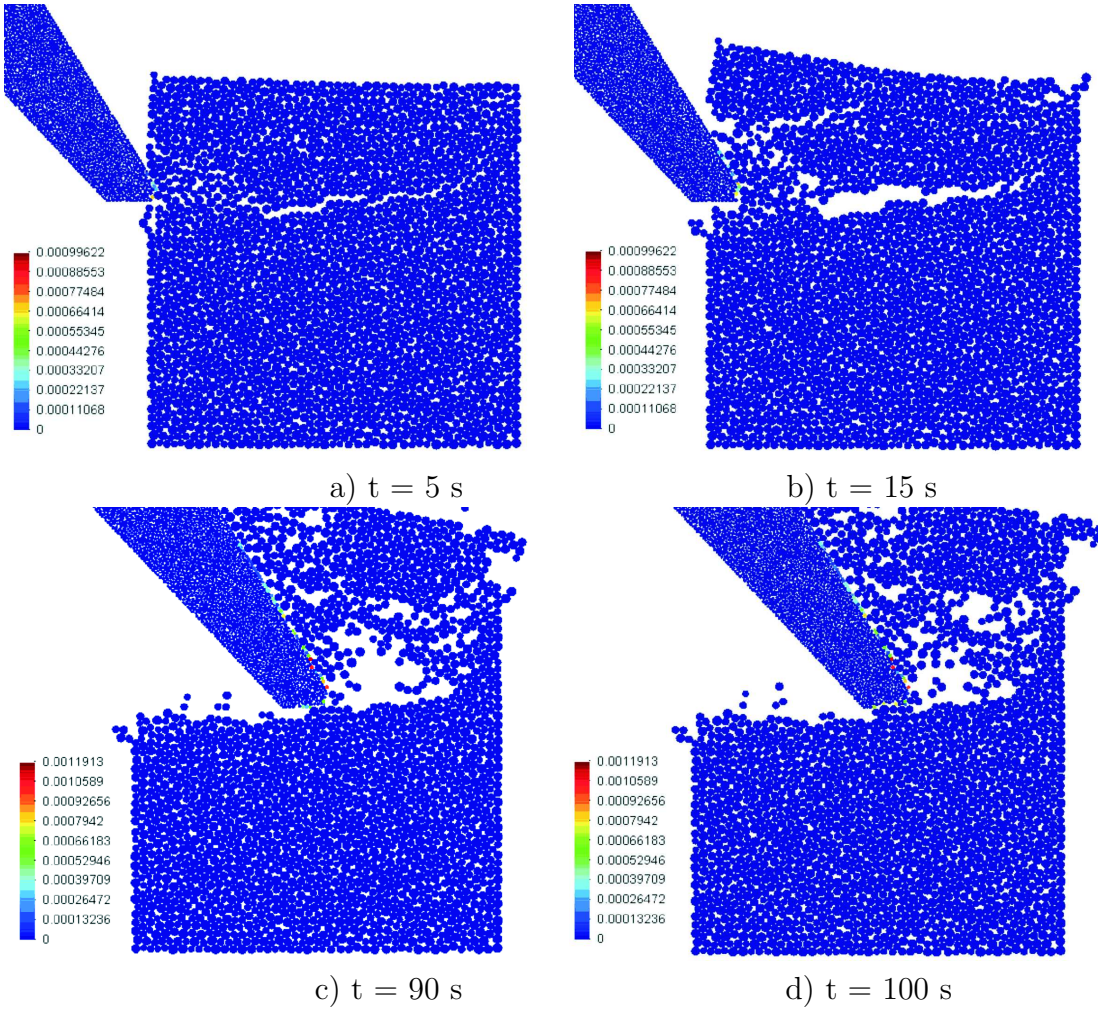

Figure 9.8: Process of cutting — wear distribution on the tool surface at initial stage

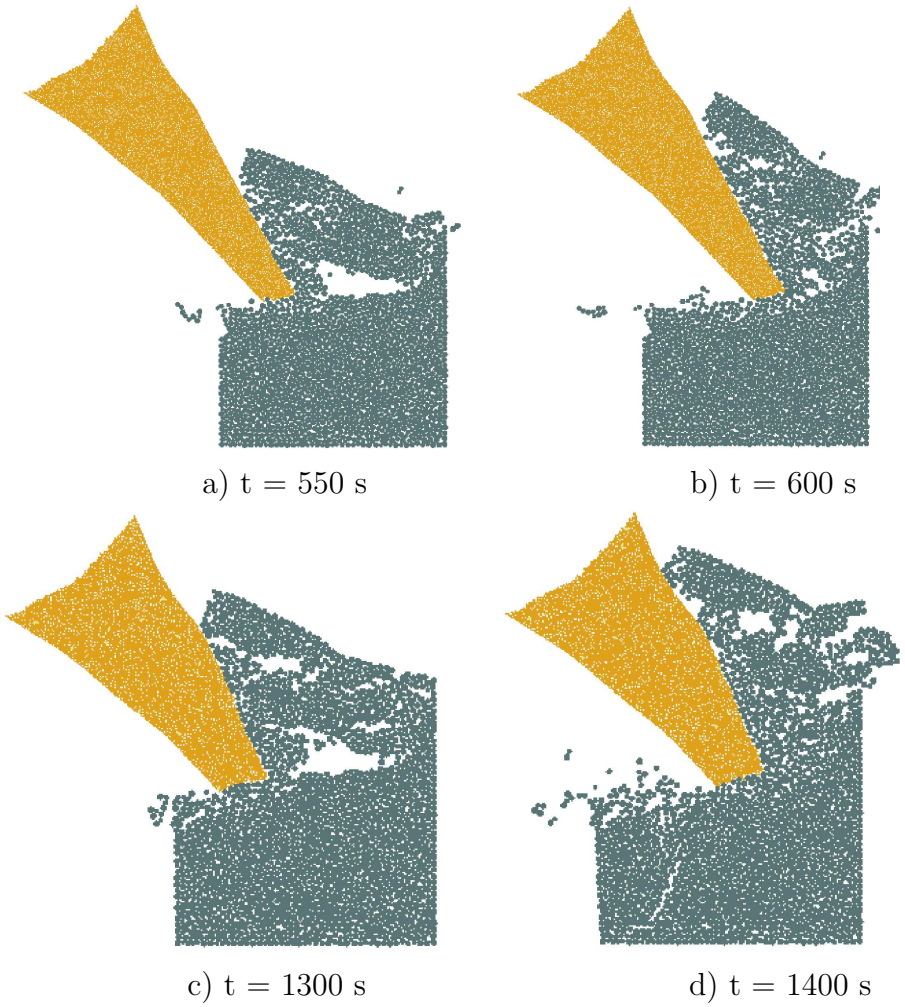

a) t = 550 s b) t = 600 s

c) t = 1300 s d) t = 1400 s

Figure 9.9: Process of cutting at different stages of wear

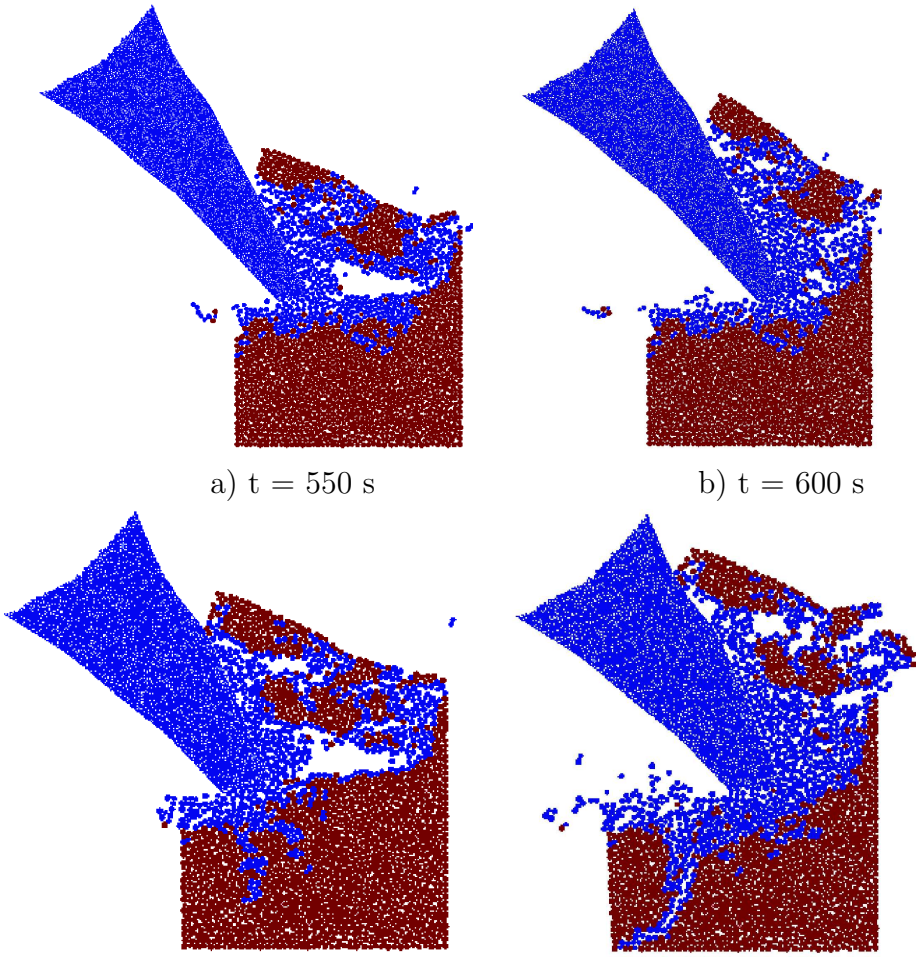

a) t = 550 s b) t = 600 s

c) t = 1300 s d) t = 1400 s

Figure 9.10: Process of cutting — failure mode at different stages of wear

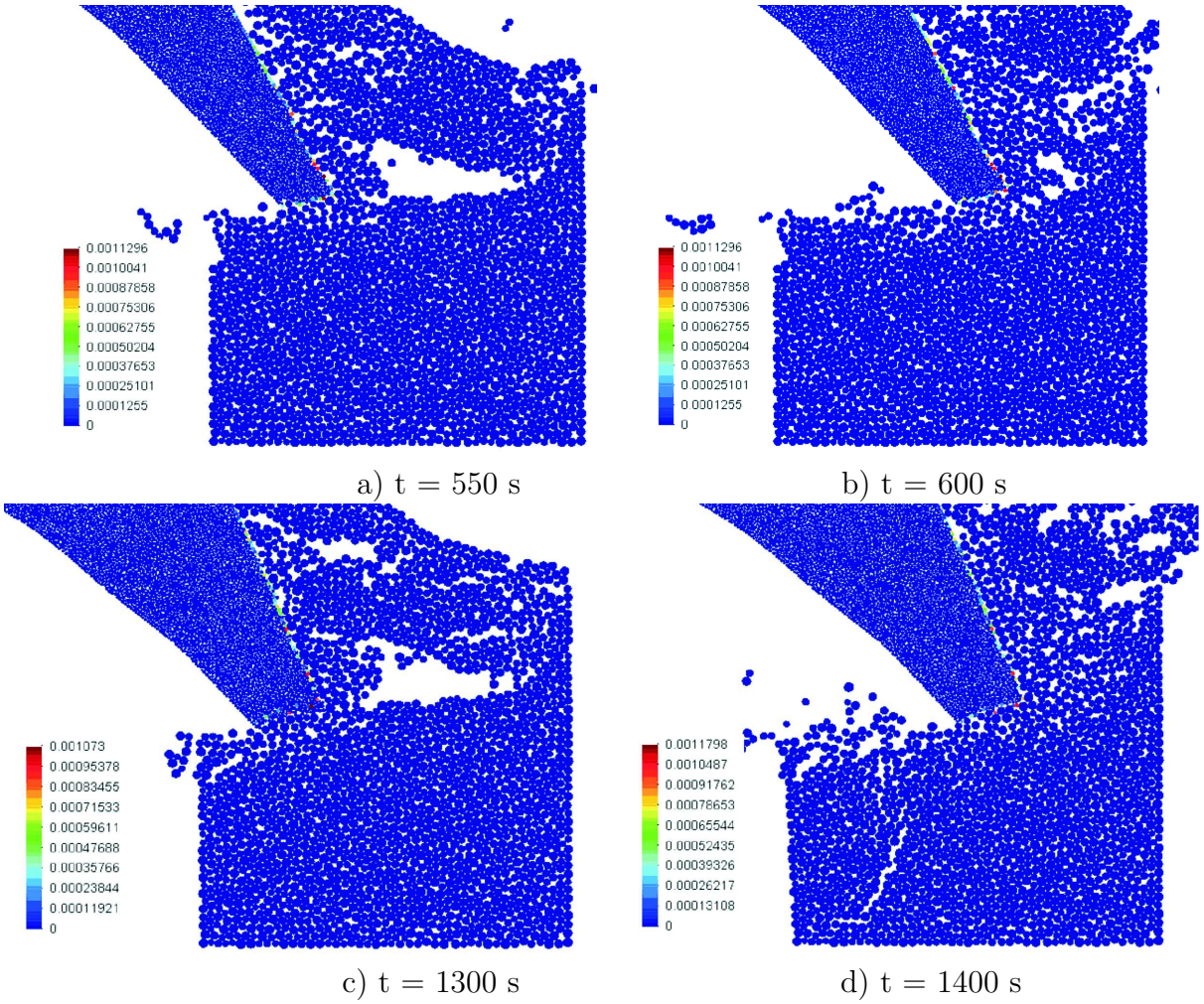

a) t = 550 s b) t = 600 s

c) t = 1300 s d) t = 1400 s

Figure 9.11: Process of cutting — wear distribution on the tool surface

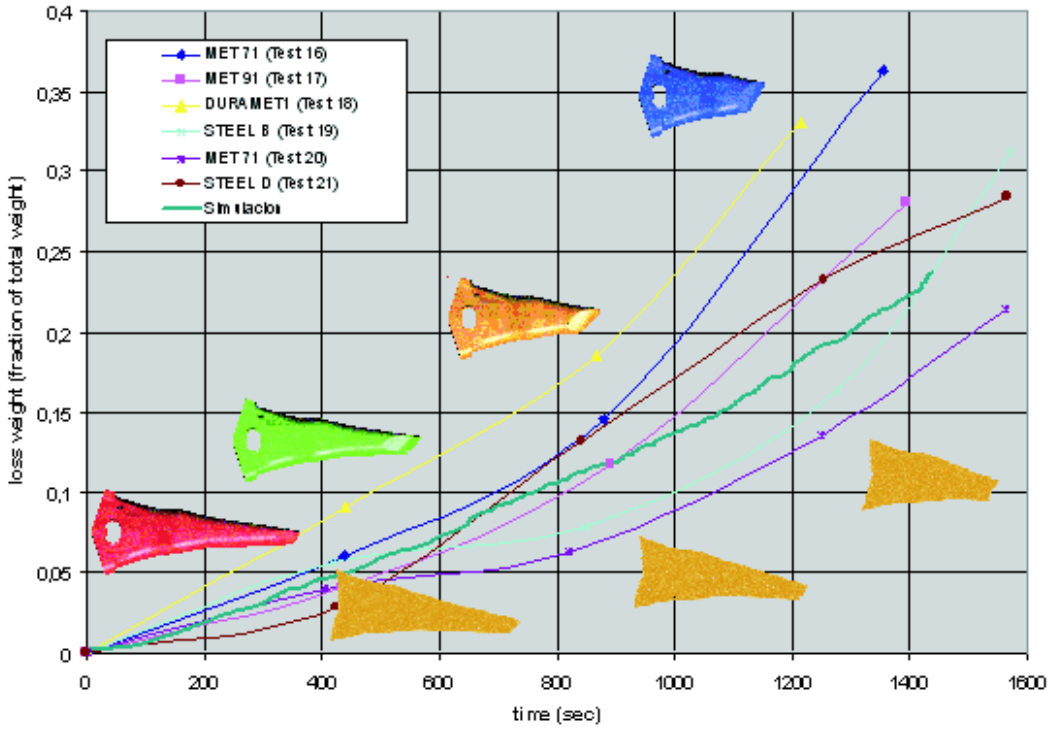

Figure 9.12: Comparison of experimental and simulation wear curves for a ripper tooth

Chapter 10

Thermo-mechanical transient analysis of rock cutting

10.1 2D thermo-mechanical simulation of rock cutting

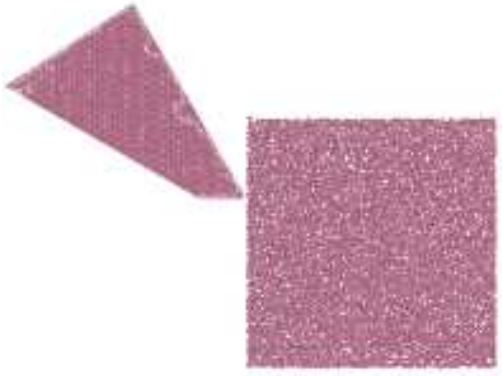

Figure 10.1: Initial set-up of 2D model of rock cutting

2D thermo-mechanical simulation of rock cutting has been carried out using a model shown in Fig. 10.1. Material sample 109 × 109 mm is represented by an assembly of randomly compacted 2100 discs of radii 1–1.5 mm. Other model parameters are as follows: contact stiffness in the normal and tangential directions $k_n = k_T = 20$ GPa, the cohesive bond strengths $R_n = 0.1$ MN/m, $R_T = 1$ MN/m, and the friction coefficient $\mu = 0.839$. The rigid tool is modelled with distinct elements, 4649 equal particles of radius 0.5 mm (average radius of particles modelling rock 1.25 mm). The following parameters have been assumed for the tool-rock interface: contact stiffness modulus $k_n = 20$ GPa, Coulomb friction coefficient $\mu = 0.839$. The following thermal

properties have been assumed:

- for rock
  heat capacity $c = 3000$ J/(kg·K),
  heat conductivity $\kappa = 0.1$ W/(m·K)

- for steel
  heat capacity $c = 450$ J/(kg·K),
  heat conductivity $\kappa = 60$ W/(m·K)

Cutting has been carried out with prescribed horizontal velocity of the tool 0.04 m/s. Process of cutting is shown in Fig. 10.2. In this figure we can also see the failure mode – particles with broken bonds are coloured in blue. It can be clearly seen formation of a chip during cutting typical for brittle materials. Wear has been calculated according to Eq. (6.9) using the constants $\bar{k} = 10^{-10}$, $H = 100$ Pa. Little wear was produced in one cycle. The objective example of the example was to test thermal analysis including heat generation and conductance. Two cases has been studied. In the first case no heat conductance was allowed, heat was assumed to be adsorbed by particles which generate heat. In the second case full thermal analysis with heat conductance by the tool and rock has been carried out. Temperature distribution at different time instants for the case without conductance is shown in Figs. 10.3 and 10.4. Temperature distribution at different time instants for the full thermal analysis is presented in Fig. 10.5. We can see increase of temperature in the zone of contact between the tool and rock.

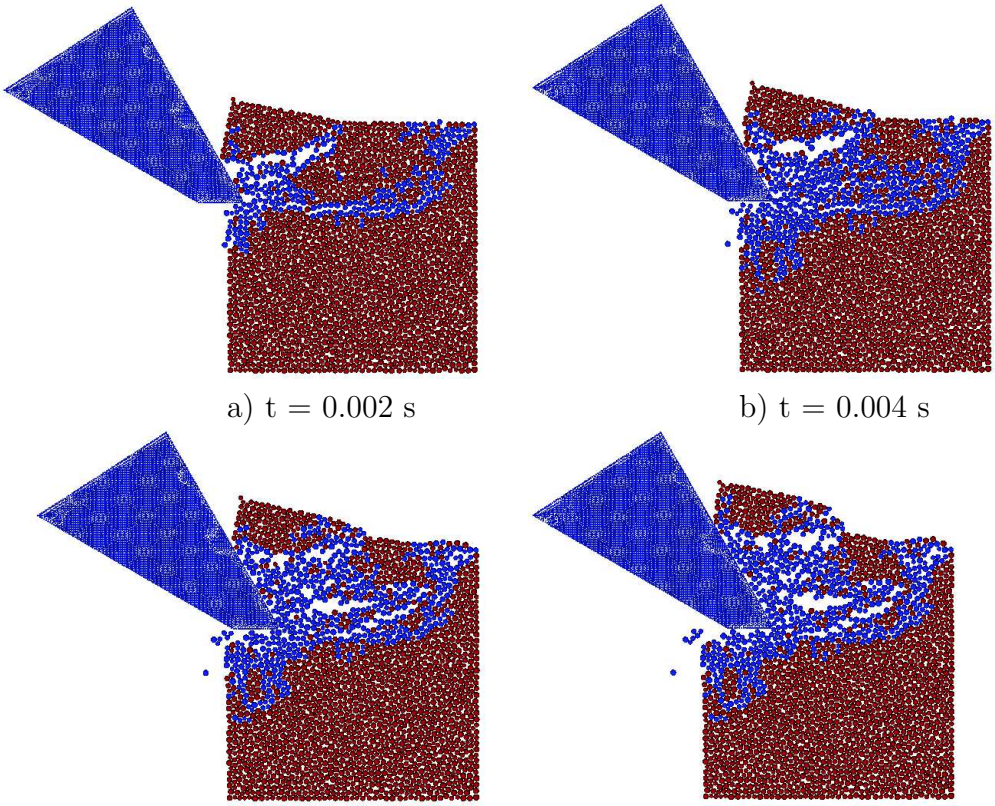

a) t = 0.002 s b) t = 0.004 s

c) t = 0.006 s d) t = 0.008 s

Figure 10.2: Process of cutting - failure mode

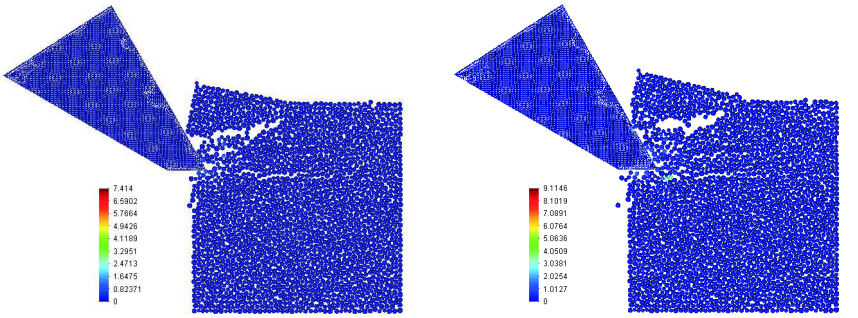

a) t = 0.002 s b) t = 0.004 s

c) t = 0.006 s d) t = 0.008 s

Figure 10.3: Process of cutting – temperature distribution obtained in the solution without heat conductance

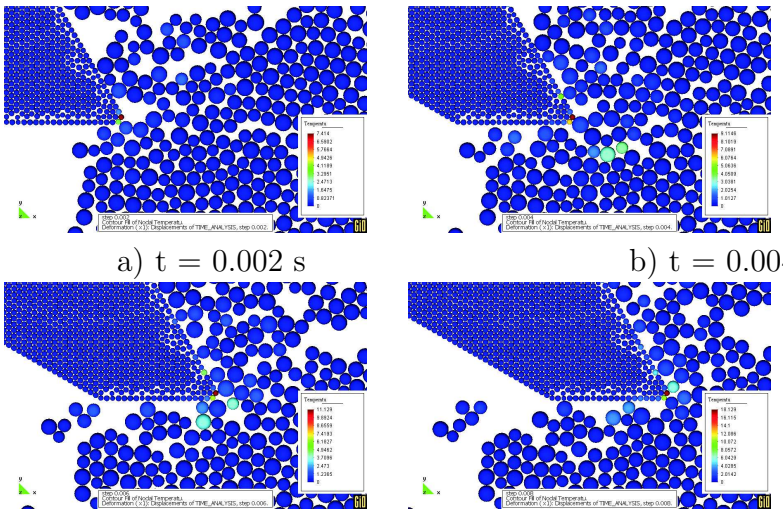

a) t = 0.002 s b) t = 0.004 s

c) t = 0.006 s d) t = 0.008 s

Figure 10.4: Process of cutting – temperature distribution obtained in the solution without heat conductance (zoom)

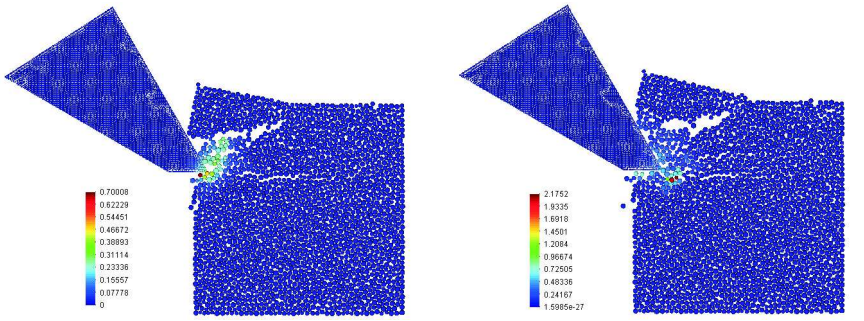

a) t = 0.002 s b) t = 0.004 s

c) t = 0.006 s d) t = 0.008 s

Figure 10.5: Process of cutting – temperature distribution (full thermal analysis)

Chapter 11

Thermomechanical analysis of wear of a ripper

11.1 Model definition

Thermo-mechanical numerical simulation of wear of a ripper tooth has been carried out Geometry of the rock sample and tooth as well as mechanical parameters have been assumed similar to those used in Sec. 9.3.

Material sample (Fig. 9.5) of dimensions 109×109 mm is represented by an assembly of randomly compacted 2100 discs of radii $1 \div 1.5$ mm. Mechanical model parameters are as follows: contact stiffness in the normal and tangential directions $k_n = k_T = 90$ GPa, the cohesive bond strengths $R_n = 0.1$ MN/m, $R_T = 1$ MN/m, and the friction coefficient $\mu = 0.839$. The material macroscopic behaviour corresponds to sandstone properties which has been found in previous numerical tests.

The rigid tool is modelled with distinct elements, 6500 disc of radii randomly varying from 0.4 to 0.6 mm. The following parameters have been assumed for the tool-rock interface: contact stiffness modulus $k_n = 20$ GPa, Coulomb friction coefficient $\mu = 0.3$. The tooth material has been assumed steel MET 91. Temperature dependent steel hardness and wear coefficient given in Sec. 6.6 have been used.

The thermal properties of rock (sandstone) and steel have been assumed, cf. Sec. 7.4:

- for rock
  heat capacity $c = 1970$ J/(kg·K),
  heat conductivity $\kappa = 5$ W/(m·K)

- for steel
  heat capacity c = 450 J/(kg·K),
  heat conductivity $\kappa = 60$ W/(m·K)

According to Eq. (7.3) the heat transfer coefficient representing heat conductance between rock particles is obtained as

$$h_{\text{cond}} = \kappa \frac{\bar{A}}{d} \approx \kappa \frac{r \cdot 1\text{m}}{2r} = \frac{\kappa}{2} \text{ [W/K]} \tag{11.1}$$

Thus we have

- for rock: $h_{\text{cond}} = 2.5$ W/K
- for steel: $h_{\text{cond}} = 30$ W/K

Thermo-mechanical numerical simulation of wear of a ripper tooth has been preceded by the determination of temperature distribution in the tooth. Two methods has been used:

1. transient thermal analysis for sufficiently long time,
2. quasi-stationary solution of thermal process using average heat generation rate during one tooth pass as thermal load.

11.2 Transient thermo-mechanical solution without wear

It is assumed that in the process of rock cutting we have initially a transient process of heat generation and conduction, when the temperature of the tooth rises until a certain quasi-stationary state of heat conduction is reached. In this state we have equilibrium between the heat generated and absorbed by the tooth and heat convected to the contacting rock and environment.

Because the process of rock cutting is characterized by relatively long work distances it can be assumed that most of the work of a ripper is carried out under quasi-stationary thermal conditions. This is the period most important for the wear of the tooth. Following this assumption we analyzed transient thermo-mechanical process of rock cutting with a ripper without considering wear.

Cutting has been carried out with prescribed horizontal velocity of the tool 4, 0.4 and 0.04 m/s. Temperature distribution at different instants for cutting with velocity 4 m/s is shown in Fig. 11.1, for velocity 0.4 m/s – in Fig. 11.2, and for velocity 0.04 m/s – in Fig. 11.3.

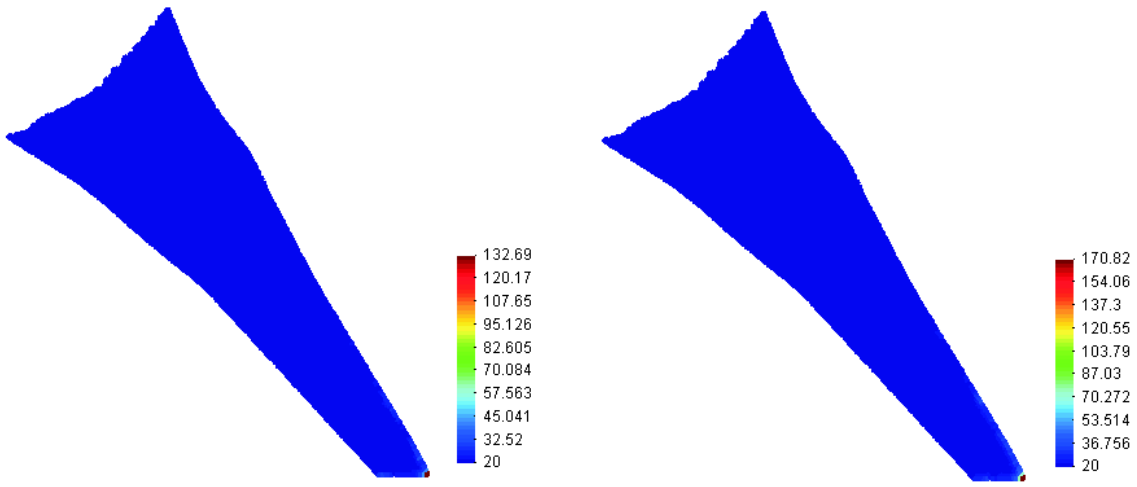

a) after pass 3 b) after pass 4

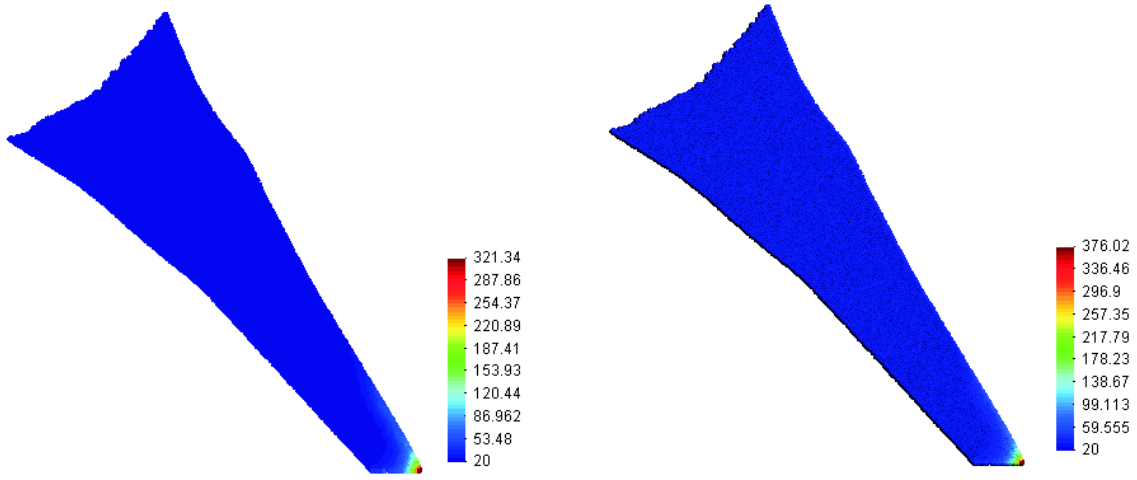

c) after pass 21 d) after pass 22

Figure 11.1: Thermo-mechanical transient simulation of rock cutting with a ripper – temperature distribution at different instants of cutting with velocity 4 m/s

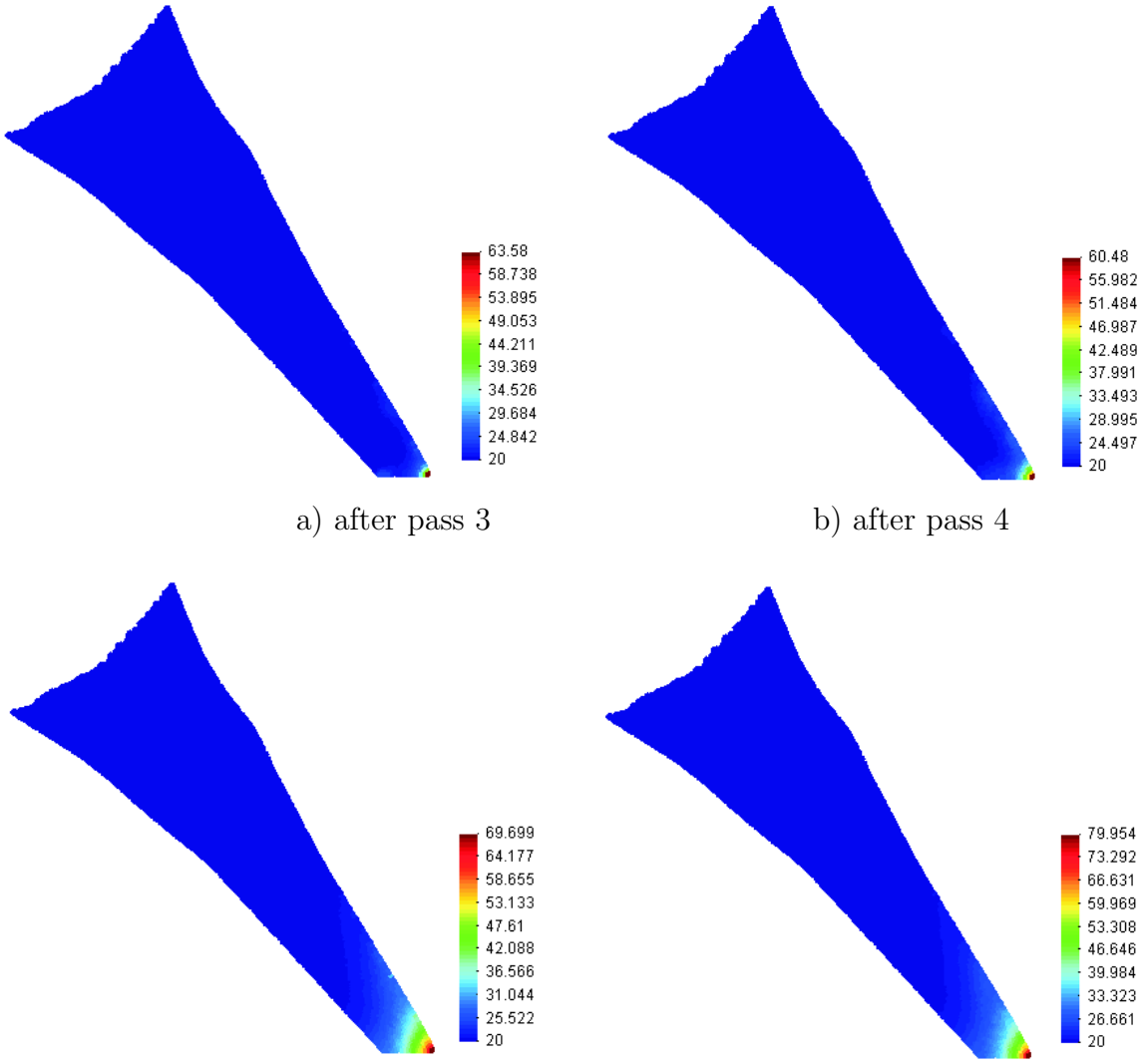

a) after pass 3 b) after pass 4

c) after pass 13 d) after pass 14

Figure 11.2: Thermo-mechanical transient simulation of rock cutting with a ripper – temperature distribution at different instants of cutting with velocity 0.4 m/s

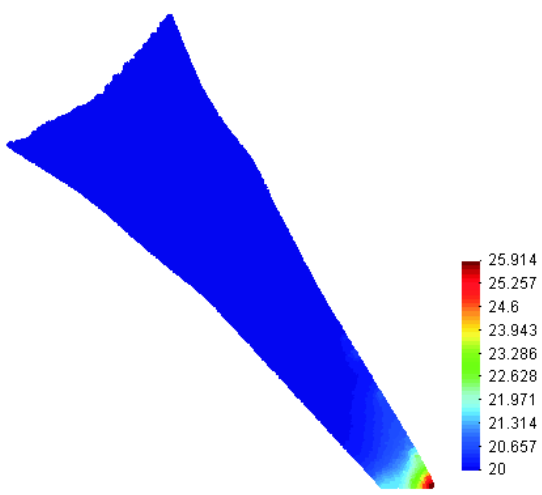

a) after pass 3

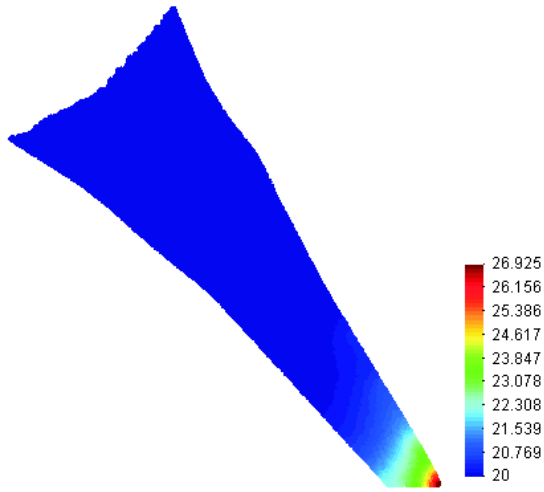

b) after pass 4

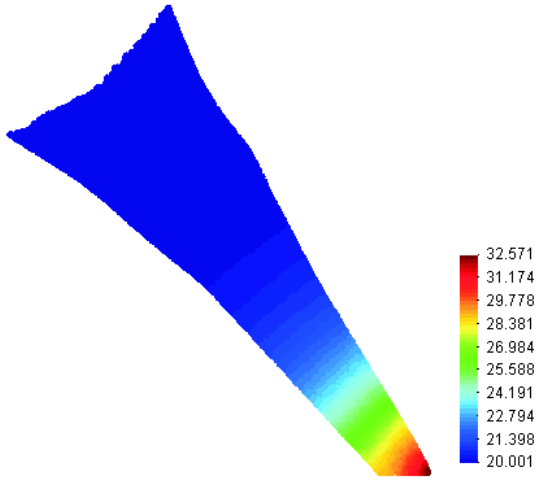

c) after pass 17

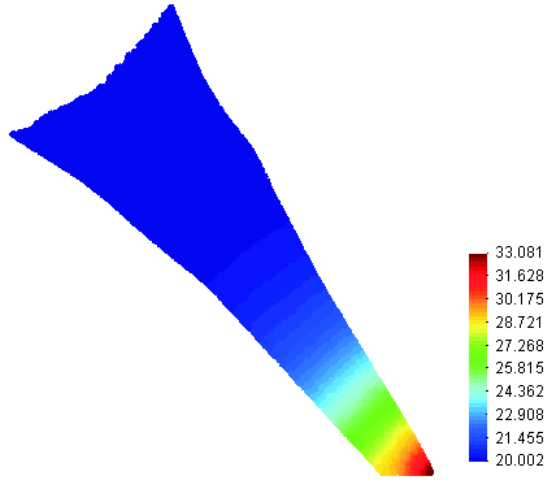

d) after pass 18

Figure 11.3: Thermo-mechanical transient simulation of rock cutting with a ripper – temperature distribution at different instants of cutting with velocity 0.04 m/s

11.3 Quasi-stationary solution of thermal problem

Assuming that we have reached the steady state of heat transfer temperature distribution can be obtained employing a quasi-stationary solution of thermal problem. As the thermal load the average heat generation rate on the tooth surface obtained from transient analysis is taken. Different cutting velocities and different boundary conditions along the tooth cross-section have been considered. Temperature distributions obtained for different cases are shown in Fig. 11.4.

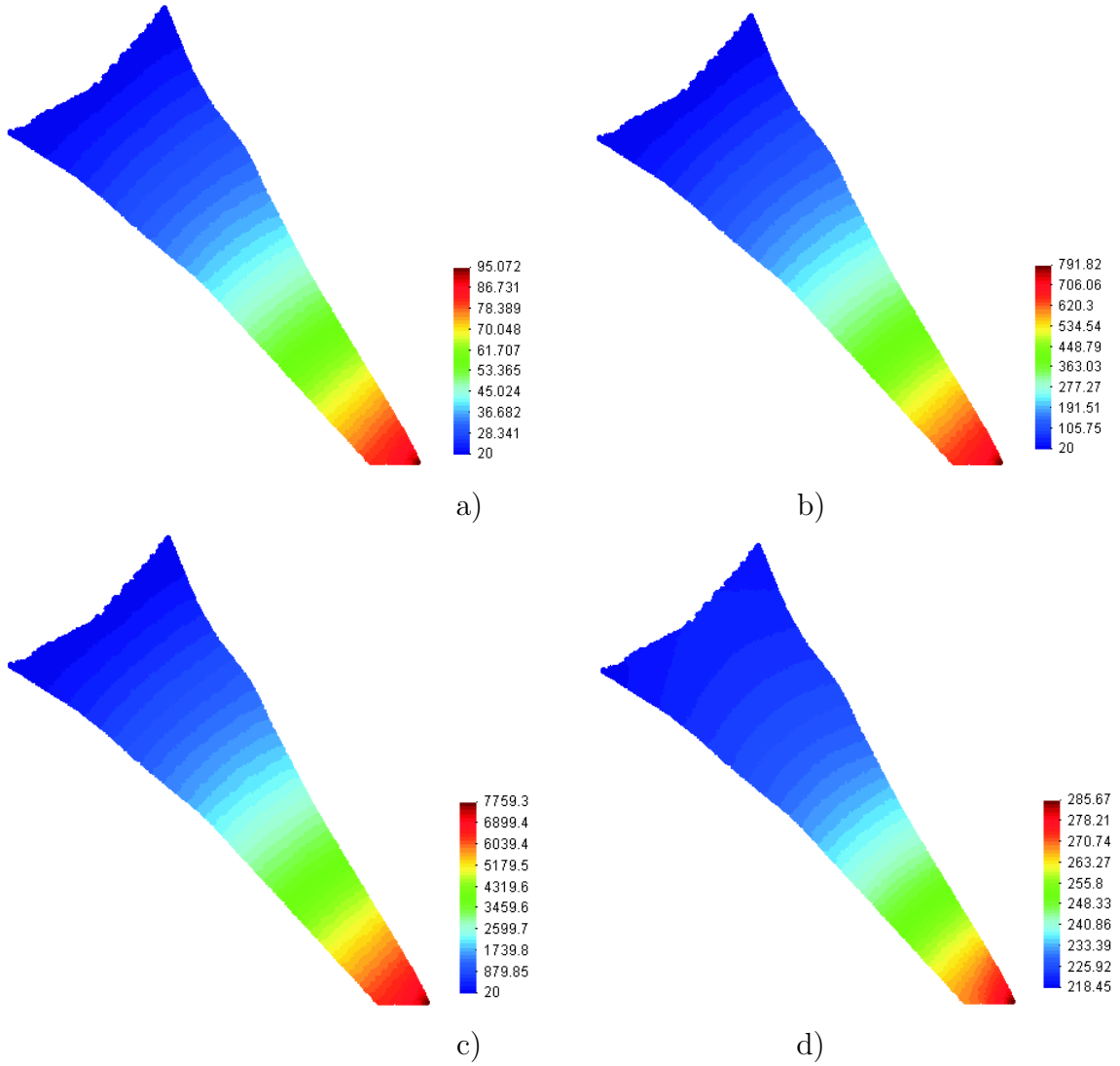

Figure 11.4: Quasi-stationary thermal analysis – temperature distribution for different boundary conditions at the tooth cross-section, and cutting velocity; a) $v = 0.04$ m/s, b) $v = 0.4$ m/s, c,d) $v = 0.04$ m/s; a,b,c) prescribed temperature 20°C, d) insulation

11.4 Thermomechanical simulation of rock cutting with wear evaluation

11.4.1 Model I – initial temperature distribution from transient thermal analysis

Wear analysis has been carried out starting with initial temperature distribution determined through transient thermal analysis discussed in Sec. 11.2. Cutting velocity 0.4 m/s has been assumed – corresponding temperature distribution is shown in Fig. 11.2d). Wear has been accelerated as accelerating wear 7000 times.

Tooth shape and temperature distribution for different stages of wear are shown in Fig. 11.5.

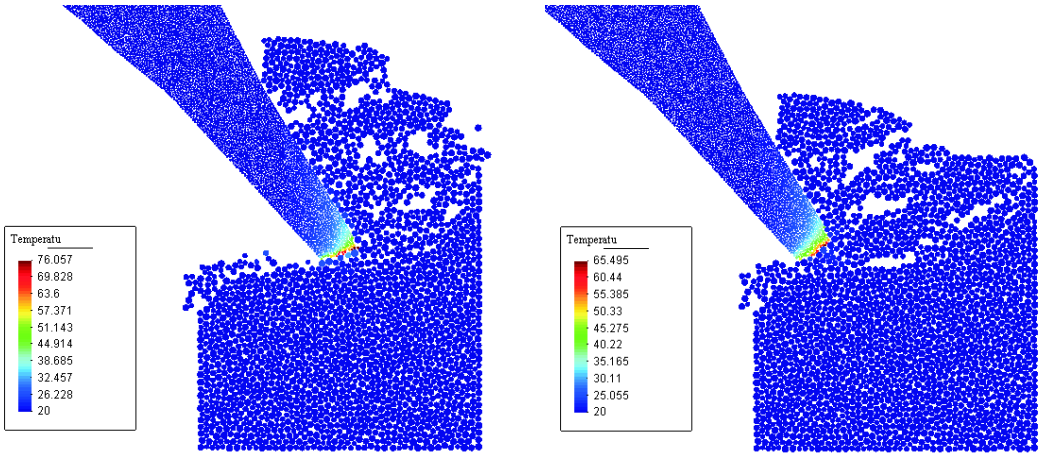

a) t = 5 s b) t = 15 s

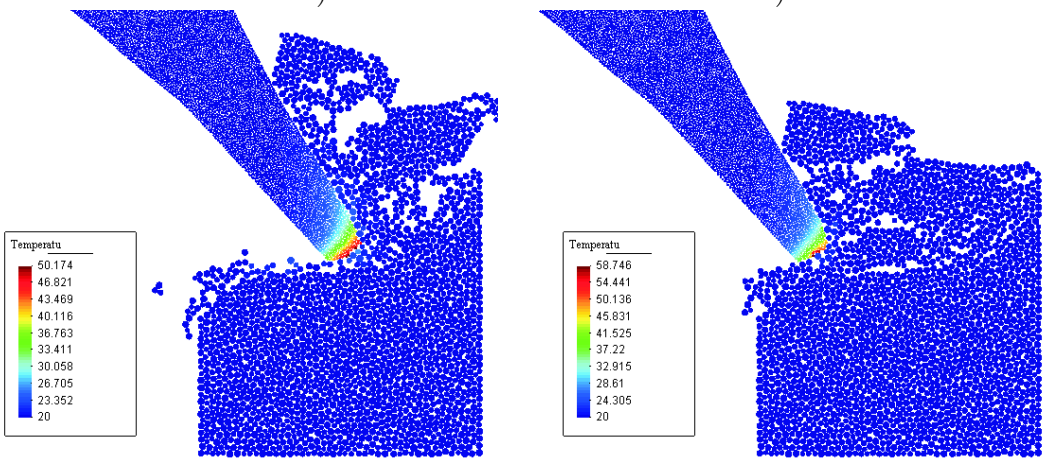

c) t = 90 s d) t = 100 s

Figure 11.5: Process of cutting — tool shape evolution and temperature distribution in the tool (model II)

11.4.2 Model II – initial temperature distribution from quasi-stationary thermal analysis

Wear analysis has been carried out starting with initial temperature distribution determined through quasi-stationary thermal analysis discussed in Sec. 11.3. Cutting velocity 0.4 m/s has been assumed and insulation at the tooth-crossection – corresponding initial temperature distribution is shown in Fig. 11.4d). Wear has been accelerated as accelerating wear 7000 times.

Tooth shape and temperature distribution for different stages of wear are shown in Fig. 11.6.

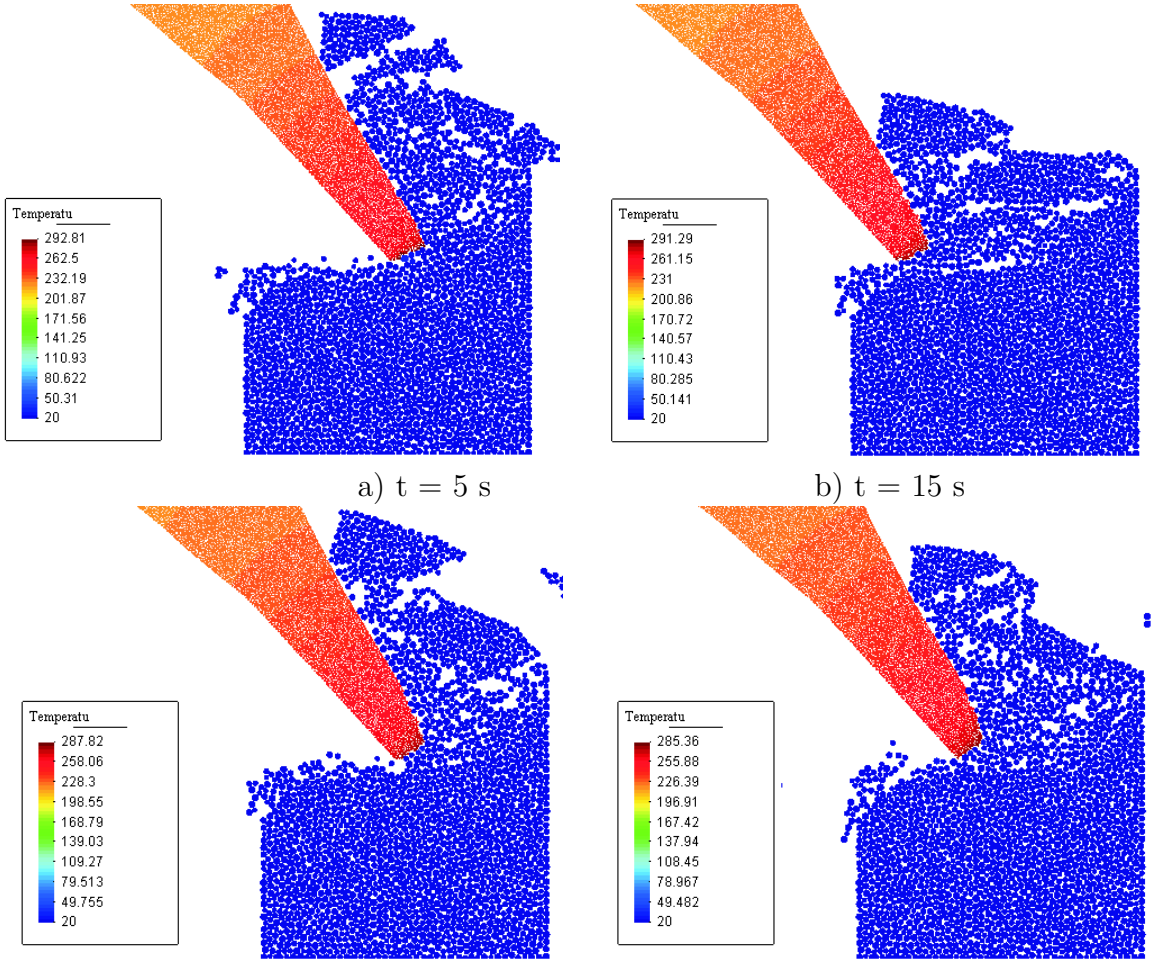

Figure 11.6: Process of cutting — tool shape evolution and temperature distribution in the tool (model I)

Chapter 12

Simulation of dredging

12.1 Model I

12.1.1 Model definition

Numerical simulation of dredging with wear of a dredge tooth has been carried out using a 2D model shown in Fig. 12.1. Material sample is represented by an assembly of randomly compacted 92000 discs of radii 1–1.5 mm. Model parameters obtained previously for sandstone are assumed for the micromechanical model.

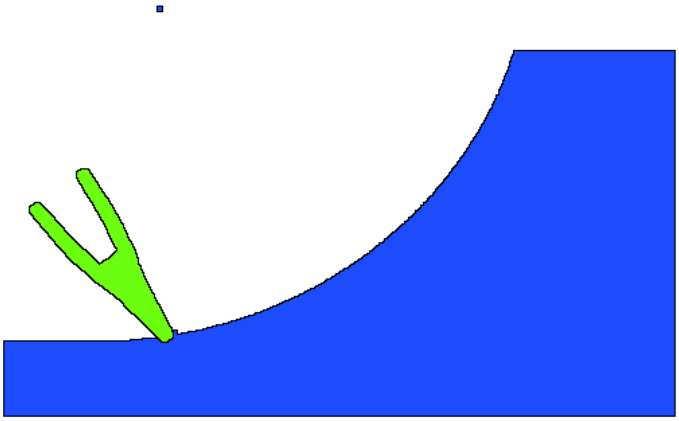

Figure 12.1: 2D model of dredging – initial set-up

The rigid tool is modelled with distinct elements, 5400 discs of equal radius of 1 mm. The following parameters have been assumed for the tool-rock interface: contact stiffness modulus $k_n = 50$ GPa, Coulomb friction coefficient $\mu = 0.4$. The tooth material has been assumed steel MET 91. Wear analysis has been carried out with temperature dependent hardness and wear coefficient estimated in Sec. 6.6. The

simulation has been carried out using the constant tooth hardness. Wear has been accelerated 7000 times by scaling the wear coefficient k.

The swing velocity was assumed 0.2 m/s, and rotating velocity 1.6204 s^{-1}, which with the distance of the tooth from the axis of rotation 0.7 m gives circumferential velocity 1.134 m/s. Mechanical process has been scaled 5 times.

12.1.2 Thermo-mechanical analysis of dredging

Process of dredging has been analysed as thermo-mechanical process with subsequent cutting and cooling. During cutting the tooth was heated and then during the rotation in water the tooth was cooled. The tooth surface was cooled by water during cutting as well. The heat diffusion through the tooth material was analysed. Analysis presented in this section has been carried out with an unchanged tooth shape (zero wear).

Analysis results are shown in Figs. 12.2–12.5. Failure of rock during dredging is shown in Fig. 12.2. Temperature distribution at different instants of the first tooth pass of cutting is shown in Fig. 12.3 and temperature distribution during cooling with water is presented in Fig. 12.4. Cyclic thermal load is illustrated by the curve representing change of maximum tooth temperature during subsequent cutting and cooling (Fig. 12.5).

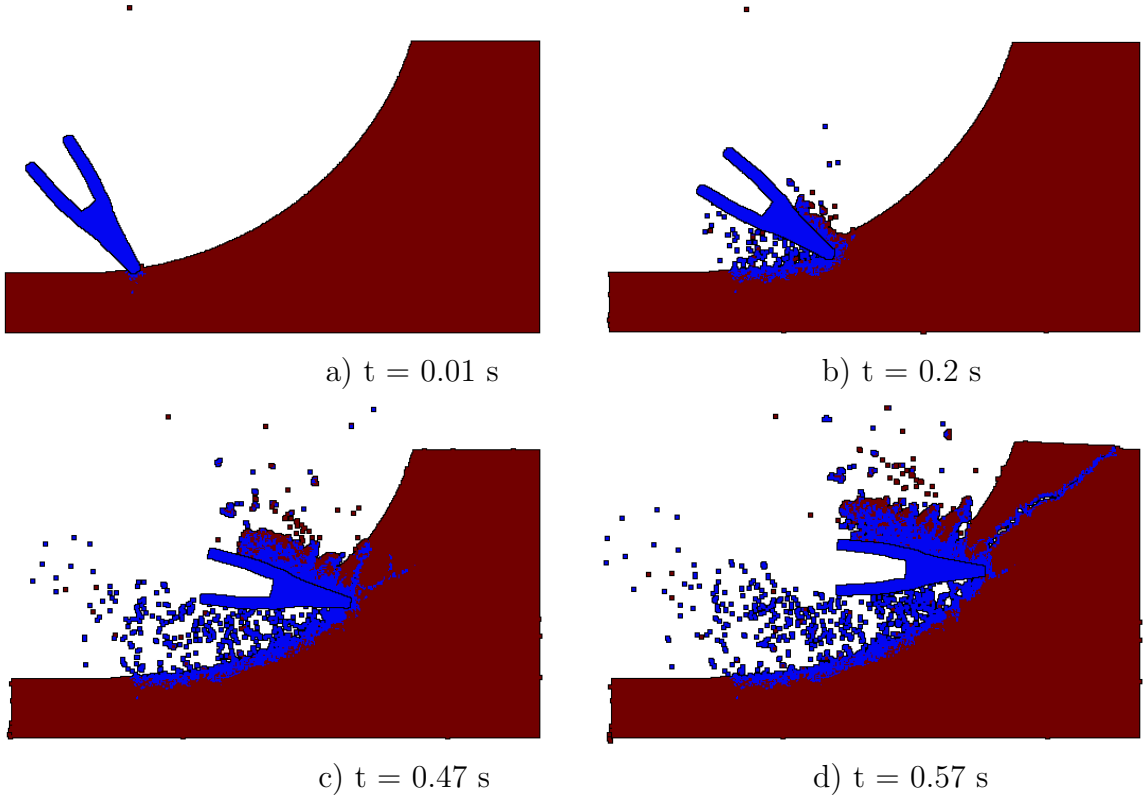

a) t = 0.01 s

b) t = 0.2 s

c) t = 0.47 s

d) t = 0.57 s

Figure 12.2: Thermo-mechanical simulation of dredging – failure mode

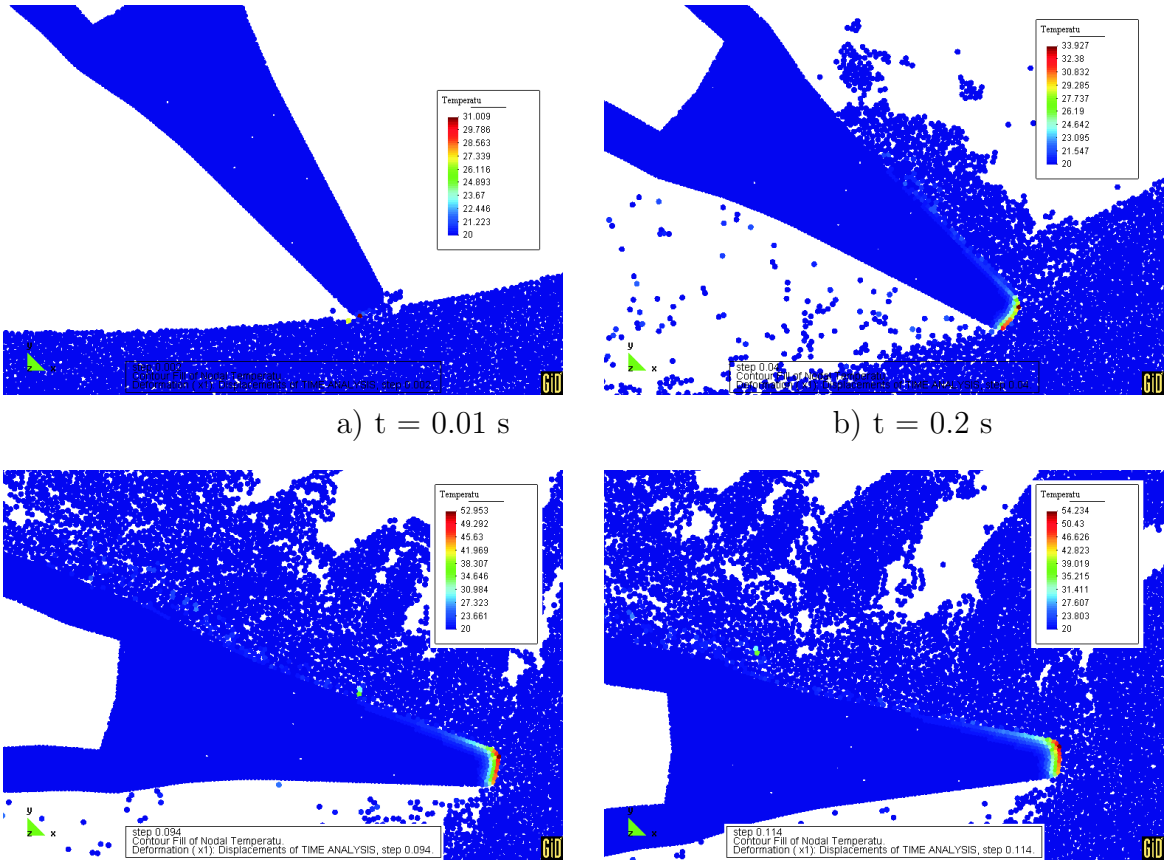

a) t = 0.01 s b) t = 0.2 s

c) t = 0.47 s d) t = 0.57 s

Figure 12.3: Thermo-mechanical simulation of dredging – temperature distribution at different instants of the first tooth pass of cutting

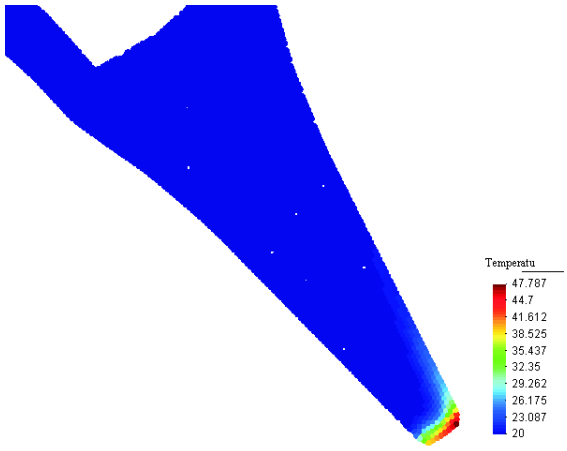

a) t = 0.63 s

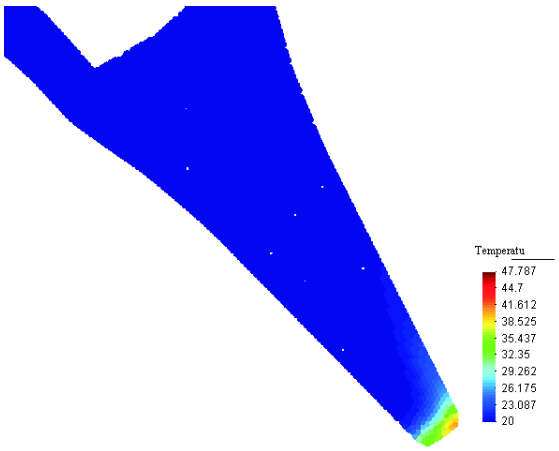

b) t = 0.93 s

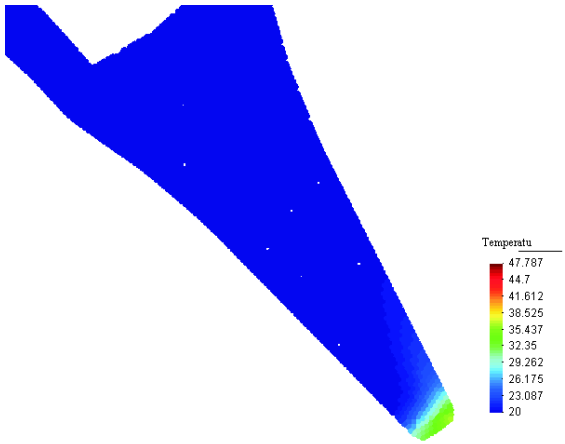

c) t = 1.23 s

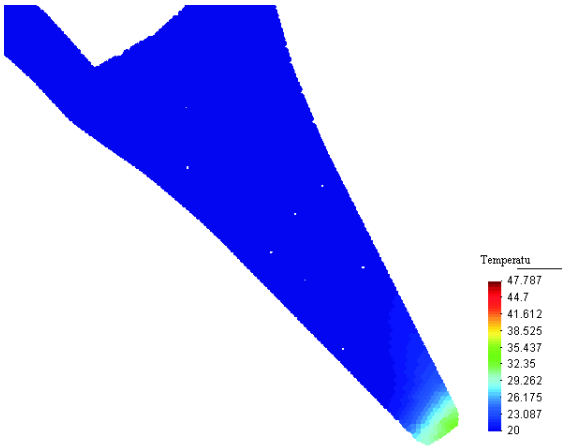

d) t = 1.83 s

Figure 12.4: Thermo-mechanical simulation of dredging – temperature distribution at different instants of cooling after the first tooth pass of cutting

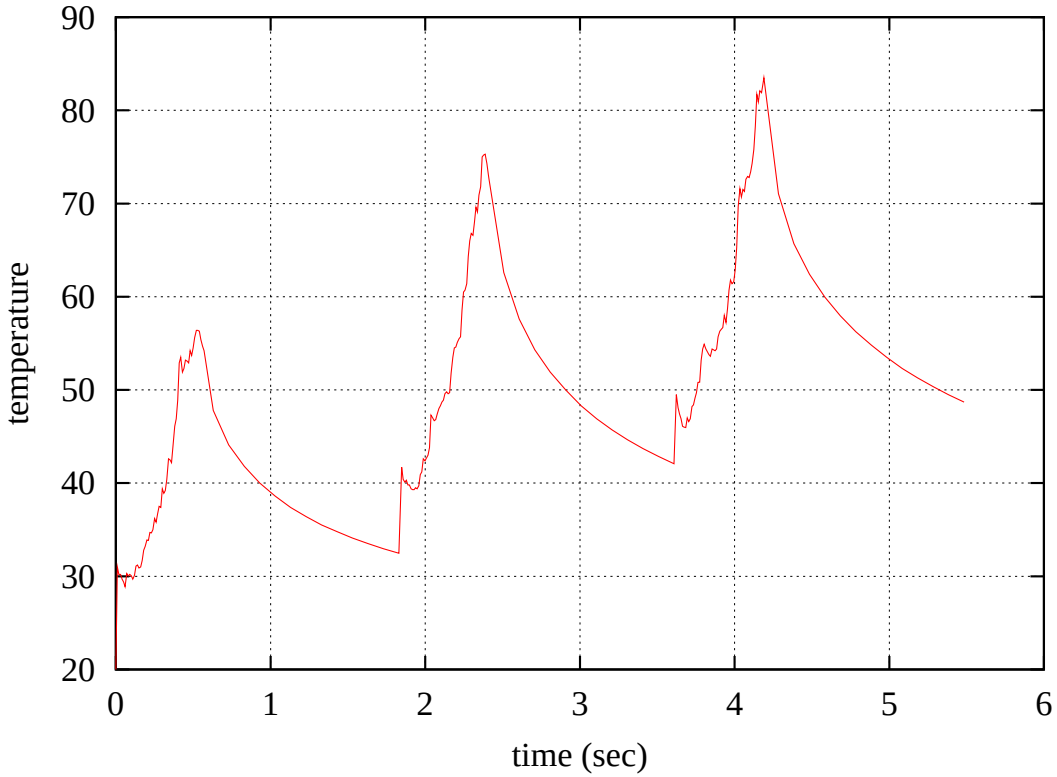

Figure 12.5: Thermo-mechanical simulation of dredging – variation of maximum tooth temperature during three cycles of cutting and subsequent cooling

12.1.3 Thermo-mechanical analysis of dredging with wear evaluation

Similar thermo-mechanical analysis of dredging has been carried out with extension to wear evaluation and modification of the tooth shape due to wear.

Analysis results are shown in Figs. 12.6–12.12. Failure of rock during dredging is shown in Fig. 12.6. Temperature distribution at different instants of the first tooth pass of cutting is shown in Fig. 12.7 and temperature distribution during cooling with water is presented in Fig. 12.8. Cyclic thermal load is illustrated by the curve representing change of maximum tooth temperature during subsequent cutting and cooling (Fig. 12.9). Figure 12.10 shows accumulated wear on the tooth surface at different instants of the first tooth pass of cutting. Evolution of tooth shape due to wear is shown in Fig. 12.11. Wear is quantified by the curve showing the tooth mass loss in Fig. 12.12.

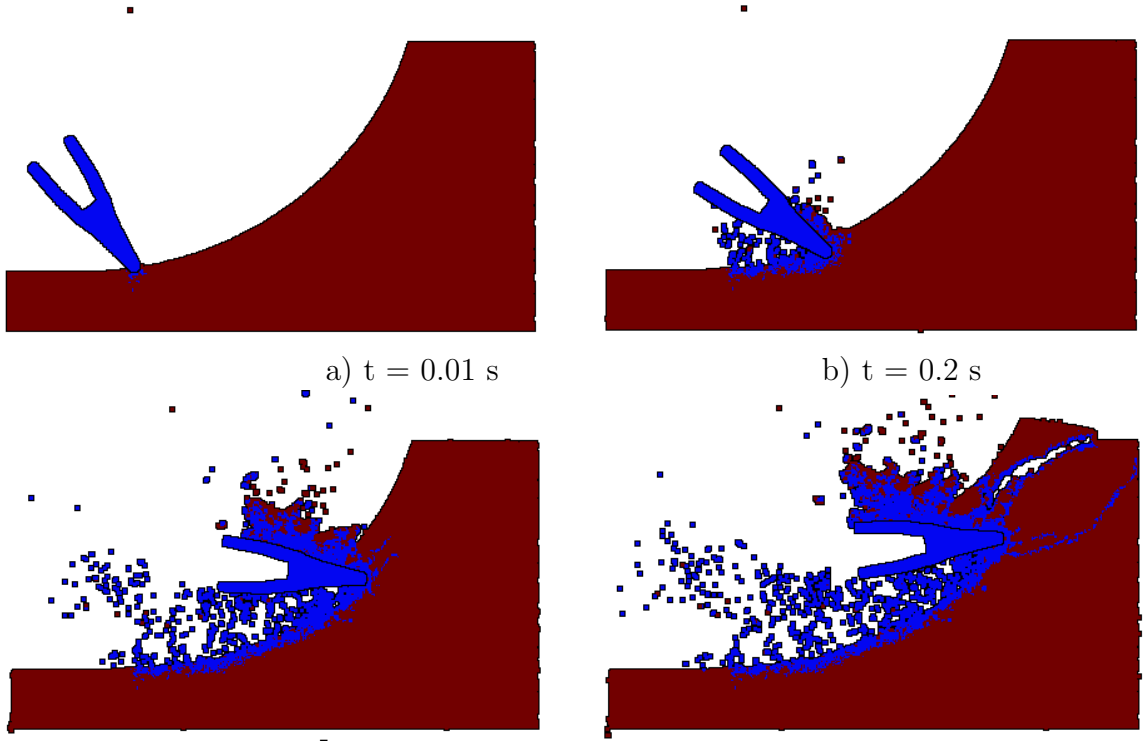

a) t = 0.01 s b) t = 0.2 s

c) t = 0.52 s d) t = 0.64 s

Figure 12.6: Thermo-mechanical simulation of dredging with wear evaluation – failure mode

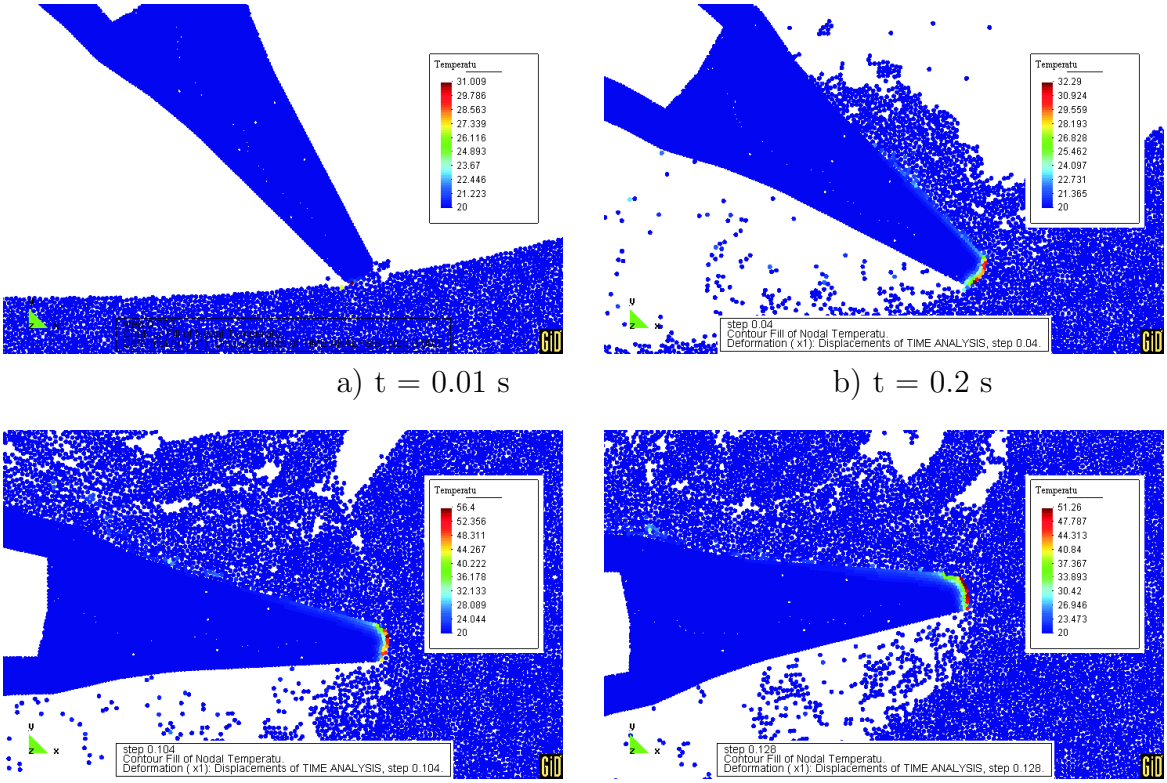

a) t = 0.01 s b) t = 0.2 s

c) t = 0.52 s d) t = 0.64 s

Figure 12.7: Thermo-mechanical simulation of dredging with wear evaluation – temperature distribution at different instants of the first tooth pass of cutting

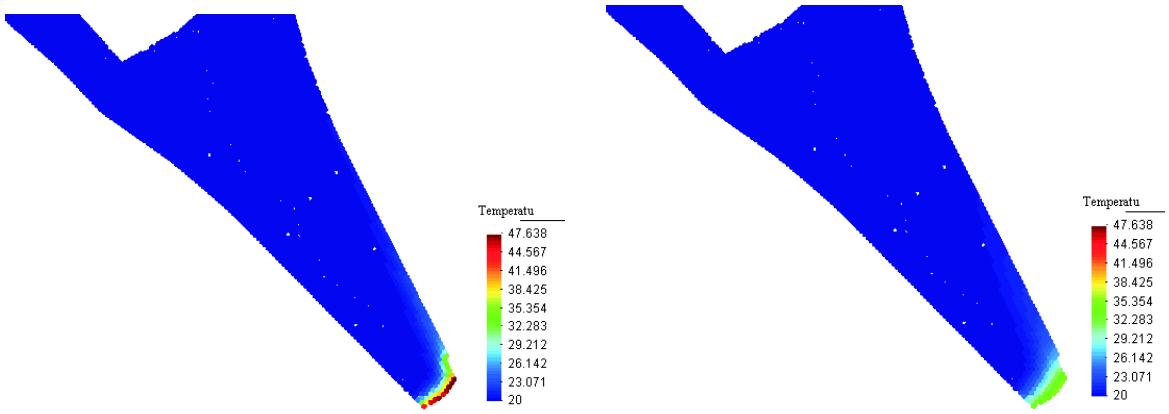

a) t = 0.68 s

b) t = 1.08 s

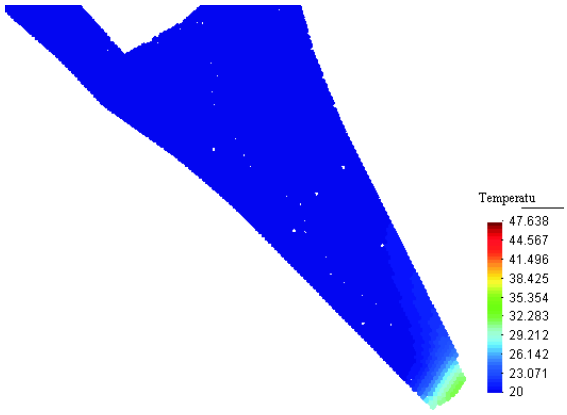

c) t = 1.48 s

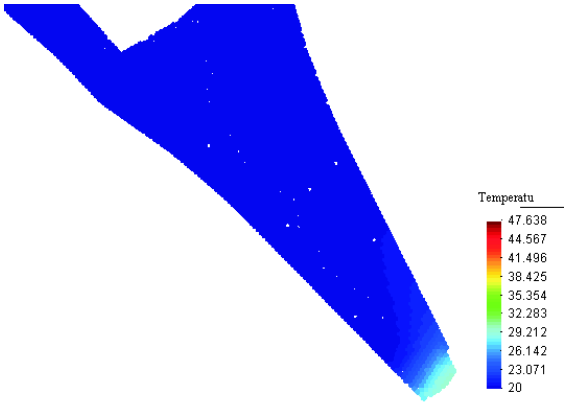

d) t = 2.00 s

Figure 12.8: Thermo-mechanical simulation of dredging with wear evaluation – temperature distribution at different instants of cooling after the first tooth pass of cutting

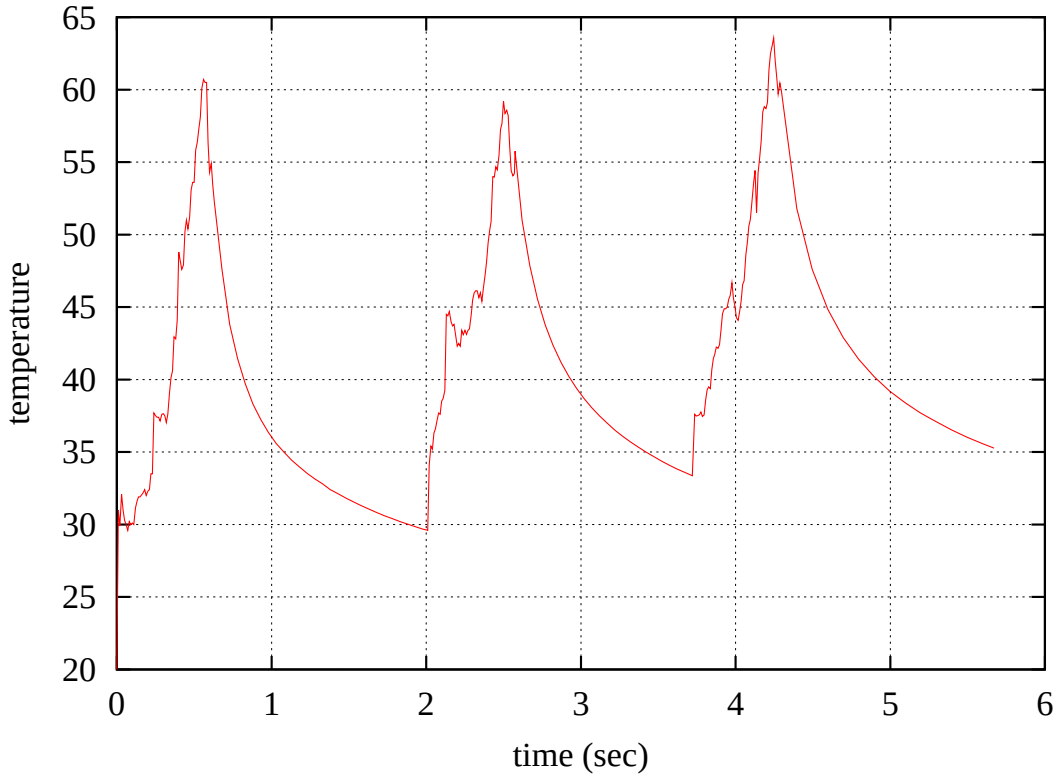

Figure 12.9: Simulation of dredging – variation of maximum tooth temperature during three cycles of cutting and subsequent cooling

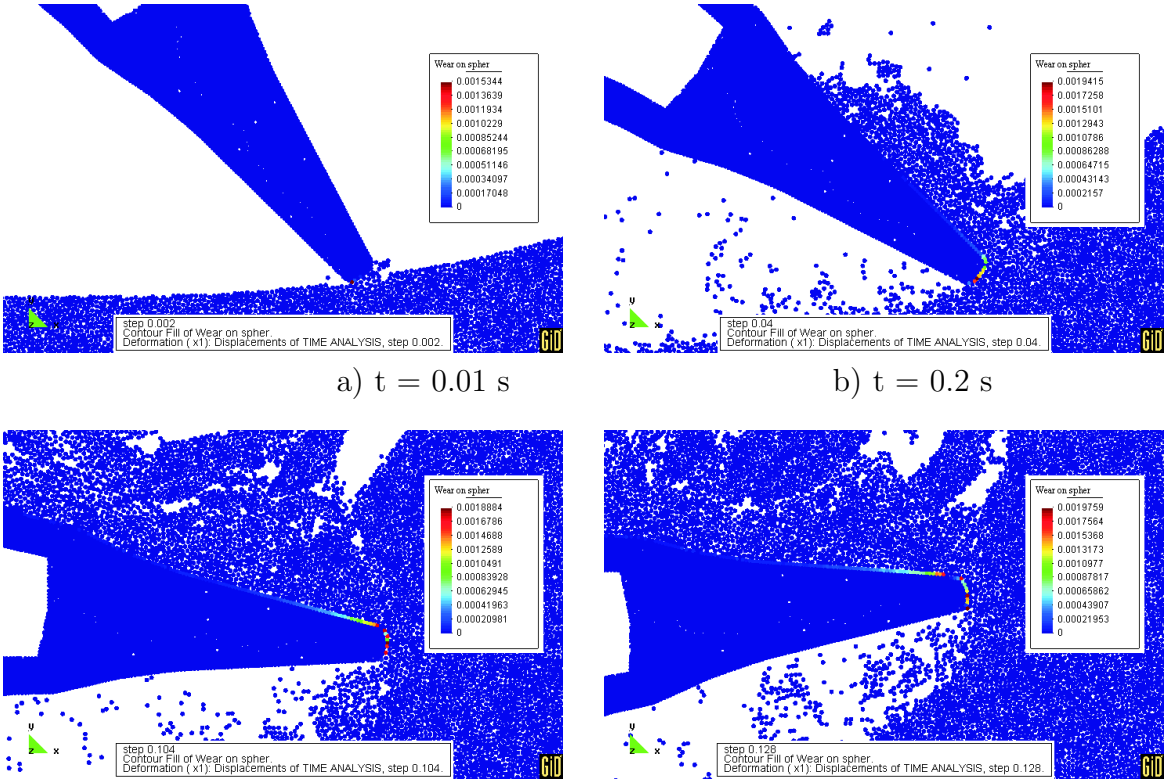

a) t = 0.01 s b) t = 0.2 s

c) t = 0.52 s d) t = 0.64 s

Figure 12.10: Thermo-mechanical simulation of dredging with wear evaluation – accumulated wear on the tooth surface at different instants of the first tooth pass of cutting

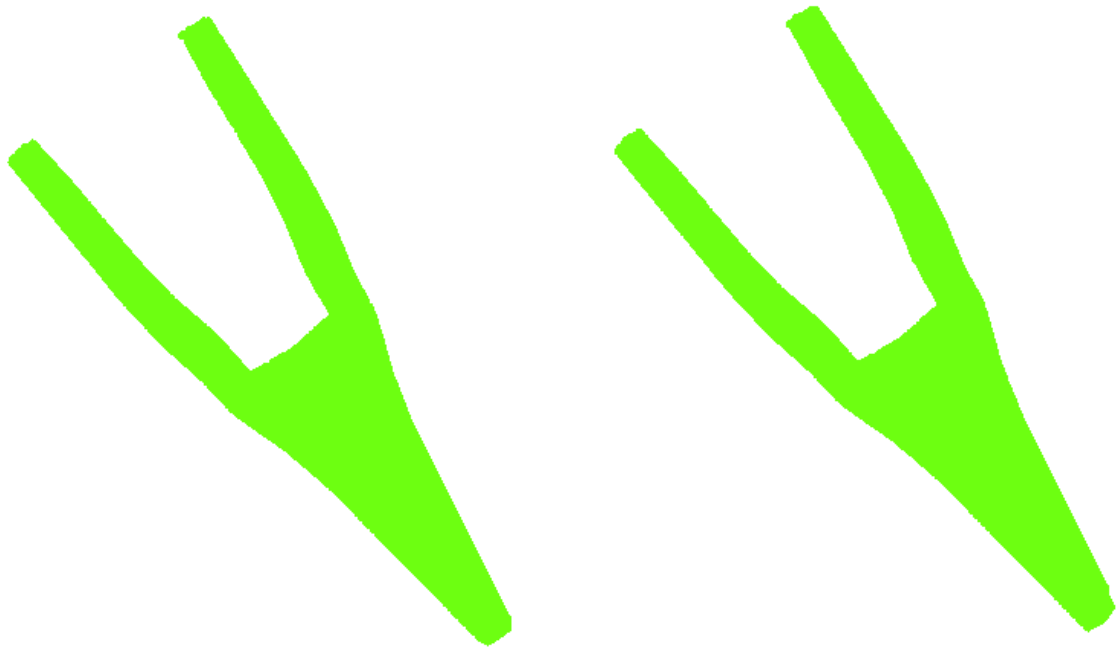

a) before 1st pass

b) after 1st pass

c) after 2nd pass

d) after 3rd pass

Figure 12.11: Thermo-mechanical simulation of dredging with wear evaluation – evolution of tooth shape due to wear

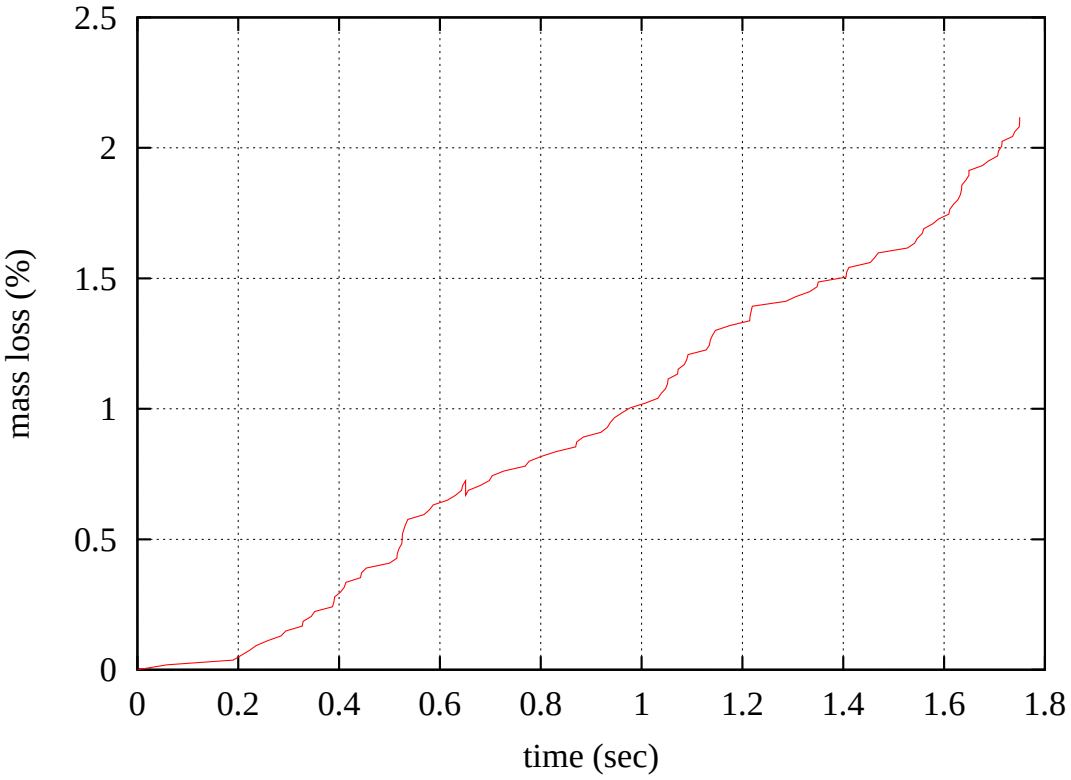

Figure 12.12: Simulation of dredging – tooth mass loss during 3 cycles analysed

12.2 Model II

12.2.1 Model definition

Numerical simulation of dredging with wear of a dredge tooth has been carried out using a 2D model shown in Fig. 12.13. This model has slightly modified initial tooth geometry.

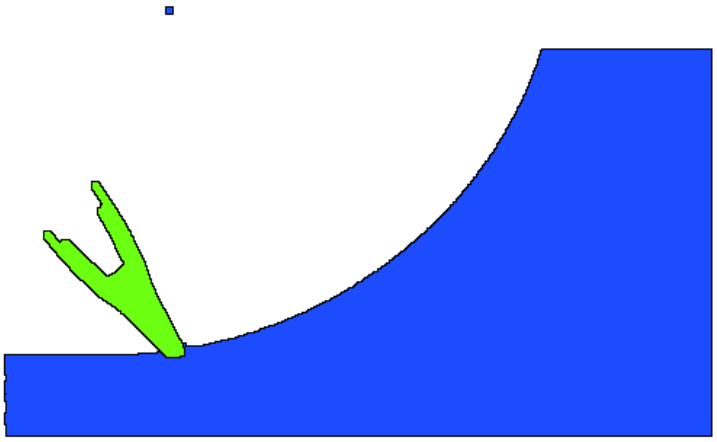

Figure 12.13: 2D model of dredging – initial set-up

Material sample is the same as in Model I. The rigid tool is modelled with distinct elements, 9400 discs of equal radius of 0.7 mm. The parameters for the tool-rock interface have been assumed the same as in Model I. The tooth material has been assumed steel MET 91 with wear coefficient k and temperature dependent hardness $H = H(T)$ given in Sec. 6.6. Wear has been accelerated 7000 times, which was obtained by scaling adequately coefficient k.

The same cutting velocities as previously have been assumed. Similarly mechanical process has been scaled 5 times.

12.2.2 Thermo-mechanical analysis of dredging with wear evaluation

Process of dredging has been analysed as thermo-mechanical process with subsequent cutting and cooling. During cutting the tooth was heated and then during the rotation in water the tooth was cooled. The tooth surface was cooled by water during cutting as well. The heat diffusion through the tooth material was analysed. The tool shape was modified due to wear.

Analysis results are shown in Figs. 12.14–12.18. Failure of rock during dredging is shown in Fig. 12.14. Temperature distribution at different instants of the first tooth

pass is shown in Fig. 12.15 and temperature distribution during cooling with water is presented in Fig. 12.16. Figure 12.17 shows accumulated wear on the tooth surface at different instants of the first tooth pass of cutting. Change of the tooth shape due to wear after one pass of cutting is shown in Fig. 12.18.

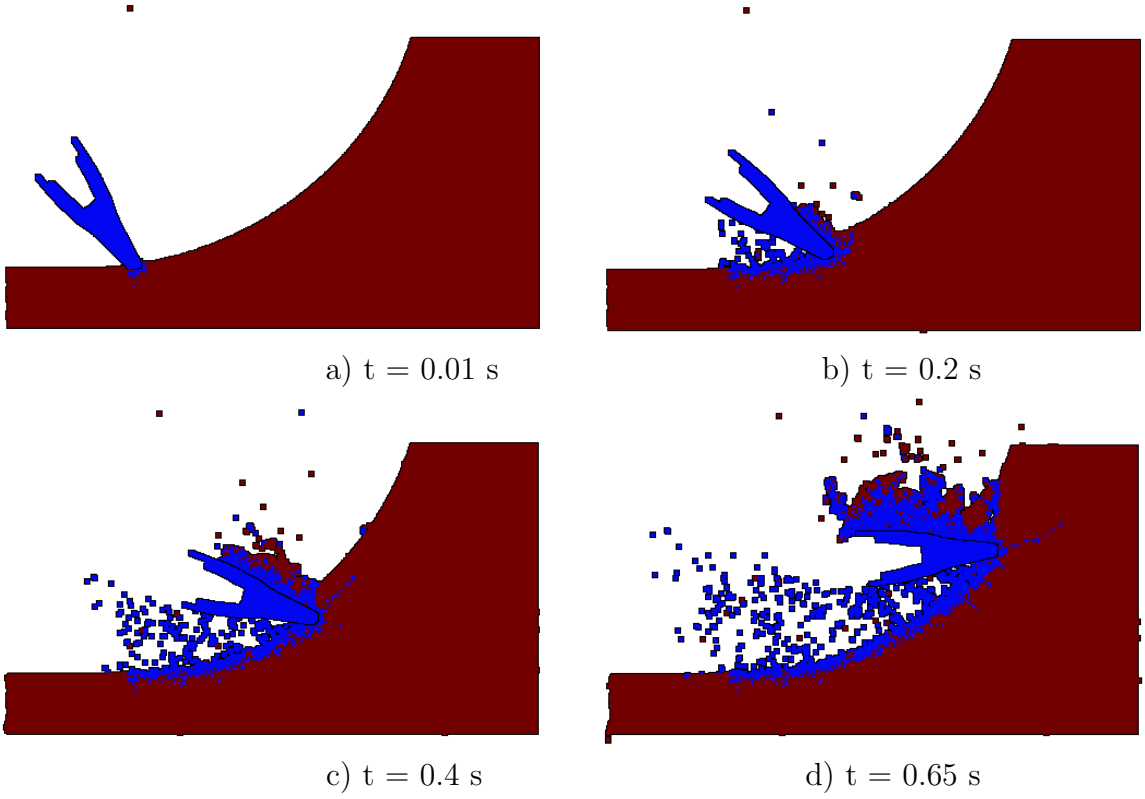

a) t = 0.01 s b) t = 0.2 s

c) t = 0.4 s d) t = 0.65 s

Figure 12.14: Thermo-mechanical simulation of dredging with wear evaluation – failure mode (model II)

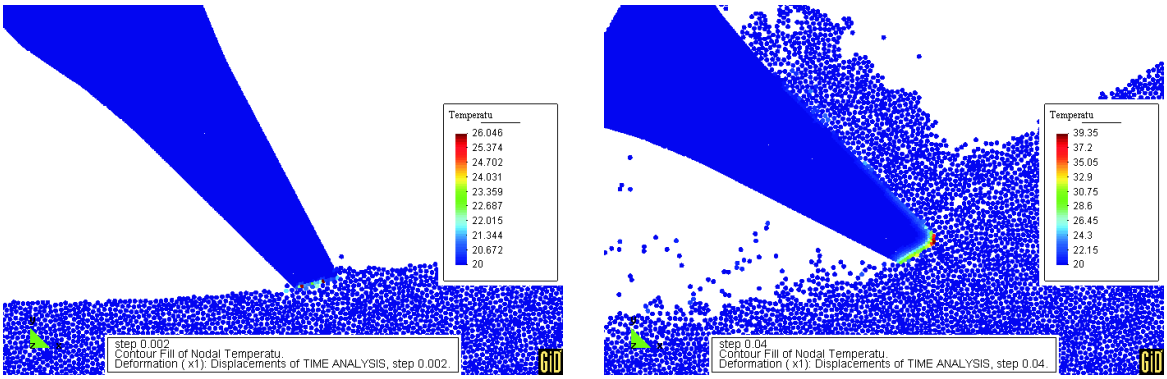

a) t = 0.01 s b) t = 0.2 s

c) t = 0.4 s d) t = 0.65 s

Figure 12.15: Thermo-mechanical simulation of dredging with wear evaluation – temperature distribution at different instants of the first tooth pass of cutting (model II)

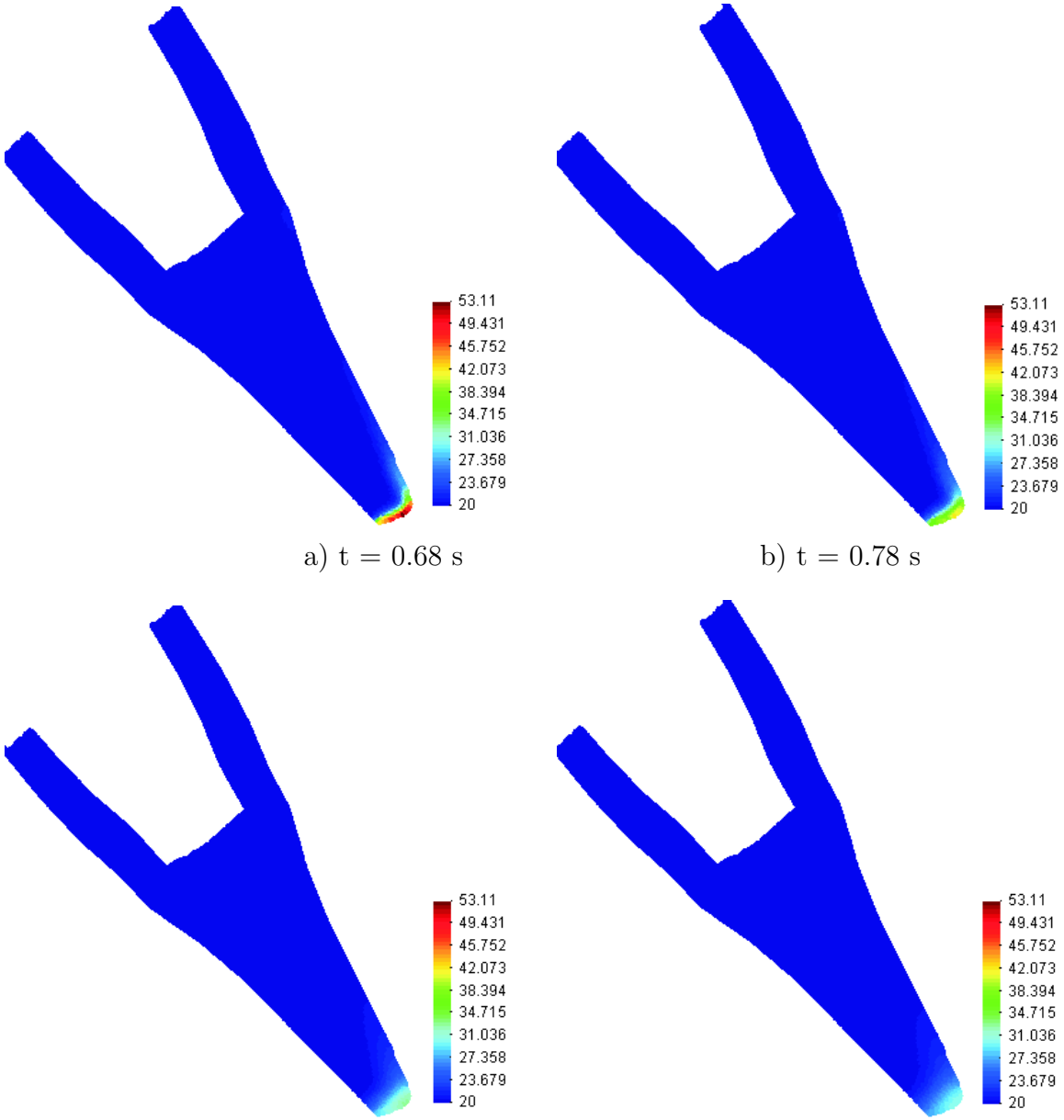

a) t = 0.68 s b) t = 0.78 s

c) t = 1.48 s d) t = 2.00 s

Figure 12.16: Thermo-mechanical simulation of dredging with wear evaluation – temperature distribution at different instants of cooling after the first tooth pass of cutting (model II)

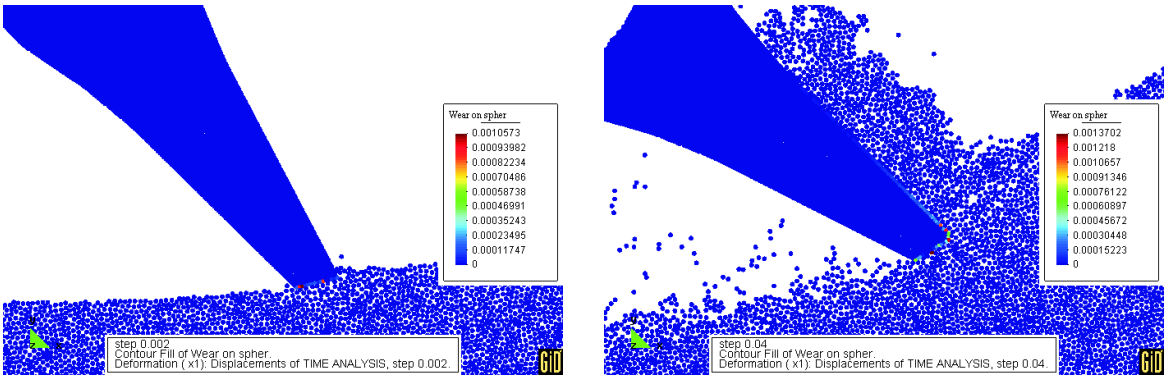

a) t = 0.01 s b) t = 0.2 s

c) t = 0.4 s d) t = 0.65 s

Figure 12.17: Thermo-mechanical simulation of dredging with wear evaluation – accumulated wear on the tooth surface at different instants of the first tooth pass of cutting (model II)

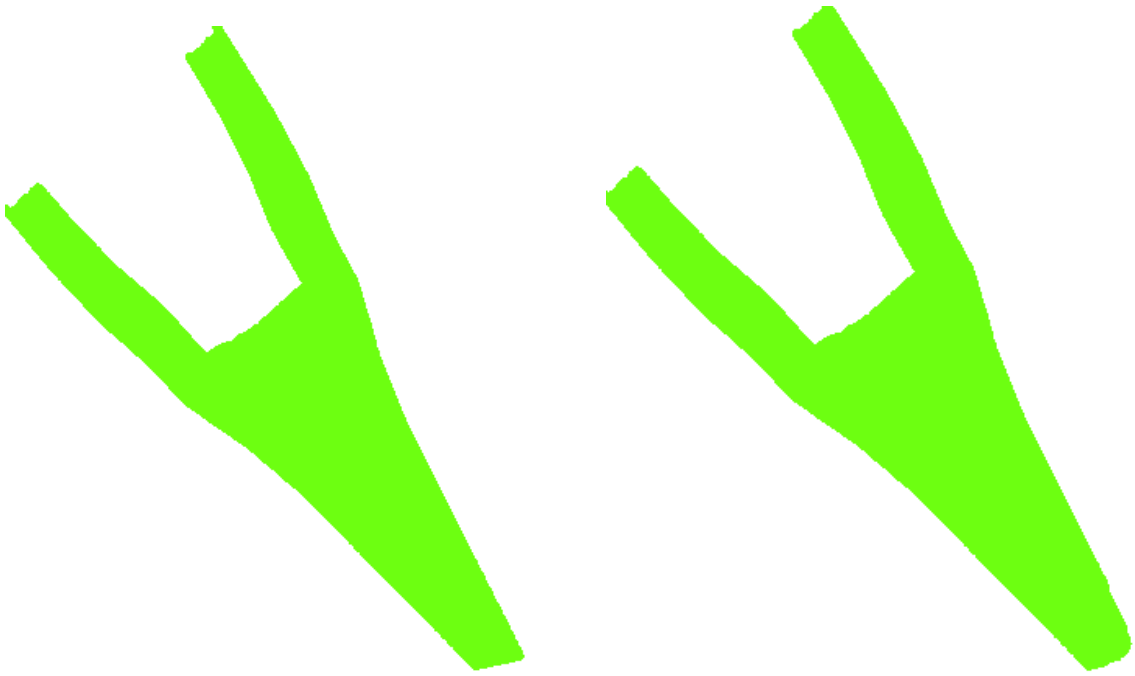

a) before 1st pass b) after 1st pass

Figure 12.18: Thermo-mechanical simulation of dredging with wear evaluation – evolution of tooth shape due to wear (model II)

Chapter 13

3D simulation of rock cutting

13.1 3D simulation of interaction of a tooth with granular medium

3D simulation of interaction of a tooth with granular medium has been carried out using a model shown in Fig. 13.1a. Material is represented by a collection of 11700 spherical particles of radii 9 mm placed randomly in a rectangular box (not presented in figure) and subjected to gravitational loading. The surface of the rigid tool has been modelled with triangular facets. In the contact among particles the following properties have been assumed: contact stiffness in the normal direction $k_n = 10^6$ N/m, friction coefficient $\mu = 0.1$, no cohesion existed among particles. Friction between the tooth and material particles was defined by the Coulomb friction coefficient $\mu = 0.1$, no wear calculation has been done. The tooth has been lowered, and after penetration the horizontal velocity 0.04 m/s has been prescribed. Interaction of the tooth with material particles is shown in Fig. 13.1b.

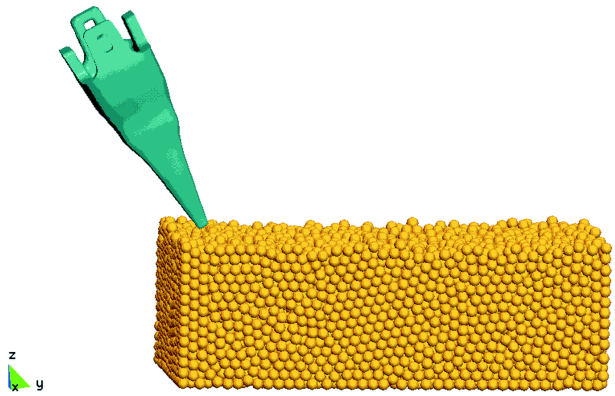

a) t = 0.0 s

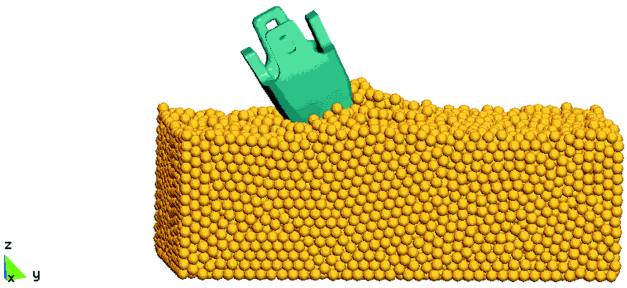

b) t = 1.1 s

Figure 13.1: 3D simulation of interaction of a tooth with granular medium

13.2 3D simulation of rock cutting (model I)

The same as above initial geometry of the tooth and particles (Fig. 13.2a) has been used to create a 3D model of rock cutting. Rock-like material properties have been obtained by introduction of cohesive bonds among contacting particles. The contact interface properties were as follows: contact stiffness in the normal and tangential directions $k_n = k_T = 10^6$ N/m, cohesive bond strengths $R_n = 500$ N/m, $R_T = 5000$ N/m, friction coefficient $\mu = 0.5$. Friction between the tooth and material particles was defined by the Coulomb friction coefficient $\mu = 0.1$, no wear calculation has been done. The process of cutting has been defined similarly as previously, the tooth has been lowered, and after penetration the horizontal velocity 0.04 m/s has been prescribed. Interaction of the tooth with material particles is shown in Fig. 13.2b. Formation of a chip can be seen in this figure.

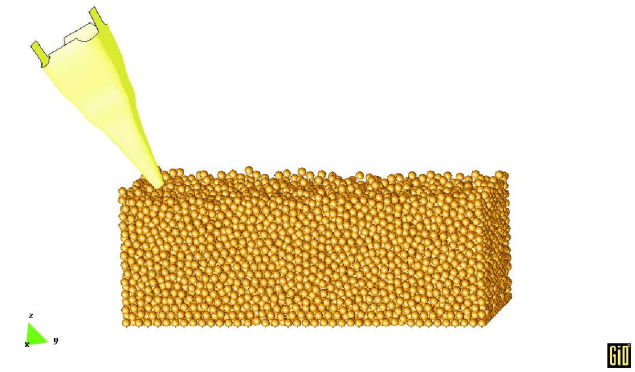

a) t = 0.0 s

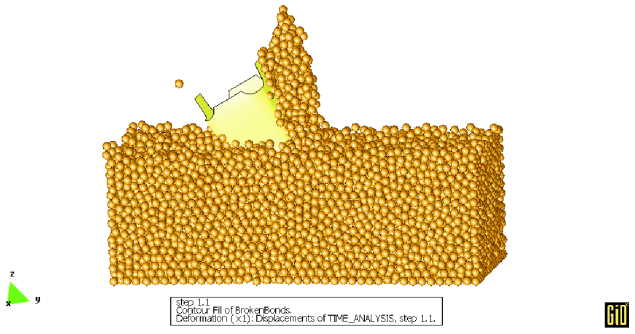

b) t = 1.1 s

Figure 13.2: 3D simulation of rock cutting (model I)

13.3 3D simulation of rock cutting (model II)

The same as above model of rock sample (Fig. 13.3a) has been used. The same contact interface properties were assumed: contact stiffness in the normal and tangential directions $k_n = k_T = 10^6$ N/m, cohesive bond strengths $R_n = 500$ N/m, $R_T = 5000$ N/m, friction coefficient $\mu = 0.5$. The tool model in the present model has been composed of two rigid parts, one part has been modelled with rigid surfaces and the other one has been discretized with 28570 distinct elements of radii 1.5 mm (considerably smaller than the radius of rock particles, 9 mm). The small radius of particles discretizing the tool allows us to assume that the interaction of rock particles is similar like interaction with flat surface. Friction between the tooth and material particles was defined by the Coulomb friction coefficient $\mu = 0.1$.

The process of cutting has been defined similarly as previously, the tooth has been lowered, and after penetration the horizontal velocity 0.4 m/s has been prescribed. Interaction of the tooth with material particles is shown in Fig. 13.3b. Formation of a chip can be seen in this figure.

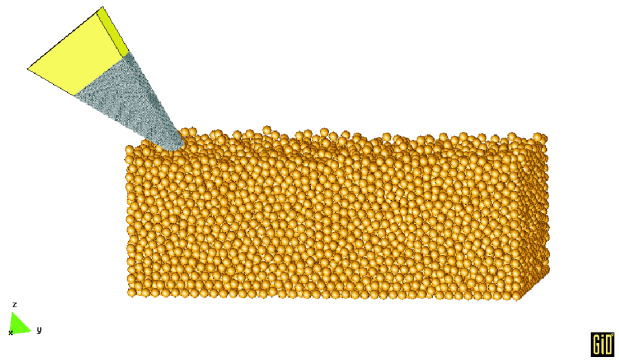

a) t = 0.0 s

b) t = 1.0 s

Figure 13.3: 3D simulation of rock cutting (model II)

Wear has been calculated according to Eq. (6.1) using the constants $\bar{k} = 5 \cdot 10^{-9}$

and $H = 1$ Pa, Profile of wear of the tooth is presented in Fig. 13.4. Maximum value of wear, 0.14186 is smaller than particle diameter, 3 mm, so the tool shape was not modified.

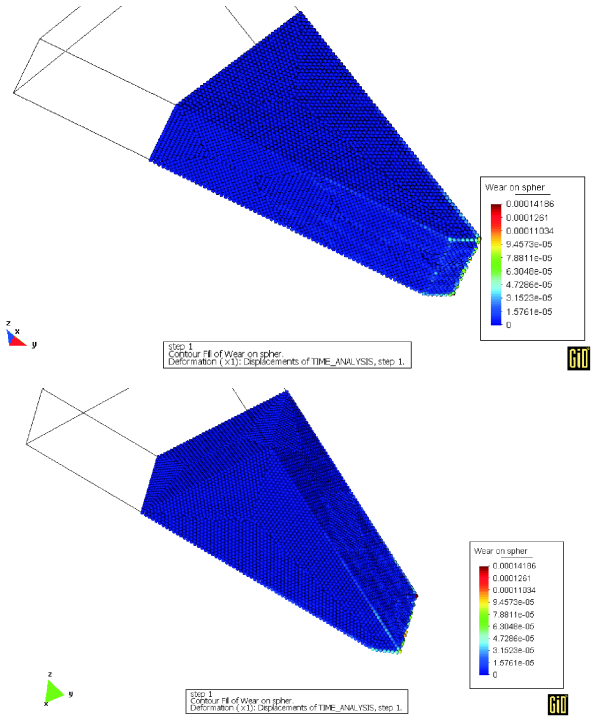

Figure 13.4: 3D simulation of rock cutting (model II) - profile of wear on the tooth at time t = 1 s

13.4 3D simulation of rock cutting (model III)

Model III of 3D rock cutting (Fig. 13.5a) is essentially the same as model II. The basic difference is in increased wear constant $\bar{k} = 5 \cdot 10^{-6}$, to produce accelerated wear and to test algorithm in short simulation.

The process of cutting has been defined similarly as previously, the tooth has been lowered, and after penetration the horizontal velocity 0.4 m/s has been prescribed. Interaction of the tooth with material particles is shown in Fig. 13.5b.

Tool shape was modified by removal of particles from the surface when the accumulated wear (thickness) exceeded their diameter. The shape of the tool at different stages of the cutting process is shown in Fig. 13.6. It can be noted that particles near the tip and on the edges have been worn out and eliminated. Profile of wear on the surface of the tool is shown for different stages in Fig. 13.7. Eliminated particles are presented in Fig. 13.8. Figure 13.8 shows clearly zones where highest wear occur.

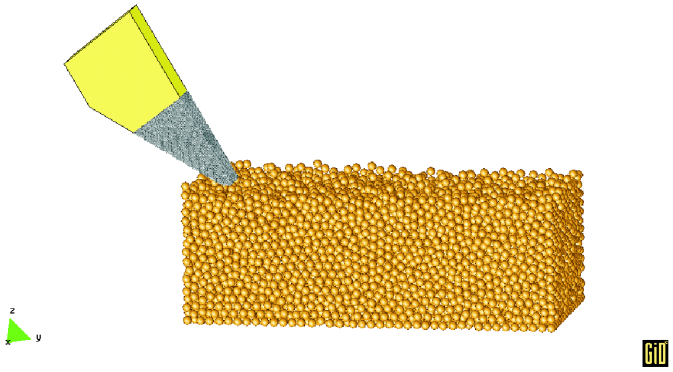

a) t = 0.0 s

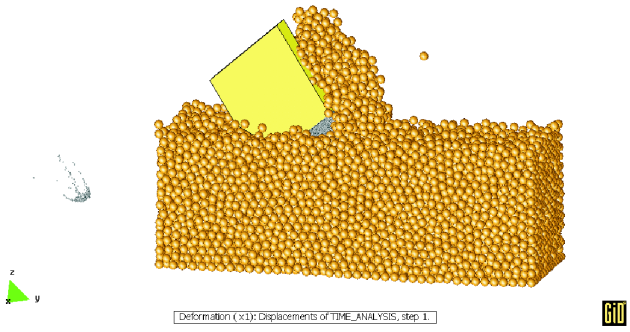

b) t = 1.0 s

Figure 13.5: 3D simulation of rock cutting (model III)

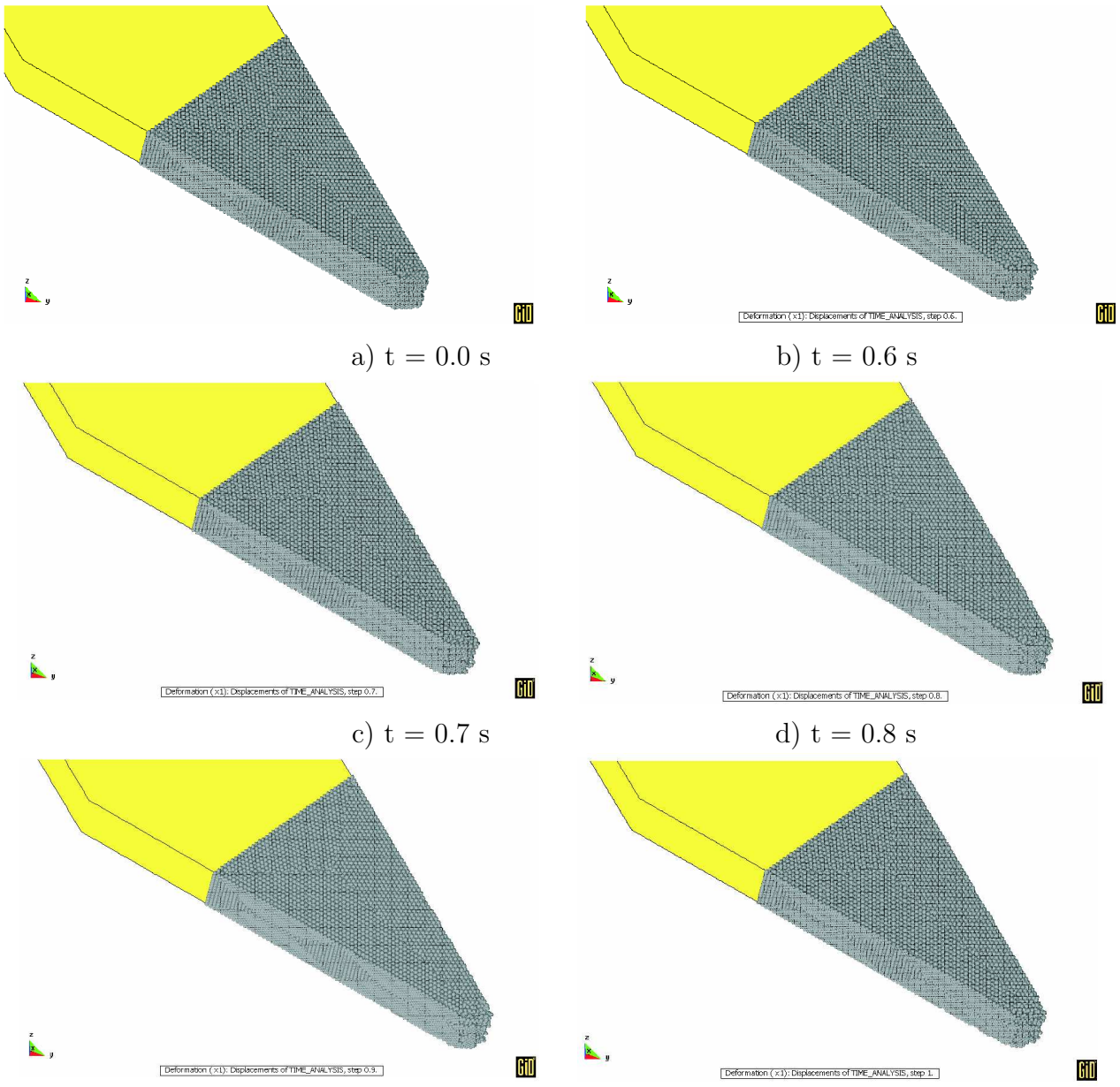

a) t = 0.0 s

b) t = 0.6 s

c) t = 0.7 s

d) t = 0.8 s

e) t = 0.9 s

f) t = 1.0 s

Figure 13.6: 3D simulation of rock cutting (model III) - change of tool shape due to wear

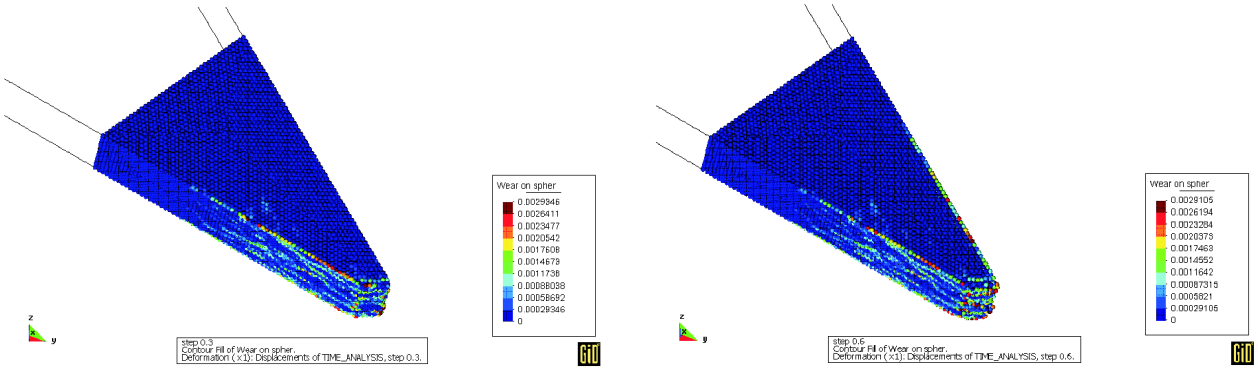

a) t = 0.3 s b) t = 0.6 s

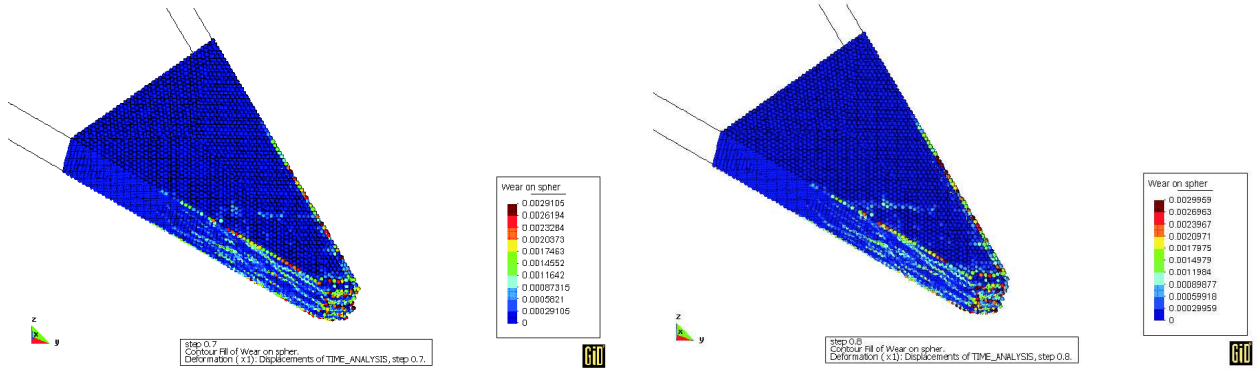

c) t = 0.7 s d) t = 0.8 s

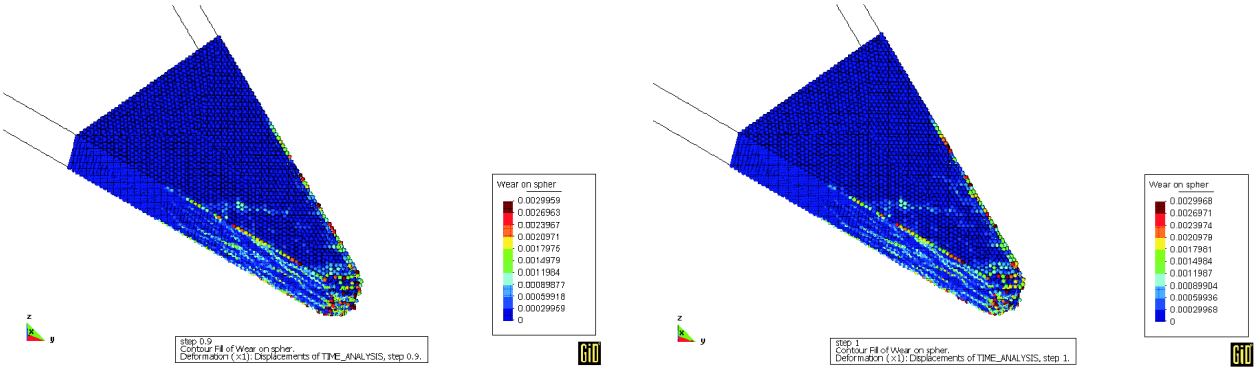

e) t = 0.9 s f) t = 1.0 s

Figure 13.7: 3D simulation of rock cutting (model III) - change of tool shape due to wear

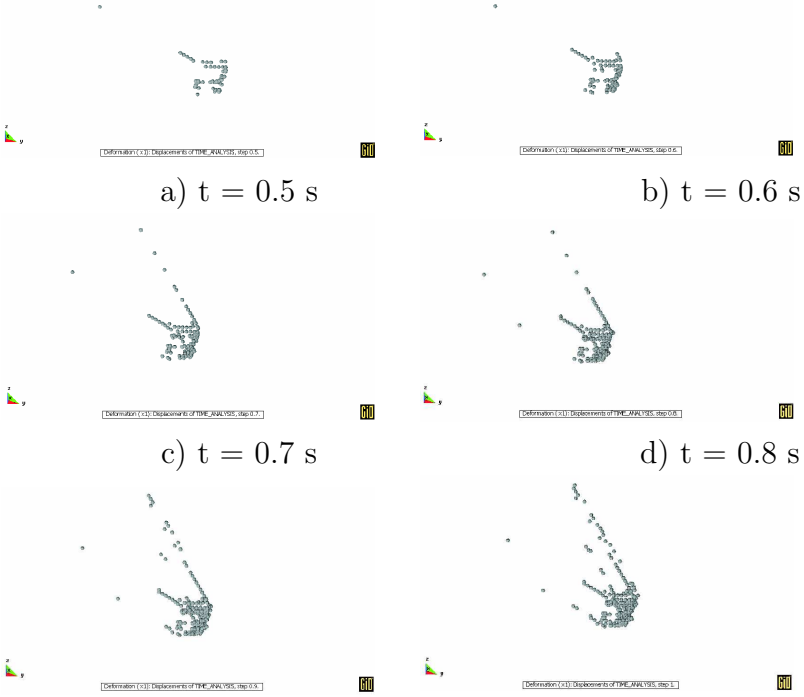

a) t = 0.5 s b) t = 0.6 s

c) t = 0.7 s d) t = 0.8 s

e) t = 0.9 s f) t = 1.0 s

Figure 13.8: 3D simulation of rock cutting (model III) - removed worn out particles

Chapter 14

Numerical examples – granular flow

The computational model developed by CIMNE has been implemented in an enhanced version of the "in house" developed explicit dynamic computer code SIMPACT. SIMPACT is an explicit dynamic computer code mainly developed to simulate contact and impact dynamic problems. Further developments on the code have been necessary in order to deal with the computational simulation of the moulding process.

The numerical model described in the previous section has been implemented in a computer program. Different computational simulations have been performed in order to assess the formulation developed for the sand flow and compaction by vibration within the lost foam technology. Here four simulations tests are considered. In the first test, the repose angle is evaluated. In the second example the flow of sand into horizontal tube under vibration is studied. Third example shows the possibility to study deformation of the pattern under sand pressure during mould filling and vibration. The last example presents possibilities of 3D simulation for a test pattern geometry. Numerical results are compared with experimental data.

Chapter 15

Conclusions

The following conclusions may be obtained:

- A numerical model based on the Discrete Element Method using spherical or cylindrical rigid particles is suitable to model mould manufacture, sand filling and compaction of sand by vibration.
- Computer implementation within the FE explicit dynamic code enables us to create a model combining the Discrete Element Method with the Finite Element Method, which gives the possibility to take into account deformation of the foam pattern during filling and vibration.
- Experimental validation tests show good correlation of numerical results with practice.
- Numerical analysis can be used to find parameters characterizing mould manufacture process
- Computation cost time is quite expensive. Further possibilities to reduce computing including parallelisation of the code would be considered.

Wear problems are difficult to handle. It is known that wear is system dependent process. Rock cutting belong to the most complicated processes to study, cf. [23]. The tribological system, we have to deal with, is hard to study in laboratory. There is little correlation between laboratory wear tests and real cutting conditions. The laboratory tests help to understand the wear mechanism. The results of these tests are generally not directly applicable to quantify the wear in real cutting process.

Acknowledgement

Financial support of the European Commission through the Growth European Project GRD1-2000-25243 “Shortening Lead Times and Improving Quality by Innovative Upgrading of the Lost Foam Casting Process (FOAMCAST)” is gratefully acknowledged.

Bibliography

[1] P.A. Cundall and O.D.L. Strack. A discrete numerical method for granular assemblies. *Geotechnique*, 29:47–65, 1979.

[2] J. Rojek, E. Oate, F. Zarate, and J. Miquel. Modelling of rock, soil and granular materials using spherical elements. In *2nd European Conference on Computational Mechanics ECCM-2001*, Cracow, 26-29 June, 2001.

[3] K. Gehring. Rock testing procedures at VA's geotechnical laboratory in Zeltweg. Technical report, Voest Alpine Zeltweg, Austria, TZU 41, 1987.

[4] B.N. Whittaker, R.N. Singh, and G. Sun. *Rock fracture mechanics.* Amsterdam, 1987.

[5] I. Evans. The force required for pointed attack picks.

[6] Y. Nishimatsu. The mechanics of rock cutting.

[7] C.S. Campbell. Rapid granular flows. *Annual Review of Fluid Mechanics*, 2:57–92, 1990.

[8] *Eng. Comput.*, 9(2), 1992. Special issue, Editor: G. Mustoe.

[9] J.R. Williams and R. O'Connor. Discrete Element Simulation and the Contact Problem. *Archives Comp. Meth. Engng*, 6(4):279–304, 1999.

[10] P.A. Cundall. Formulation of a Three Dimensional Distinct Element Model — Part I. A Scheme to Detect and Represent Contacts in a System of Many Polyhedral Blocks. *Int. J. Rock Mech., Min. Sci. & Geomech. Abstr.*, 25(3):107–116, 1988.

[11] J. Argyris. An excursion into large rotations. *Comput. Meth. Appl. Mech. Eng.*, 32:85–155, 1982.

[12] D.J. Benson and J.O. Hallquist. A simple rigid body algorithm for structural dynamics programs. *Int. J. Num. Meth. Eng.*, 12:723–749, 1986.

[13] L.M. Taylor and D.S. Preece. Simulation of blasting induced rock motion. *Eng. Comput.*, 9(2):243–252, 1992.

[14] T.J.R. Hughes. *The Finite Element Method. Linear Static and Dynamic Analysis.* Prentice-Hall, 1987.

[15] R. Löhner. *Applied CFD techniques. An Introduction based on Finite Element Methods.* Wiley, 2001.

[16] R. Löhner and K. Morgan. An unstructured multigrid method for elliptic problems. *Int. J. Num. Meth. Eng.*, 24:101–115, 1987.

[17] D.N. Knuth. *The Art of Computer Programming.* Addison-Wesley, Reading, Mass., 1973.

[18] J. Bonet and J. Peraire. An alternate digital tree algorithm for geometric searching and intersection problems. *Int. J. Num. Meth. Eng.*, 31:1–17, 1991.

[19] H. Samet. The quad-tree and related hierarchical data structures. *Comput. Surveys*, 16(2):187–285, 1984.

[20] F.L. Greengard. *The Rapid Evaluation of Potential Fields in Particle Systems. ACM Distinguished Dissertation 1987.* ACM Distinguished Dissertation Series, 1987.

[21] H. Huang. *Discrete Element Modeling of Tool-Rock Interaction.* PhD thesis, University of Minnesota, 1999.

[22] K.H. Zum Gahr. *Microstructure and wear of materials.* Amsterdam, 1987.

[23] P.N.W. Verhoef. *Wear of rock cutting tools.* Balkema, Rotterdamd, 1997.

[24] J.F. Archard. Contact and rubbing of flat surfaces. *J. Appl. Phys.*, 24(8):981–988, 1953.

[25] E. Rabinowicz. *Friction and wear of materials.* 1995.

[26] S. Stupkiewicz and Z. Mróz. A model of third body abrasive friction and wear in hot metal forming.

[27] *SIMPACT. User Manual. A finite element code for structures under dynamic and impact loadings.* Report No. 236, CIMNE, Barcelona, 1997.

[28] R.M. Polivka and E.L. Wilson. *Finite Element Analysis of Nonlinear Heat Transfer Problems.* UC SESM 76-2, 1976.